Modeling and Testing of Insulation Degradation due to Dynamic Thermal Loading of Electrical Machines

by Zhe Huang

Thesis for The Degree of Doctor of Philosophy

Real knowledge is to know the extent of one's ignorance – Confucius

Abstract

Electrical machines in electrified vehicles are subjected to dynamic loadings at different driving conditions, which results in dynamic temperatures. The aging of the Electrical Insulation System (EIS) in electrical machines is caused by these dynamic temperatures, namely high average temperatures and temperature cycles. In addition, the degradation of EIS affects the lifetime of the electrical machine.

In this thesis, three cornerstones for lifetime estimation of electrical machines in electrified vehicles are identified and studied, which are the usage, the degradation mechanisms and the lifetime model. A combination of computational simulation and lab testing is required to design a comprehensive model. Furthermore, the indicators of EIS degradations and the diagnostic methods of stator segments (or motorettes) and electrical machines with aged insulations are studied.

A system thermal model, including a drivetrain model of vehicles, a loss and cooling model and a thermal model of electrical machines, is proposed to predict the temperature distribution inside the electrical machine of an electrified vehicle. The estimated dynamic temperature at the hotspot is one of the inputs to a lifetime model of the electrical machines.

To identify the degradation mechanisms of the EIS under the dynamic temperatures, both enameled wires and motorette specimens are tested with accelerated degradation tests. It is found that the aging of the EIS of an electrical machine subjected to the dynamic temperature is not only caused by oxidation of insulations with high average temperature, but also caused by the fatigue of insulations due to thermal-mechanical stress induced by the temperature or thermal cycles. A revised lifetime model of electrical machines is proposed, which covers both aging mechanisms mentioned above. Another input to the lifetime model, the thermal-mechanical stress is estimated by Finite Element Analysis (FEA) using Ansys Structure simulation.

The condition monitoring approaches are simulated by both electrostatic FEA model and analytical model and implemented during the accelerated degradation testings. These approaches assess the State of Health of the EIS of motorette specimens . Insulation capacitance shows more consistent trends during aging at different stress levels compared to insulation resistance. Insulation capacitance reduction of 4 to 6% and 11 to 12% are found between winding and winding and

between winding and ground, respectively. A diagnostic method is proposed for measuring the high frequency current with a voltage pulse simply set by the drive of an electrical machine. The migration of both amplitude and frequency of the current detected are indications of aging of the insulation system of an electrical machine due to the decrease of the insulation capacitance.

Index Terms: thermal degradation, thermal cycle, dynamic temperature, thermal-mechanical, fatigue, electrical insulation system, accelerated testing, condition monitoring, electrical machine, electrified vehicle.

Acknowledgments

In the summer of 2013, I sat in Göteborg and concluded the first half of my Ph.D. studies with my Licentiate thesis. After more than three years, I am sitting in Göteborg again and I start to look back on the second half and the entire Ph.D. study. Lots of good things and a few bad things have happened during these years. Nevertheless, the Ph.D. period is for sure becoming an important part of my life and I would like to express my appreciation to many people who helped or accompanied me during this special journey.

First of all, I want to express my sincere gratitude to my supervisor Prof. Mats Alaküla who directed me throughout my entire Ph.D. journey. He has always been like the lighthouse that points and steers me in the right direction, during both the peaceful and stormy days with his technical advice and life experiences. I have enjoyed every discussion we have had together. I especially appreciate that I have learned things beyond the scope of science from his wisdom and his view of life.

I want to thank my co-supervisor Assoc. Prof. Avo Reinap who walked me through the entire Ph.D. journey step by step. The short and long discussions with him were always fruitful and his in-depth knowledge of electrical machines inspired me and directed me forward. He always supported me with constructive questions and new perspectives, which 'sparked' the discussions and made technical problems really fun.

I also want to thank my manager at Volvo, Azra Selimovic who together with Mats initiated my second Ph.D. project and reserved the time for me to focus on my Ph.D. studies. She always provided great advice and help to manage the project efficiently.

Many thanks to my friend and mentor Martin West who always challenges me with different perspectives and always supports me with his extensive knowledge of research and engineering. His way of thinking and working really inspires me and helps me to distinguish the possibilities from the impossibilities, which can be 'twisted' into possibilities eventually.

I would like to thank Odyssefs Lykartsis and Julius Björngreen who were involved in my second Ph.D. project at different stages and contributed to the research work through their master thesis projects.

My special thanks to the Volvo lab 'gang', Mikael Ohlsson, Ricard Blanc,

Contents

Contents

Chapter 1

Introduction

1.1 Background

The development of Electrified Vehicles (EV) is booming in recent years. In the development phase, much effort is put into the functionality of the electrified vehicles and many automotive companies develop their own electrification solutions. As one of the key components of EV, the electrical machine is usually pushed to its 'boundaries' to achieve maximum torque and power density within a limited volume. This challenge is usually tackled by improving the electromagnetic design and the heat transfer design to increase the specific magnetic loading and specific electric loading, respectively.

With the gradually increased maturity of the functionality, the reliability and durability of the electric traction system becomes more relevant and important, in order to decrease the cost in terms of material and maintenance and increase the safety level. Under-dimensioning of the electrical machine results in a shorter component lifetime than the rest of the system, leading to safety issues and increased cost of the aftermarket. However, over-dimensioning of the electrical traction machine leads to overly long lifetime of the component, thereby over-dimensioned system, including the power electronics controllers and batteries. It is therefore important to design the electrical machine for traction purpose with an optimal lifetime.

1.2   Scope and objectives

There are several critical questions that to be addressed in order to provide a proper and precise answer to the lifetime estimation of electrical machines.

Firstly, what are the major causes for degradation and failure that reduces the lifetime of an electrical machine?

The lifetime of an electrical machine is strongly related to the stresses it is exposed to, such as the TEAM stresses (Thermal, Electrical, Ambient and Mechanical stresses) [1]. Regarding to electrical machines for traction purpose, it is important to study the distribution of these stresses during the usage of vehicles in different driving conditions by various types of simulations (thermal, electrical, mechanical, acoustic etc.).

Among all the previous mentioned stresses, thermal stress is considered as one of the most critical stresses for traction electrical machines, since traction machine designs are always pushed towards the limit of their thermal capabilities. The thermal stress, in terms of temperatures are very dynamic, and it includes different levels of average temperature and a spectrum of temperature cycles.

The research reported in this thesis provides a system thermal model to understand the temperature distribution based on usage of the electrical machine while the vehicle is driving. As a result of the high and dynamic thermal stress, the stator electrical insulation systems (EIS), such as winding to winding (including turn to turn and phase to phase) and winding to ground insulations, degradate and fail. This type of degradations and failures occupies a large proportion of the different failure modes of electrical machines.

Secondly, what are the definitions and mechanisms of electrical machine degradation and failure?

The peak operation range or over-loading capacity of an electrical machine is usually linked to or limited by the drive of the machine. The optimal design of an electrical machine allows the maximum current and voltage set by the drive, without over-stressing the machine. Some over-stresses, such as over-heat of magnets, will immediately decrease the performance. Some over-stresses, such as overly high mechanical stress of the rotor at immoderate speed, could lead to immediate failure. But an accumulating degradation, such as the degradation caused by thermal stress, can gradually degrade the electrical machine and eventually lead to failure after long exposure. The electrical machine and its drive system needs to be designed in a manner which allows it to run normal operations (including instances of peak performances or over-loading operations), whilst withstanding

the stress levels which lead to degradation, and ultimately provide the required lifetime. The thermal stress degradation and accumulated degradation to failure is studied in this thesis. Both tests and simulations are used to identify the mechanisms of degradation of stator EIS caused by thermal stresses, including high average and cyclic thermal stresses.

Identification of the root causes and understanding of the process for degradation and failure is one of the essential prerequisites in designing a more reliable product. For example, the notion that 'the reliability of traction machines and drives will be improved by improving the cooling systems' is based on the assumption that temperature stress is the root cause of degradation. In other words, a correct identification of root causes could therefore be an important factor to enable design of highly reliable components and system in a short time perspective, and to decide the direction of technical development in a long time perspective. Furthermore, understanding the degradation mechanisms will permit different approaches for condition monitoring, thereby increasing the accuracy for the quantification of reliability and lifetime of the design.

Two methods are commonly used to identify the root causes for degradations and failures, namely the 'passive way' and the 'active way'. A 'passive way' is based on feedback or failure reports from the field after products have been launched. The advantage of this method is that the failure modes and targets can be relatively clear. However, the vehicle's life cycle is usually very long, which can delay the feedback, especially for failures caused by normal usage. Also, no failure reports would arise from over-sized components when the lifetime of the system has been reached. As shown in [2] and [3], the required lifetime of a rail traction motor is approximately 30 years and of a motor for electrical buses or trucks is approximately 60,000 hours. From the customer's perspective, failure of traction units of vehicles can lead to high costs, if normal working schedules cannot be met. The 'active way' is based on previous statistical data, usage of products and knowledge of degradation mechanisms. From these parameters an 'educated guess' of the root cause can be postulated and subsequent design improvement can eliminate possible failures at an early stage. The research presented in this thesis will be using the 'active way'.

In this work we test the degradation of EIS caused by cycled temperatures. Thereafter, we examine the degradation process of the EIS via the measured insulation parameters, such as insulation resistance and capacitance. The relationship between the global EIS and the local individual electrical insulation (EI) mate-

rials, is reviewed by the electrical simulations with the known geometries and materials of the studied objects. Another method, to study degradation and failure of the electrical machine, is to treat it as a 'black box'. Deviations from normally expected behavior of an electrical machine are classified as 'symptoms'. With this approach, condition monitoring is carried out through accessible signals, such as current, power, vibration and so on. Measurements can be acquired either from already implemented sensors on-board or by additional sensors and logging devices. One of the challenges of this 'black box' approach is that a particular change of a signal could represent multiple degradation and failure locations/modes. Another drawback is that the acquired knowledge from the measurements is hardly used to improve the design of the studied object, because of the limited information inside the 'black box'.

The scope and objectives of this research work are

1. Understanding of the usage of the electrical machines for traction purpose by system thermal simulations;

2. Identification of the degradation mechanisms and estimation of lifetime by accelerated aging tests and simulations;

3. Development and application of off-board condition monitoring measurements for further development of on-board condition monitoring and Residue Useful Life (RUL) prediction of traction electric machines.

1.3   Disposition of the thesis

This thesis contains the following 8 chapters.

Chapter 1 is the introduction chapter, which includes background, scope and objectives of the research. Contributions of the research and publications are listed.

Chapter 2 contains the literature review. The statistics of electrical machine failures, definition of EI and EIS, accelerated tests and condition monitoring methods are discussed.

Chapter 3 contains the modeling and simulations of the insulations of motorette samples for condition monitoring. Both Finite Element Analysis (FEA) and analytical models are utilized to estimate the measurement ranges.

Chapter 4 contains the modeling and simulations of the insulations of motorette samples for mechanical stress induced by thermal stress.

Chapter 5 demonstrates the system simulation with consideration of the usage of vehicles and the lifetime estimation models with consideration of two degradation mechanisms.

Chapter 6 describes the selection of relevant tests, explain the test procedures and measurement techniques, define the test setup and control strategies. The tests are carried out on different types of specimens including enameled wire, motorette and electrical machine.

Chapter 7 concludes and compares the results from different types of experiments and simulations.

Chapter 8 contains the conclusions of the current studies and discusses the future work.

1.4 Contributions

The approaches and contributions of the research are described as following.

Firstly, the system thermal model is built. With inputs of vehicle driving cycles, vehicle data, the required torques and speeds of the electrical machine are obtained, thereby the dynamic temperatures and the resulted lifetime of the EIS are estimated. Through this type of simulation we can understand the traction machine usage. The approach is generic and could be utilized by other drivetrain systems or traction electrical machines.

The thermal-mechanical stress analysis of the primary electrical insulation, i.e. winding coating, followed by a fatigue life estimation based on Inverse power law and Miner's rule (refer to Table 2.2) is proposed. This simulation together with the lifetime estimation based on Arrhenius law (refer to Table 2.2) represents the degradation caused by cycled temperature and average high temperature, respectively. The dominating degradation mechanism among the two above mentioned factors is defined as the one that results in a shorter lifetime, despite the linked degradation effects between these two.

Secondly, the high average thermal and thermal cycle degradation of insulation and EIS are studied by means of both tests and simulations. Thermal degradation at constant temperatures is widely studied on individual materials or single wires. Thermal index or thermal class for insulation materials or wires are defined in this manner. However, little is known regarding degradation of insulation systems exposed to cycled temperatures, especially for random-wound windings of electrical machines for traction applications. The accelerated aging tests are

carried out as shown in Fig. 1.1.
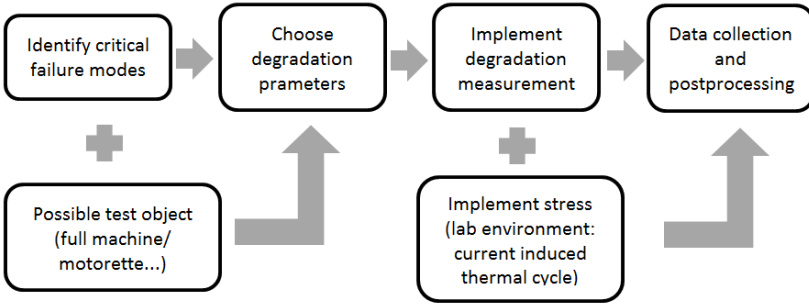
Fig. 1.1 Flowchart of the research steps for high average thermal and thermal cycle impact on EIS of traction electrical machines.

Test specimens/motorettes are designed and produced for accelerated aging test purpose. The experience accumulated during the production process will assist similar studies in the future

Also, a test rig is built to create the desired thermal cycles, using current control and forced water cooling control, for accelerated aging tests. Compared to the thermal stress provided by an oven, the in-house test rig provides temperature distribution, which more closely reflects the that of electrical machine stators in real application.

Both DC and AC measurements are applied for condition monitoring tests. The irreversible changes of insulation properties of tested motorettes are identified during the degradation tests and are used either as indicators for degradation or failure. Similarly, electrical models and thermal-mechanical models are also built for motorettes which links the changes of an individual insulation (i.e. local property) with the changes of the EIS (i.e. global property). The simulations provide the insights to understand the collected data from test.

Thirdly, based on the understanding from offline tests, an online measurement method for electrical machine diagnostics by high frequency current analysis is investigated in depth through a master thesis study within the project. A new impregnation epoxy is proposed to improve thermal behavior (verified by simulations and tests) and reduce thermal mechanical stress during thermal cycles (verified by simulations).

From a simulation perspective, steady state and transient thermal simulations, electrical simulations and thermal-mechanical simulations are implemented with

the purpose to estimate dynamic temperatures, ranges of State of Health (SoH) or condition monitoring measurements and thermal induced mechanical stresses, respectively. From a test perspective, accelerated test methods, designing and producing of test specimens and implementation of offline and online SoH measurements are studied and applied. This project contributes to the in-depth knowledge of thermal cycle degradation, lifetime estimation through simulations and tests for insulation systems of electrical machines.

1.5   Publications

Publication part I [1]

F. Marquez-Fernandez, A. Reinap, Z. Huang, M. Alaküla, "Dynamic Evaluation of the Overloading Potential of a Convection Cooled Permanent Magnet Synchronous Motor", IEEE International Electric Machines & Drives Conference (IEMDC), Niagara Falls, Canada, 2011.

Shafigh Nategh, Andreas Krings, Zhe Huang, Oskar Wallmark, Mats Leksell and Magnus Lindenmo, "Evaluation of Stator and Rotor Lamination Materials for Thermal Management of a PMaSRM", 20th International Conference on Electrical Machines (ICEM), Marseille, 2-5 September 2012.

Zhe Huang, Shafigh Nategh, Mats Alaküla, Viktor Lassila, Jinliang Yuan, "Direct Oil Cooling of Traction Motors in Hybrid Drives", IEEE International Electric Vehicle Conference (IEVC), Greenville, SC, 2012.

Zhe Huang, Francisco Marquez, Mats Alaküla, Jinliang Yuan, "Characterization and Application of Forced Cooling Channels for Traction Motors in HEVs", XXth International Conference on Electrical Machines (ICEM), Marseille, 2-5 September 2012.

Francisco Marquez, Zhe Huang, Mats Alaküla, "Redesign of an Electrical Rear Wheel Drive (E-RWD) for a hybrid vehicle in a given drive cycle", XXth International Conference on Electrical Machines (ICEM), Marseille, 2-5 September 2012.

Shafigh Nategh, Zhe Huang, Oskar Wallmark, Mats Leksell, Andreas Krings, "Thermal Modeling of Directly Cooled Electric Machines Using Lumped Parameter and Limited CFD Analysis", IEEE Transactions on Energy Conversion 28.4 (2013): 979-990.

Zhe Huang, "Thermal Design of Electrical Machines-Investigation and Evaluation of Cooling Performances." (2013). Technical Licentiate thesis.

Publication part II [2]

Zhe Huang, Francisco J. Marquez-Fernandez, Yury Loayza, Avo Reinap, and Mats Alaküla. "Dynamic thermal modeling and application of electrical machine in hybrid drives." International Conference on Electrical Machines (ICEM), pp. 2158-2164. IEEE, 2014.

Zhe Huang, Avo Reinap, and Mats Alaküla. "Predictive monitoring of turn-to-turn insulation in single tooth coils." 10th International Symposium on Diagnos-

---

[1] **Publications before Technical Licentiate Degree**
[2] **Publications after Technical Licentiate Degree**

tics for Electrical Machines, Power Electronics and Drives (SDEMPED), IEEE, 2015.

Zhe Huang, Avo Reinap, and Mats Alaküla. "Degradation and Fatigue of Epoxy Impregnated Traction Motors Due to Thermal and Thermal Induced Mechanical Stress - Part I: Thermal Mechanical Simulation of Single Wire due to Evenly Distributed Temperature", 8th International Conference on Power Electronics, Machines and Drives (PEMD), IET, 2016.

Zhe Huang, Avo Reinap, and Mats Alaküla. "Degradation and Fatigue of Epoxy Impregnated Traction Motors Due to Thermal and Thermal Induced Mechanical Stress - Part II: Thermal Mechanical Simulation of Multiple Wires due to Evenly and Unevenly Distributed Temperature", 8th International Conference on Power Electronics, Machines and Drives (PEMD), IET, 2016.

Zhe Huang, Avo Reinap, and Mats Alaküla. "Dielectric Properties Modeling and Measurement of Single Tooth Coil Insulation System under Accelerated Degradation Test", International Conference on Electrical Machines (ICEM), IEEE, 2016.

Chapter 2

Review of degradation and failure of electrical machine

2.1 Electrical machine failures

In [4], Tavner summarizes the fault distribution (Table 2.1) in different parts of induction machines based on previous publications [5–8]. A general conclusion from the review is that bearing failure is dominant for small and medium low voltage (LV) induction machines. In medium and high voltage (MV and HV) induction machines, stator failure is as common as bearing failure. However, no similar survey or literature review is found for electrical machines used in Electrified Vehicles (EV).

The common types of electrical machines in EV are reviewed in [9, 10]. As shown in Fig. 2.1, except for induction machine (IM), switched reluctance machine (SRM), reluctance machine (RM) and especially permanent magnet machine (PMM) are often used machine topologies for traction purpose. Therefore, comparing types of electrical machines for which degradation studies are available with the electrical machines used in EV there is a clear gap between the research and the market need.

Without sufficient support from the literature, a logic prediction of failure modes for traction electrical machines could be that the stator failure and bearing failure are equally significant, similarly to MV and HV induction machines (Table. 2.1). Our conclusions are as based on the following facts:

1. The requirements of traction electrical machines are tend to be high power density, over loadings to accommodate vehicle acceleration requirements and dynamic loadings because of the driving conditions. Therefore, stators of the machines are exposed to higher thermal stress, in terms of high average temperature and more cyclic temperature, in comparison to the stators of electrical machines for industry use;

2. With the trend of developing high frequency power electronics, issues such as high dv/dt and high stray electrical field on bearings arise, thereby increasing the probability of bearing failures. Also, the trend of developing high speed electrical machines increase the likelihood of bearing failure.

Based on literature review above, this research focuses on the degradation and failure of the machine stator, particularly the electrical insulation system (EIS), one of the key failure locations of traction electrical machines. Also, we focus on the thermal degradation caused by high average thermal and thermal cycle as its root cause of degradation and failure.

(a) PMM – PM brushless machine

(b) IM – Induction machine

(c) SRM – Switched reluctance machine

(d) RM – Reluctance machine
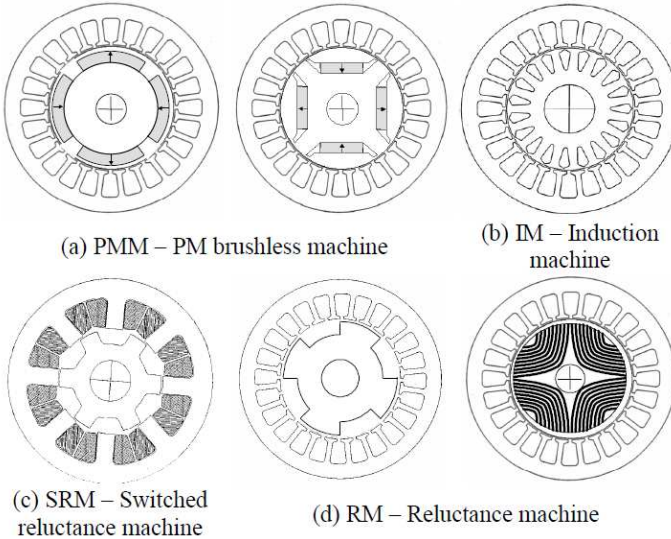
Fig. 2.1 Main traction machine technologies [9]

Table 2.1: Fault distribution in different parts of electrical machines from literature [4]

	Predicted by an OEM through FMEA techniques, 1995-7	MOD survey, 1999 [8]	IEEE large motor survey, 1985 [6]	Motors in Utility, Applications 1995 [7]	Motor Survey offshore and petro-chemical 1995 [5]
types of electrical machine	small to medium LV motors and generators <150kW, generally squirrel cage induction motors	small LV motors and generators <750kW, generally squirrel cage induction motors	motors >150kW, generally MV and HV induction motors	motors >75kW, generally MV and HV induction motors	motors >11kW, generally MV and HV induction motors
bearing	75%	95%	41%	41%	47%
stator	9%	2%	37%	36%	13%
rotor	6%	1%	10%	9%	8%
others	10%	2%	12%	14%	38%

2.2 Electrical insulation material and system

2.2.1 Electrical insulation (EI)

Electrical and electronic insulating (EI) materials, also called dielectric materials, are essential for proper operation of all electrical and electronic equipment [11]. In fact, equipment size and operating limitations are dictated by the type and amount of material required for insulation. Shugg [11, p. 1-9] discusses the development of different types of insulation material, from the early time when engineers had to adapt wood-finishing varnish, natural resins, coal tars and petroleum asphalt, to nowadays that the high-temperature polymers such as polyamideimide (PAI) and polyetherimide (PEI). The electrical insulation materials have developed in parallel with the electrical equipment and more and more synthetic materials are available. Several characteristics are defined for electrical insulation materials as stated in [12] and [13], such as dielectric strength, resistivity, dielectric constant or relative permittivity and dielectric power loss, etc.

2.2.2 Electrical insulation systems (EIS)

More than one electrical insulation material is used in one electrical machine and the combination of insulation materials is called as Electrical Insulation System (EIS). The combinations differ according to application requirements, in terms of electrical, thermal, mechanical strength, etc. The electrical machine stator insulation system contains several different components and features, which together ensure that electrical short-circuits do not occur, that the heat from the conductor losses are transmitted to a heat sink or cooling media, and that the conductors do not vibrate in spite of the magnetic forces [1, p. 12,14].

The basic stator insulation system consists of four components: strand (or sub-conductor) insulation, turn insulation, groundwall (or ground or earth) insulation and phase insulation. The EIS of a random wound slot is shown in Fig. 2.2.

Apart from the insulation materials shown in Fig. 2.2, impregnating varnish or resins are often used to increase the electrical insulating strength, mechanical strength, and insulate the stator windings from environmental exposure, such as moisture, dust. Furthermore, with the high torque and power density required by traction machines of EV, more electrical machines are completely impregnated by epoxy or silicon materials with higher thermal conductivities than that of traditional resins. Vacuum and pressure impregnation (VPI) method is usually applied

for the complete encapsulation and results in good penetration of the resins into the small gaps between windings and between windings and slots.

However, the VPI method is more complicated and time-consuming in comparison with other impregnation methods, such as dipping and trickling process. As a result, it is more challenging for high volume productions. The detailed processes for the dipping, trickling and VPI impregnation methods are explained in [14]. In our studies, we simulated and tested the motorettes with complete encapsulation with VPI method.
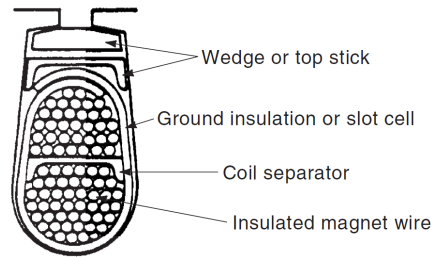
Fig. 2.2 Cross section of a random stator winding slot [1]

2.3 Accelerated test

Accelerated test is divided into two types, namely accelerated degradation/ qualitative accelerated test and accelerated life/quantitative accelerated test [1, 15, 16].

Using accelerated test as a qualitative tool can be very effective [15]. The qualitative accelerated test is primarily used to identify failures and failure modes. It could be used to evaluate a 'candidate' system by comparing it to a 'proven'/ 'reference' material or system under the same accelerated test conditions. The comparison of results between different materials/systems is the usual way aging tests are evaluated in standards [1, p. 50]. Compared to the qualitative accelerated test, the quantitative accelerated test is used to make predictions about a product's life characteristics (such as L50 life) under normal use conditions [15]. However, to correlate the data from accelerated tests with the actual use is extremely difficult, and some of the failure modes exposed to the accelerated testings may not occur during the normal operations [1, 15, 16].

In general, the purpose of the accelerated test is to save the time and resources

when evaluating the strength of the products or systems, in comparison to the their actual lifetime. However, the cost of accelerated test, in terms of time and resources, could still be significant compared to other types of test. Therefore it is important that the parties involved, such as manufacturers, users/purchasers and testing facilities, agree upon the testing parameters, from 'definition of pass/fail criteria' to 'requirements of test reports' (in total 21 terms), prior to the commencement of the tests, as stated in [17, p. 18].

2.3.1   Accelerated lifetime models

The commonly used lifetime models are listed in Table 2.2 and Table 2.3 [15]. Additions to the Inverse Power Law in Table 2.2, Equation 2.1 and 2.2 [18] are also often used to describe the lifetime of insulations exposed to constant electric stresses. The Arrhenius model and Miner's rule are applied in later studies and explained in detail in Chapter 5.

$$Life = kV^{-n} \tag{2.1}$$

$$logL = logk - nlogV \tag{2.2}$$

where V is the applied voltage, k and n are constants to be determined.

Apart from the models described in Table 2.2 and 2.3, Design of Experiment (DoE) models are also used utilized for accelerated tests to study the EI or EIS degradations caused by multiple stresses. Research groups from Univesity of Toulouse and Laboratory for PLAsma and Conversion of Energy (LAPLACE), Toulouse, France, have published on several interesting studies on this subjet. One example, showing the relationship between the lifetime of an insulation material with multiple stresses, by means of DoE, is shown in Equation 2.3 [19].

$$
\begin{aligned}
Log(L) \sim\ & M + E_V \cdot log(V) + E_F \cdot log(F) \\
& + E_T \cdot exp(-bT) + E_{FV} \cdot log(V) \cdot log(F) \\
& + E_{VT} \cdot log(V) \cdot exp(-bT) + E_{FT} \cdot log(F) \cdot exp(-bT) \\
& + E_{VFT} \cdot log(V) \cdot log(F) \cdot exp(-bT)
\end{aligned} \tag{2.3}
$$

where V, F, T are the voltage, frequency and temperature stresses applied during test, respectively. M, b, E_V, E_F, E_T, E_{FV}, E_{VT}, E_{FT} and E_{VFT} are the coefficients decided by the tests, which are the impact factors of lifetime determined by each stress and by each two stresses and by all three stresses.

2.3.2 Statistics

The lifetime data collected from field or tests on number of specimens is usually scattering. Hence, statistics method is applied to process data with such an attribute, which includes the distribution model and the curve fitting/regression analysis. The distribution model is to quantify the normal amount of variation in an outcome, and the regression analysis is to derive an equation based on aging tests at a few stress levels, that can be used to predict the outcome of a test at a different stress level, respectively [1]. Furthermore, the lognormal and Weibull distribution are the two often used distribution models and the latter one is used in our studies and discussed further in Chapter 5.7. Regression analysis, including parameters identification and confidence limits calculation of a statistical distribution, is often carried out by programs such as 'Weibull ++'.

2.4 Standards of constant thermal and thermal cycle tests

In this section, the often used standards related to thermal degradation, namely the degradation caused by constant temperature and that caused by cyclic temperature, of Electrical Insulation (EI) and Electrical Insulation System (EIS) in electrical machines are reviewed and summarized in Table 2.4.

Apart from the standards from IEC and IEEE listed in the table, ASTM has a large collection of standards to test different types of EI as presented in [1, p. 68] and [20]. Other relevant IEEE standards can also be found in [1, p. 59].

By standards review, it is observed that many standards are focused on the thermal degradation caused by constant temperature. However, fewer of them emphasize on the thermal degradation caused by cyclic temperature, among which form-wound stators of large electrical machines are focused. There is a clear gap between the existing and the needs of thermal degradation standards of electrical machines for electrified vehicles application.

Table 2.2: Accelerated lifetime models [15]

Model Name	Description /Parameters	Application Examples	Model Equation
Arrhenius acceleration model	Time to Failure as a function of Relative Humidity and Temperature	Electrical Insulation and Dielectrics, Solid State and Semiconductors, Intermetallic Diffusion, Battery Cells, Lubricants Greases, Plastics, Incandescent Lamp Filaments	$Life = A_0 e^{-E_a/kT}$ where: Life = median life of a population A_0 = scale factor determined by experiment e = base of natural logarithms E_a = Active Energy Unique for each failure mechanisms k = Boltzmann's constant $= 8.2 \times 10^{-5}$ev/K T = Temperature(degrees Kelvin)
Inverse power law	Life as a function of any given stress	Electrical insulation and dielectrics (voltage endurance), ball and roller bearings, incandescent lamp filaments, flash lamps	$\frac{Life_{norm}}{Life_{acc}} = \left(\frac{Stress_{acc}}{Stress_{norm}}\right)^{N}$ where: Life_norm = life at normal stress $Life_{acc}$ = life at accelerated stress $Stress_{norm}$ = normal stress $Stress_{acc}$ = accelerated stress N = acceleration factor
Miner's rule	Cumulative linear fatigue damage as a function of flexing	Metal fatigue (valid only up to the yield strength of the material.)	$CD = \sum_{i=1}^{k} \frac{C_{Si}}{Ni}$ where: CD = cumulative damage C_{Si} = number of cycles applied at stress Si Ni = number of cycles to failure under stress Si (determined from an S-N diagram for that specific material) k = number of loads applied

Table 2.3: Accelerated lifetime models - continued [15]

Model Name	Description /Parameters	Application Examples	Model Equation
Coffin-Manson	Fatigue life of metals (ductile materials) due to thermal cycling and/or thermal shock	Solder joints and other connections	$Life = \frac{A}{\Delta T^B}$ where: Life = Cycles to failure A = scale factor determined by experiments B = scale factor determined by experiments ΔT = temperature change
Thermo-mech-anical stress	Time to failure as a function of change in temperature	Stress generated by differing thermal expansion rates	$TF = B_0(T_0 - T)^{-n} e^{\frac{E_a}{kT}}$ where: TF = Time-to-Failure B_0 = scale factor determined by experiment T_0 = stress free temperature n = 2 - 3 E_a = 0.5 - 0.6 eV for grain-boundary diffusion, approx. 1 eV for intra-grain diffusion k = Boltzmann's constant $= 8.2 \times 10^{-5}$ev/K T = temperature (degrees Kelvin)

Table 2.4: Reviewed standards related to constant thermal and thermal cycles degradation of insulation material, enameled wires and insulation systems of rotating electrical machines.

Standard No.	Applied thermal	Type of specimen	Description
IEC 60085 [21]	constant thermal	insulation material	Thermal classification of electrical insulation material/materials
IEC 60216 [22–24]	constant thermal	insulation material	Thermal classification of electrical insulation material/materials
IEC 60851-6 [25]	constant thermal	enameled wire	Winding thermal property
IEC 60172 [26]	constant thermal	enameled wire	Temperature Index of Enameled Winding Wires
IEC 61857 [27, 28]	constant thermal	EIS of random-wound windings	Electrical insulation systems thermal evaluation
IEC 60034-18 [29, 30]	constant thermal (part 31) and thermal cycle (part 34)	EIS of form-wound windings	Test procedures and thermal evaluation for form-wound windings
IEEE 1776 [31]	constant thermal	EIS of form-wound windings	Thermal evaluation of unsealed or sealed insulation systems for AC electric machinery employing
IEEE 1310-2012 [17]	thermal cycle	EIS of form-wound windings	Thermal Cycle Testing of Form-Wound Stator Bars and Coils for Large Generators
UL 1446	constant thermal	EIS of random-wound windings	Evaluates small- and medium-sized random-wound, low-voltage applications

2.5   Condition monitoring methods

Condition monitoring measurements are carried out to diagnose the State of Health (SoH) of the EI or EIS of electrical machines. The measurements can be divided into non-destructive (such as surge test) and destructive type (such as breakdown voltage test). Another way to categorize the measurements is in accordance with the usage of the machines when the tests are performed. The on-line and the off-line measurements correspond to the tests carried out when the electrical machines are in and not in operations, respectively. Besides, the on-board measurement is the one carried out at the location where the electrical machine serves, and the opposition of it is the off-board measurement. The often used condition monitoring methods are summarized as follows.

AC measurement

The AC measurements are usually to measure the resulting current after applying an AC voltage across the specimen. Depending on whether the amplitudes or the angles of the AC currents are analyzed, AC measurements differ slightly.

For the measurement that the amplitude of current is of interest, exceeding a certain level of current, i.e. a threshold, is considered as a failure of the specimen. This method is referred by the standards [25,26,28], which correspond to different test objects, insulation materials, enameled wires and insulation systems, and different threshold currents, 5mA, 10mA and 40mA are identified, respectively. The recommended voltage frequencies of the tests are between 48 Hz and 62 Hz in the above standards. However the voltage amplitudes are not clearly defined, which determined by the voltage levels that the specimens exposed to in operation.

The dissipation factor or $\tan\delta$ of the specimen could be obtained from AC measurements, where δ is the dielectric loss angle. An increase of the $\tan\delta$ indicates the degradation of the measured dielectric material. By other means of data post-processing, insulation capacitance (IC) and dielectric constant are obtained.

DC measurement

The DC measurements are also referred to as Hipot (high potential) tests due to the high voltages that specimens are exposed to in such tests. The amplitude of leakage current is measured. These measurements could be destructive or non-destructive depending on the amplitudes of the excitation voltages.

With different post-processing of the measured current, various parameters are obtained, for instance the insulation resistance (IR). Polarization index (PI) and dielectric absorption ratio (DAR) are defined by Equation 2.4. Table 2.5 reviews the typical values of PI and DAR and their corresponding health status.

$$PI = \frac{IR_{10min}}{IR_{1min}} \tag{2.4}$$

$$DAR = \frac{IR_{1min}}{IR_{30sec}} \tag{2.5}$$

where IR is the insulation resistance and the subscript represents the time that the measurement is carried out.

Table 2.5: Typical values of PI and DAR and health status of insulations and insulation systems [32]

Insulation resistance condition	DAR	PI
Dangerous	0-1.0	0-1
Poor	1.0-1.3	1-2
Good	1.3-1.6	2-4
Excellent	1.6 and above	4 and above

Surge test

A sudden change of a current in a coil builds up a voltage because of the nature of inductance. For a winding coil, the inductance is a sum of self inductance of each individual loop, and mutual inductance between every two individual loops. If the insulations of the adjacent coils are weak, meanwhile the induced voltage is higher than the dielectric strength of the weakened insulation, an arc will form between the conductors of the coils [33]. Surge test is designed to create the voltage between the adjacent coils and detect the arcing due to the weakened or failing insulations.

The above mentioned condition monitoring approaches are off-line measurements. The examples of online condition monitoring approaches are discussed below.

Partial discharge

The fast rise time of impulses at motor terminals induces high wire-to-wire voltages in the first coils of each phase, thereby an early breakdown between wires [34]. The upper limited level, at which this over-voltage stress becomes harmful for insulations, is the Partial Discharge Inception Voltage (PDIV) or Corona Inception Voltage (CIV) [34–36]. This is the voltage level that partial discharges begin to occur.

Electrical machines could be categorized into type I and type II machines, in which the existence of partial discharges is not permitted or permitted, respectively [37, 38]. The PD resistant materials are required for type II machines. The electrical machines with rated voltages $\leq$ 700 V r.m.s. are usually of Type I, but could also be Type II. The electrical machines rated above 700 V r.m.s. are usually of Type II. For the Type I machines, the existence of PD indicates failures of the EIS. However, keeping track of the levels of PD, in terms of PDIV, could be used to evaluate the SoH of a type II machine. A decreased PDIV indicates an aged EI or EIS of the machine. However, this measurement is temperature dependent [34]. Typically, PDIV decreases by 30% when winding temperature increases from 25°C to 155°C.

Motor current signature analysis (MCSA)

MCSA is by far the most preferred technique to diagnose faults of electrical machines [39, 40]. It is used as on-line condition monitoring for stators, rotors and bearings. Theoretical analysis and modeling of machine faults are necessary to distinguish the relevant frequency components from the others that may be present due to time harmonics, machine saturation, etc [39].

Vibration analysis

Vibration analysis is a powerful tool to detect bearing related faults of rotational machines [41–43]. Also, a study by Joachim Härsjö [44] reveals that the vibration analysis is useful to detect the turn-to-turn fault in the stator of a PMSM. Similarly to the MCSA approach, vibration analysis is demanding for data analysis.

Other condition monitoring methods

Other measurement methods, temperature monitoring, electromagnetic field monitoring, infrared recognition, radio-frequency (RF) emission monitoring, etc., are also used for condition monitoring purposes [39].

2.6 Overview of studied machines

For the convenience of discussion, an overview of the studied machines in this thesis are presented below. Table. 2.6 summarizes the vehicle applications and the types and winding specifications of the studied machines. Table. 2.7 gives a short overview of the simulations and experiments carried out for the machines.
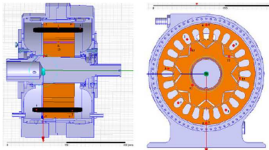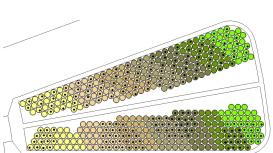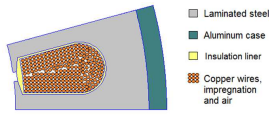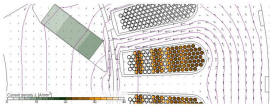
Application		
Traction machine for wheel loader	Traction machine for rear wheel drive hybrid car	Traction machine for hybrid heavy vehicles
Machines		
16-pole surface mounted PMSM	8-pole interior PMSM	6-pole interior PMSM
Windings		
Concentrated winding	Double layer distributed winding (phase divider inside the slot is shown)	Single layer distributed winding

Table 2.6: Traction machines referred by this thesis

Simulations and experiments		
1. The motorettes used in the accelerated tests are based on this machine; 2. Simulation and tests of the off-board condition monitoring; 3. Thermal-mechanical simulations; 4. Finite Element Analysis (FEA) thermal model; 5. System simulation with driving cycles.	1. Lumped Parameter Analysis (LPA) thermal model; 2. System simulation with driving cycles; 3. Validation and sensitivity studies of the on-board diagnostics method.	1. Sensitivity studies on temperature dependence of the on-board diagnostics method.

Table 2.7: Traction machines referred by this thesis (continued)

Chapter 3

Modeling and simulation for condition monitoring

In this chapter, electrical fields and parameters of the insulation systems of the motorette structure are calculated. The modelings and simulations in this chapter are used to predict the ranges of the off-board condition motioning measurements applied during accelerated degradation tests, which are discussed in later chapters. A motorette structure is a segmented stator with windings and all electrical insulations included and it represents the full-scale traction machine stator. Fig. 3.1 shows the motorette sample used for this study before epoxy impregnation is applied. More information about the motorette is described in Chapter 6.2.1.

As discussed in Chapter 2.2.2, the insulation system of the electrical machine stator is built up by wire coating, slot liner, impregnation and winding-to-winding insulation. When electric excitation is applied across electrical insulations, polarization occurs and leakage current is generated, thereby forming an electric networks with capacitive and resistive components. Fig. 3.2 shows the simplified equivalent network when electric excitation is applied between windings (left) and between windings and ground (right), separately. Theoretically, the State of Health (SoH) of the insulation system can be assessed, by identifying and tracking the changes of values of winding-to-winding capacitance (C_{ww}), conductance (G_{ww}) or resistance (R_{ww}) and winding-to-ground capacitance (C_{wg}), conductance (G_{wg}) or resistance (R_{wg}). Breakdown could be formed during the degradation, which is an irreversible process whereby the system endurance is weak-

27
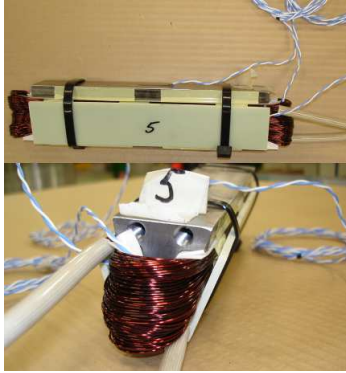
Fig. 3.1 Stator segment motorette sample before epoxy impregnation

ened. The stochastic nature of breakdown distribution and deterioration can be described mathematically through statistics. However, it is also important to understand the loads resulting in the degradation and the process of the degradation and to estimate the level of degradation of the insulation system [45] by the condition monitoring or SoH measurements described above.
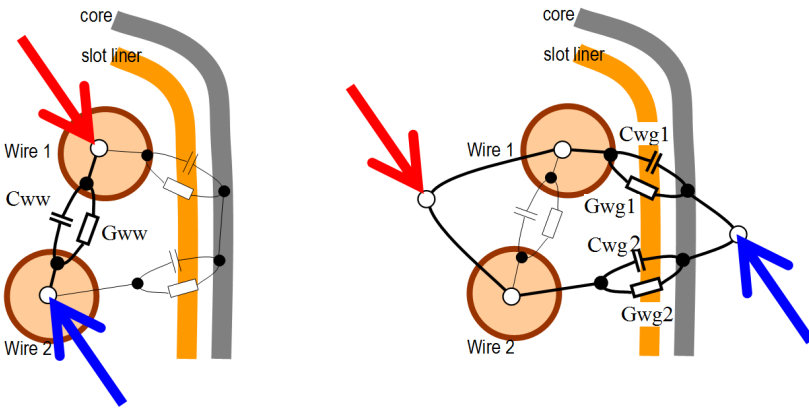
Fig. 3.2 Simplified equivalent network of insulation system: between windings (left) and between winding and ground (right)

Compared to the modeling of the insulation properties between the winding and the core, it is more challenging to model the insulation properties between

randomly grouped parallel strands. In this chapter, both the Finite Element Analysis (FEA) method and the analytical method are utilized to calculate the ranges of insulation resistance (R_{ww}) and insulation capacitance (C_{ww}) between randomly grouped parallel strands. It is expected that FEA of thermal and electrical loads would become a useful tool for visualizing the load distribution on the winding, hence estimating the winding parameters. However, compared to the FEA model, the analytical model provides the convenience of performing sensitivity studies with geometrical property and material physical property changes due to aging. Besides, the analytical model builds the link between the measured global properties of Electrical Insulation System (EIS) and the average local dimensionless values of individual electrical insulation (EI) material (such as the volume resistivity and dielectric constant) [46]. The dimensionless values can be adapted by other studies.

3.1 Geometry

As shown in Table 2.6 and Fig. 3.1, the stator segment under test consists of a winding structure of 7 turns and 29 parallel strands, which are rather arbitrarily placed into the slot of the reference machine or wound around the teeth of the test sample. Compared to a well-defined or simplified test object with a perfect conductor and insulation arrangement, this specimen structure is chosen to represent the actual electrical machine.

However, the structure of a motorette brings a challenge to simulation since neither the geometric arrangement, nor the material distribution of the coil and the insulation system can be perfectly known, due to the randomness of the distribution of the wires in one slot. However, by dividing the parallel strands of 29 wires into two groups of 14 and 15 strands randomly, it provides a great advantage that the winding insulation state of health and degradation can be estimated between these two groups and along the whole length of the windings.

A perfect conductor distribution is assumed in a machine slot as shown in Fig. 3.3. The seven turns are shown with different colors and the two groups of strands are shown with or without a dot in a conductor. These equally located hexagonal placements of conductors are defined level by level starting from the stator tooth because the coils of test samples are wound around the tooth. In practice, the coil of 29 strands can have a fairly similar appearance except for the regions between the turns. The geometrically perfect winding is defined so that the thickness of the

coating film is 6% of the conductor diameter and the additional spacing between the coated wires is 10% of the conductor diameter. [47]
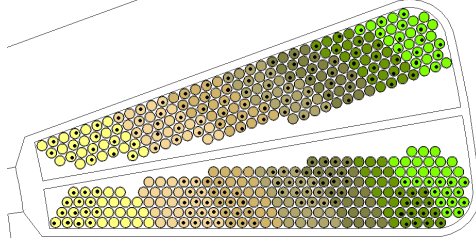
Fig. 3.3 7-turn 29-strand conductor distribution inside the slot by considering the ideal packing between the wires. The groupings of parallel strands are distributed in the upper half and concentrated in the lower half. [47]

It is not only the distance between the conductors and the properties of insulating material, but also the way of grouping the strands, that define the measured parameters of the EIS for the above condition monitoring method. As an outcome the parameters for the insulation system can vary cross a certain range that is due to geometry, material properties and location of the selected strands.

3.2 Materials

Table. 3.1 shows the material properties for both FEA and analytical simulations.

Table 3.1: Materials properties

Component	Material	Electric resistivity ρ [Ωm]	Dielectric constant ε [-]
Conductor wire	copper	$1.7 \cdot 10^{-9}$	-
Coating film	PAI	$2 \cdot 10^{15}$ [48]	4.0
Slot impregnation	epoxy	$8 \cdot 10^{12}$ [49]	3.6 [49]
Slot liner	paper	$8 \cdot 10^{12}$	3.0
Stator core	iron	$5.5 \cdot 10^{-9}$	-
-	air	$1.3 \cdot 10^{16}$ to $3.3 \cdot 10^{16}$ [50]	1

3.3   Electrostatic Finite Element Analysis (FEA)

Electrostatic or electric current modeling is made using Finite Element (FE) analysis, in order to study the E-field and load distribution and identify the electrical parameters for insulation systems. Two FEA tools, which are FEMM and Ansys Maxwell, are utilized to verify the analytical calculations made in the following sections, with identical materials and boundary conditions.

Fig. 3.4 shows one example of a distribution of the electric field intensity, which is the outcome from the situation where 1.2kV is applied across the two groups of strands. Corresponding to Fig.3.3, the electric field distribution is demonstrated in two different cases, which are for the distributed windings group (upper) and concentrated winding group (lower). Leakage current and insulation capacitance are post-processed between the groups of strands.
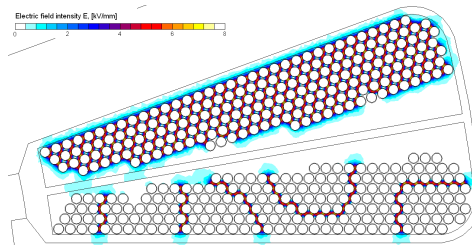
Fig. 3.4 E-field distribution (below) at 1.2 kV across the two groups of parallel strands: 1) concentrated (lower half), and 2) distributed (upper half of the slot) [47]

3.4   Analytical calculation

This part explains the method of building up the analytical model for off-board off-line condition monitoring measurements for the motorette insulation system, to estimate the parameters of leakage current or insulation resistance and insulation capacitance. Compared to the FEA electrostatic model, the analytical model provides the convenience to perform sensitivity studies with geometrical property differences or physical property changes due to aging.

3.4.1 Winding patterns

As mentioned above, neither the geometric arrangement nor the material distribution of the coil can be perfectly known. Fig. 3.5 [51] shows three types of commonly used winding configurations, namely orthocyclic winding, layer winding and random winding, respectively, which result in different slot fill-factors P_D. The highest fill-factor is obtained with orthocyclic winding distribution. With the segmented stator technique used for making the test specimens, the highest fill factor could be achieved, therefore the orthocyclic winding distribution is chosen for further modeling. The analytical modeling to estimate the insulation resistance and capacitance between two randomly selected groups of strands is demonstrated step by step below.
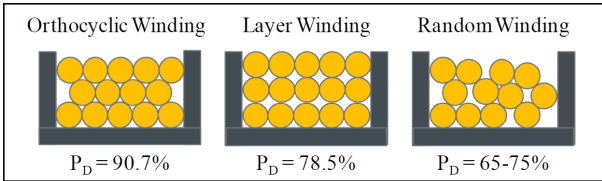
Fig. 3.5 Winding configurations [51]

3.4.2 Assembling of unified resistance and capacitance

With the orthocyclic winding configuration, except for the windings close to the slot edges, each winding shares 1/6 th of its coating and its impregnation material with the neighboring windings. Therefore, the minimum unit of insulation between each two wires is identified as shown in Fig. 3.6. Equations 3.1 to 3.4 show the calculations of insulation capacitance C_{unit} and resistance R_{unit} of the insulation unit.
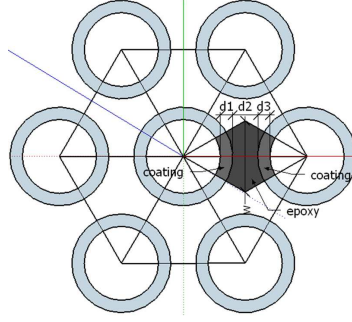
Fig. 3.6 Insulation unit between windings [46]

$$C_{unit} = \cfrac{1}{\cfrac{1}{\cfrac{\varepsilon_0 \cdot \varepsilon_{co} \cdot A}{d_1}} + \cfrac{1}{\cfrac{\varepsilon_0 \cdot \varepsilon_{ep} \cdot A}{d_2}} + \cfrac{1}{\cfrac{\varepsilon_0 \cdot \varepsilon_{co} \cdot A}{d_3}}} \tag{3.1}$$

$$= \cfrac{1}{\cfrac{1}{\cfrac{\varepsilon_0 \cdot \varepsilon_{co} \cdot w \cdot L}{d_1}} + \cfrac{1}{\cfrac{\varepsilon_0 \cdot \varepsilon_{ep} \cdot w \cdot L}{d_2}} + \cfrac{1}{\cfrac{\varepsilon_0 \cdot \varepsilon_{co} \cdot w \cdot L}{d_3}}}$$

$$R_{unit} = \frac{\rho_{co} \cdot d_1}{A} + \frac{\rho_{ep} \cdot d_1}{A} + \frac{\rho_{co} \cdot d_1}{A} \tag{3.2}$$

$$= \frac{\rho_{co} \cdot d_1}{w \cdot L} + \frac{\rho_{ep} \cdot d_1}{w \cdot L} + \frac{\rho_{co} \cdot d_1}{w \cdot L}$$

$$d_1 = d_3 = (D_{wire} - D_{cu})/2 \tag{3.3}$$

$$w = \frac{(D_{wire} + d_2)/2}{\sin \dfrac{\pi}{3}} \tag{3.4}$$

where ε_0 is the dielectric constant of air, ε_{co} and ε_{ep} are the relative dielectric constant of coating and epoxy, separately. ρ_{co} and ρ_{ep} are the volume resistivity of coating and epoxy, separately. A and w are the cross section area and width of the insulation unit, separately. L is the axial length of the winding. D_{wire} and

D_{cu} are the diameter of enameled wire and copper, separately. d_1 and d_3 are the thicknesses of the coatings and d_2 is the thickness of the epoxy.
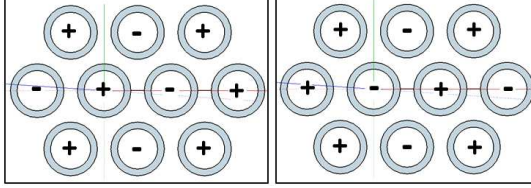
Fig. 3.7 Two possible polarity distribution for the proposed conditioning monitoring method [46]

Fig. 3.7 shows two possible idealized polarity distribution for the proposed conditioning monitoring method. Assuming that the two paralleled strands are randomly selected and the electrical field is evenly distributed, each wire is exposed to four other wires with opposite potential as shown in Fig. 3.7. This increases the total cross-sectional area of the global insulation by four times compared to the cross-sectional area of the insulation unit defined in Fig. 3.6. Also, the total cross-sectional area of the global insulation in conditioning measurement is also increased by having the number of turns and strands. As a result, the global insulation capacitance C_{tot} is increased but the insulation resistance R_{tot} is decreased. Finally, each insulation unit in Fig. 3.6 is shared by two neighboring wires, which result in a division by two. The final derivation from the dielectric properties of an insulation unit to the measurable global properties are presented by Equation 3.5 and 3.6.

$$C_{tot} = C_{unit} \cdot 4 \cdot (N_{turn} \cdot N_{strand})/2 \qquad (3.5)$$

$$R_{tot} = R_{unit}/4/(N_{turn} \cdot N_{strand})/2 \qquad (3.6)$$

where N_{turn} is number of turns in series and N_{strand} is the number of strands in parallel.

3.5   Simulation examples

With the analytical model proposed in 3.4, simulations are carried out and compared to the FEA model proposed in 3.3. Furthermore the sensitivity studies are

made using the verified analytical model. One purpose of the sensitivity study is to understand the relationship between the changes of the global insulation system properties, which can be measured directly on the motorettes or electrical machines, and the changes of local insulation properties of single materials, which cannot be easily measured in an insulation system. Another purpose of the study is to identify the primary electrical insulation material between the windings of an insulation system with complete encapsulation (defined in Chapter 2.2.2).

3.5.1 FEA simulation results

Based on the geometric data and volumetric resistivity that are presented in Chapter 3.1 and 3.2, FEA simulations by Ansys Maxwell show that the expected insulation resistance of the motorette with complete encapsulation is 640 GΩ or 2,000 GΩ and the insulation capacitance is 5.4 nF or 1.48 nF depending on whether the groups of parallel strands are distributed or concentrated, respectively (Fig. 3.3 and Fig. 3.4). For the same FEA model, if the distance between every two wires is decreased by half with the distributed winding configuration (upper half of 3.4) compared to the one defined above, the insulation capacitance will be increased to approx. 11 nF and the resistance will fall to 320 GΩ.

3.5.2 Analytical simulations and sensitivity studies

The same materials used for FEA simulations above are applied for the analytical simulations. According to the data-sheet of the enameled wire [52], the diameter of the wire and copper is approx. 0.9 mm and approx. 0.85 mm, respectively, which leads to the total coating thickness being approx. 25 μm. Therefore, a sensitivity study using coating thickness reasonably assumed to be between 15 μm and 45 μm is carried out. Similarly, the sensitivity study with varied epoxy thickness between 1.5 μm (10% of the coating thickness 15 μm) and 1.5 mm (100 times the coating thickness 15 μm) is carried out. The axial length of windings is L, 220 mm.

Figs. 3.8 and 3.9 show the expected ranges of insulation capacitance (IC) and insulation resistance (IR) with varied thickness of coating and impregnation for the proposed condition monitoring, based on the analytical model.

As shown in Fig. 3.8, the global IC of the EIS, which is measured on motorettes between paralleled strands, is heavily influenced by the average local thicknesses of both impregnation material and coating material. This also means

Fig. 3.8 Expected range of insulation capacitance with varied thicknesses of coating and impregnation for the proposed condition monitoring method [46]

that the average local thicknesses of the two materials play important roles in determining the global parasitic capacitance of electrical machines.

However, as shown in Fig. 3.9, the insulation resistance between winding strands of the motorette insulation system is mainly due to the coating material. For example, with local average thickness of the impregnation material increased from 15 μm to 1.5 mm (a factor of 100), the global insulation resistance changes from approx. 200 GΩ to approx. 600 GΩ. While with local average thickness of the coating material increased from 15 μm to 45 μm (a factor of 3), the global insulation resistance changes from approx. 200 GΩ to approx. 1,200 GΩ. The reason is that the local volume resistivity of the primary EI (such as coating material) is much higher than this of the secondary EI (such as epoxy material) in general. From this perspective, the winding coating is the major electrical insulation media between strands. In other words, the impregnation matrix material used to increase thermal conductivity, i.e. the heat transfer performance, does not enhance the electrical insulation resistance between strands. However, compared to the dielectric strength or breakdown field strength of air (approx. 3 MV/m [53]), the epoxy matrix material has a much higher breakdown field strength (approx. 19 or 21 MV/m [49]). Therefore, using impregnation improves the electrical insulation quality of the insulation system from this perspective.
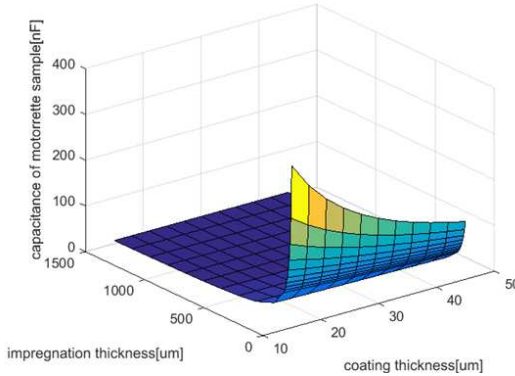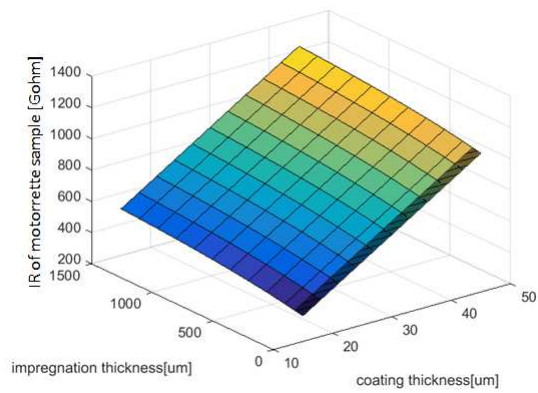
Fig. 3.9 Expected range of insulation resistance with varied thicknesses of coating and impregnation for the proposed condition monitoring method [46]

Chapter 4

Modeling and simulation for Thermal-Mechanical stress

This chapter covers the estimation of the level of mechanical stress induced by temperature and thermal expansions. The results from the thermal-mechanical simulations are used in mechanical fatigue simulations to furthermore estimate the lifetime caused by cyclic temperatures. The Finite Element Analysis (FEA) tool is used for this modeling.

Degradation caused by high temperature fields is not only due to the accelerated thermal oxidization of winding coating polymers. In order to improve the heat transfer behaviors of traction motors within the limited space of a vehicle, traction motors apply different types of epoxy impregnation, which have much higher thermal conductivities than air and varnish. The application of epoxy impregnation, on one hand prevents the winding coating from direct contact with air, therefore preventing thermal oxidization. On the other hand, the different thermal expansion ratios and the different temperature distribution between epoxy and winding coating and winding copper cause thermally induced mechanical stress. If the induced mechanical stress reaches the yield stress or ultimate tensile stress of a specific material (depending on the different definitions of material failure), material failure will occur. In addition, if the induced mechanical stress is below the level of the stress limitation, the cyclic mechanical stress will gradually degrade the materials and mechanical fatigue will occur. If the primary insulation of the electrical machine, for instance the polymer coating of the enameled wires,

cracks due to mechanical fatigue, failure of the electrical machine take place. Articles [54, 55] discuss in detail the physical aging phenomenon of polymers, except for the chemical oxidization aging, which provides an insight into how mechanical stress could age materials.

4.1 Background

4.1.1 Fatigue caused by thermal-mechanical stress

Thermally induced mechanical stress due to the difference between thermal expansion coefficients and mechanical stress related cycle life is studied widely in many fields and applications.

[56–59] discuss the influences of thermal induced mechanical stresses on LED (Light Emitting Diode), IGBT (Insulated-Gate Bipolar Transistor), PBGA (Plastic Ball Grid Array) and FPGA (Field Programmable Gate Array), respectively. [60] presents both analytical and numerical simulations in 2D on thermal induced stress of two-phase composites. [61, 62] also present the 2D numerical simulation results on the thermal induced stress and the associated cracking effects of the two-phase cement-based material. [63] discusses thermal-mechanical modeling of laminates with fire protection coating. In the case of the automotive industry, thermal induced mechanical stress and fatigue analyzes are carried out on brake discs, engine cylinder heads and after treatment systems as discussed in [64, 65].

Furthermore, some studies such as in [66, 67] are carried out to characterize the stress-strain relationships of polymeric materials and other studies such as [68–70] focus on the stress versus cycle life, i.e. S-N curve. All these studies are valuable inputs to estimate thermal induced mechanical stress and its induced cycle life.

In conclusion, the mechanical stress induced by thermal stress and the resulting degradation is studied in many different fields but not enough for traction electrical machines. One of the reasons is that the thermal-mechanical stresses are less severe when electrical machines run with constant load for industrial usage than cyclic load, to which traction motors are exposed. This problem is also overlooked when varnish is used for machine impregnation due to the similarity of thermal expansion ratios between varnish and winding. However, with the development of material technology that facilitates the high power density designs and

improves the heat transfer performance, the issue of mechanical stress induced by thermal expansion is another challenge to be investigated by electrical machine designers.

4.1.2   Static and transient structural models

As mentioned at the beginning of this chapter, the results from the thermal - mechanical simulations are used in mechanical fatigue simulations to furthermore estimate the lifetime caused by the cyclic temperatures. After obtaining the cyclic temperature load, there are two methods for the continued structural simulations. One approach is to perform a transient structural simulation directly, using the simulated temperature-time history (method 1 in Fig. 5.1). Another approach is to perform a static structural simulation after obtaining the discrete thermal cycles from a cycle counter, which contains all the information of each representative thermal cycle (method 2 in Fig. 5.1). As mentioned in [71–73], the distinction between the static and transient structural simulation types is whether the applied action has enough acceleration when compared to the structure's natural frequency. If a load is applied sufficiently slowly, the inertia forces can be ignored and the analysis can be simplified as static analysis and quasi-static analysis could be performed instead of real dynamic analysis. In comparison to the natural frequency of the electrical machine, the frequency of the temperature load is much slower. Therefore the thermal-mechanical simulations in this work are carried out by static simulations.

4.2   Analytical equations

This section derives the analytical equations of thermal induced stress for a single bar geometry and the geometry with two layers of bonded material. The analytical equations reveal the relationships between the thermal-mechanical stresses and various affecting parameters.

4.2.1   Thermal-mechanical stress of a single bar

A change in the temperature of an object corresponds to a change in its dimensions [74]. If the temperature of the object is uniformly distributed, the material will undergo a uniform thermal strain ε_t which can be expressed by Equation 4.1.

$$\varepsilon_t = \alpha \Delta T \tag{4.1}$$

in which α is the coefficient of thermal expansion (CTE) with unit 1/K or 1/°C and ΔT is the increase in temperature with unit K or °C. A positive ε_t means the object is expanded and a negative ε_t means the object is compressed.

However, if the bar has both ends fixed as shown in Fig. 4.1 and is exposed to uniform temperature increase ΔT, reaction R will be developed over the bar and the bar will be subjected to compressive stresses. However, the thermal expansion in the transverse direction does not produce any stress as there are no constraints or supports applied. Therefore, the problem can be simplified to a 1D problem in the axial direction. From another point of view, assuming that the fixed support at the right end in Figure 4.1 is removed and the same uniform temperature is applied, with force R applied from the right support pointing to the left, the bar will still keep its original length L in the axial direction. The displacement produced by force R on the bar is

$$\delta_R = \frac{RL}{EA} \tag{4.2}$$

where E is the modulus of elasticity or tensile modulus of the material with unit Pa and A is the cross-sectional area of the bar.

Fig. 4.1 Bar with both ends fixed [75]

Besides, the displacement induced by thermal expansion is equal to the force R induced displacement as shown by Equation 4.3. As a result, the expression for the force R is derived as Equation 4.4.

$$\delta_R - \delta_t = \frac{RL}{EA} - \alpha \Delta T L = 0 \tag{4.3}$$

$$R = EA\alpha \Delta T \tag{4.4}$$

Therefore, the induced stress in the bar is

$$\sigma = \frac{R}{A} = E\alpha \Delta T = E\varepsilon_t \tag{4.5}$$

As shown in Equation 4.5, the thermal induced stress over a single bar is proportional to its tensile modulus, thermal expansion coefficient and change in temperature, but not related to the total length.

4.2.2   Thermal-mechanical stress of bonded layers

If materials with different CTE are bonded, for instance, an enameled wire with copper and coating and bonded with epoxy, thermal mechanical stress will be developed even if all the materials are heated uniformly. Chen and Nelson proposed in [76] the analytical model estimating the stress distribution in bonded materials influenced by differential expansion or contraction of the materials, in 1979. For the convenience of discussion of the analytical calculations, the parameters and their corresponding meanings are shown in Table 4.1.

Table 4.1: Parameters and SI units for the thermal induced stress calculation of two layers joined by one bonded joint

σ	Pa	shear stress
α	ppm/$^\circ$C	CTE
t	m	thickness of the two side layers
L	m	total axial length
η	m	thickness of joint layer
E	Pa	tensile/elastic modulus
G	Pa	shear modulus
ΔT	K or $^\circ$C	temperature change

Fig. 4.2 is a sketch showing 3 layers (layer 1, layer 2 and the joint layer) of different materials bonded together. It could be analogous to an enameled wire with copper (layer 1 if the top boundary is symmetrical) and coating (joint layer) bonded with epoxy (layer 2).
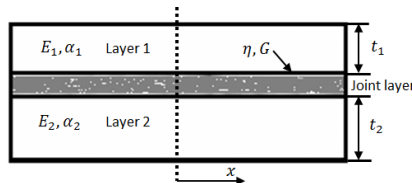

Fig. 4.2 Bonded multi-layers

Equation 4.6 shows the thermal induced shear stress in the x-axis (Fig. 4.2) direction.

$$\sigma = \frac{(\alpha_1 - \alpha_2)\Delta TG \sinh \beta x}{\beta \eta \cosh \beta L} \tag{4.6}$$

where

$$\beta^2 = \frac{G}{\eta}\left(\frac{1}{E_1 t_1} + \frac{1}{E_2 t_2}\right) \tag{4.7}$$

According to [76], physically the shear stress is zero at the center (marked by a dashed-line in Fig. 4.2), and increases gradually to a maximum at the free edge. The value of this maximum stress is obtained when $x = L$ and is expressed by Equation 4.8.

$$\sigma_{max} = \frac{(\alpha_1 - \alpha_2)\Delta TG \tanh \beta L}{\beta \eta} \tag{4.8}$$

Often it may be sufficient to take $\tanh \sim 1$ and use the estimate

$$\sigma_{max} = \frac{(\alpha_1 - \alpha_2)\Delta TG}{\beta \eta} \tag{4.9}$$

Equation 4.9 shows that the thermal induced stress in the joint layer is proportional to the CTE differences between the two layers bonded to it and the temperature change. The reference point of the 'temperature change' is the temperature at which the material has zero compression or elongation stress. The thermal induced stress in the joint layer also increases if the thickness or the tensile modulus of layer 1 and 2 (Fig. 4.2) are increased, or the thickness of the joint layer itself is decreased. Furthermore, it shows that even though the maximum shear stress of the joint layer is obtained when $x = L$, the maximum stress level is not related to the total axial length L.

4.3 Single wire Finite Element Analysis

In the previous section, the thermal-mechanical stresses are derived in a simplified one-dimensional (1D) manner, which helps to define the physics of the problem. However, in the real case of an epoxy impregnated traction motor stator, the thermally induced stresses are generated not only in 1D but in multiple dimensions and multiple materials. In order to capture more accurately the thermal-mechanical stresses, an Ansys 3D Static Structural simulation package within Ansys workbench is used to simulate the thermal induced mechanical stress.

4.3.1 Stress vector and Von Mises stress

The stress vectors of an infinitesimal cube in a structure Finite Element Analysis (FEA) is shown in Fig. 4.3. σ_x, σ_y and σ_z are the tensile stresses which act along the axes, and σ_{xy}, σ_{yz} and σ_{xz} are the shear stresses which act within planes. Similarly to a 1D problem described by Equation. 4.5, the stress and strain relation in the 3D structure FEA is shown in Equation. 4.10.
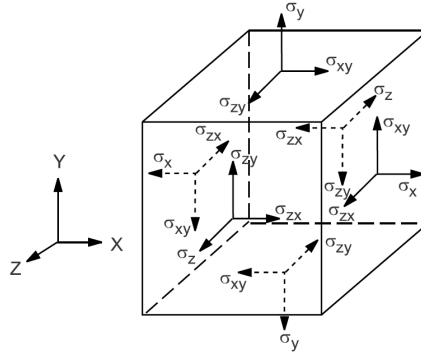
Fig. 4.3 Stress vectors of an infinitesimal cube [77]

$$\{\sigma\} = [E]\{\varepsilon_{el}\} \tag{4.10}$$

where:

$\{\sigma\}$ = stress vector = $[\sigma_x, \sigma_y, \sigma_z, \sigma_{xy}, \sigma_{yz}, \sigma_{xz}]^T$

$[E]$ = tensile/elastic modulus matrix

$\{\varepsilon_{el}\}$ = elastic strain vector

Testing of the fatigue and yield stress is usually carried out on specimens with uni-axial direction forces, however the stresses calculated from FEA simulations are in 6 directions as shown in Fig. 4.3. In structure FEA simulations, Von-Mises stress is introduced to evaluate the total state of all the stresses as a scalar for the convenience of comparison between the tested stresses and simulated stresses. The Von-Mises stress (σ_{vm}) is defined by Equation. 4.11 [77, 78].

$$\sigma_{vm} = (\frac{1}{2}[(\sigma_x - \sigma_y)^2 + (\sigma_y - \sigma_z)^2 + (\sigma_z - \sigma_x)^2 + 6(\sigma_{xy}{}^2 + \sigma_{yz}{}^2 + \sigma_{xz}{}^2)])^{\frac{1}{2}}$$
$$\tag{4.11}$$

4.3.2 Simplified geometry

Fig. 3.5 [51] shows a simplified sketch of three types of commonly used winding configurations. Fig. 4.4 (left) shows the distribution of the wires in a full stator slot, assuming perfect distribution with a constant distance between each pair of strands. In comparison to the total axial length, 220 mm of the windings, which includes an active winding length of 200 mm and end winding length of 10 mm at each side, the dimension of each wire (Table 4.2) is relatively small. Therefore, if the stresses in the thin layer of coating are of interest, a 3D simulation of the full geometry as shown in Fig. 4.4 (left) will hardly develop a good quality mesh, and provide accurate results.

A simplified geometry is proposed as shown at the right of Fig. 4.4, which is the top to bottom view of a 3D sketch of the simulated geometry. The sketch of the simplified simulation geometry shows one quarter of an enameled wire (DAMID 200) with surrounding epoxy, and its boundary conditions. In the axial direction a part of the axial length is simulated. According to Equation 4.9, the maximum shear stress is not related to the axial length, though the stress generated in the transverse direction could be slightly influenced by the axial length in terms of total cross-sectional area. However, too short a simulated axial length also influences the stress distribution. Taking these factors into consideration, a suitable simulated axial length is chosen to be at least two times longer than the maximum modeled radial section.
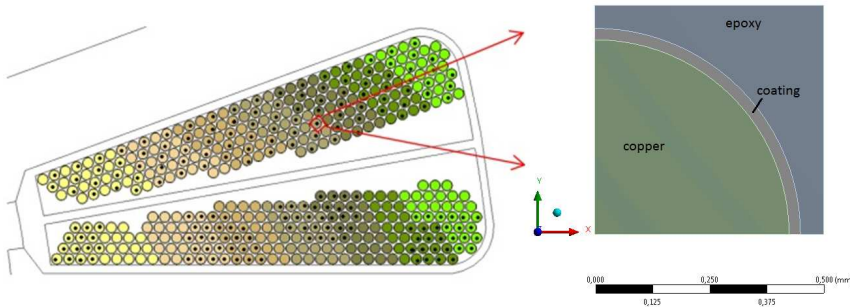

Fig. 4.4 2D view of the wire distribution in one slot (left); simplified geometry of one quarter of a winding with surrounding epoxy (top to bottom view of a 3D sketch) (right)

Table 4.2: Dimensions of enameled wire (DAMID 200)

	copper wire radius	coating thickness
[mm]	0.425	0.025

4.3.3 Materials

The material properties used in the simulations are presented in Table 4.3. According to [79], the Poisson's ratio ν defines the relation between lateral strain and the longitudinal strain and it also defines the relation between the Young's modulus E, shear modulus G and bulk modulus K as shown in Equation 4.12 and 4.13.

$$G = \frac{E}{2(1+\nu)} \tag{4.12}$$

$$K = \frac{E}{3(1-2\nu)} \tag{4.13}$$

Table 4.3: Material data used for thermal-mechanical simulation

	Epoxy 4260	Epoxy LORD	PAI coating	Copper	Steel	Alum-inum
Young's modulus[Pa]	3.5E9	15.2E9	7.4E9	1.1E11	2E11	7.1E10
Poisson's ratio	0.44	0.44	0.42	0.34	0.3	0.33
Yield strength [MPa]	-	-	25	280	2.5E8	2.8E8
Tensile strength [MPa]	65	-	250	430	4.6E8	3.1E8
CTE [ppm/°C]	70 or 155	14	16	18	12	23
Thermal conductivity [W/(m·K)]	0.5	-	0.2	400	26.9	255

4.3.4 Boundary conditions

The simplified 2D sketch in Fig. 4.5 is used to clearly explain the boundary condition settings for the simplified geometry. In comparison to Fig. 4.4, a slot divider

and detailed slot opening are not included and only a smaller number of wires (yellow) in a symbolic slot (gray) are shown in this magnified figure to emphasize the middle wire, which is marked within the black box. Due to the symmetric nature of the middle wire, only one quarter of the wire (red region) is analyzed.
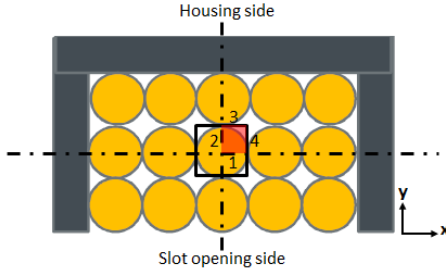

Fig. 4.5 Simplified sketch of windings and slot

The boundaries at the top and bottom surfaces (along the z direction) of the 3D simulation are 'free to move' and 'symmetrical', respectively, although these cannot be shown in the 2D sketch. With the winding configuration shown in Fig. 4.5, boundaries 1 and 2 are set to be symmetrical along the y and x direction, respectively.

Boundary 3 and its movement along the y direction is interesting to analyze, becasue the stator inner surface and slot opening are not mechanically restricted and can induce thermal expansion and displacement towards the $+y$ and $-y$ direction, respectively. As a result, boundary 3 is allowed to have a certain degree of free expansion until it reaches the displacement restriction set by the thermal expansion of the stator and slot wedge at the slot opening. 'Free expansion' in this context means that the body can thermally expand without further inducing additional mechanical stress in the body. One extreme scenario is that the stator inner surface together with the slot opening side expands more than the total thermal expansion as required by the windings and their impregnation. Hence, boundary 3 can be assumed as a 'free to move' boundary, which induces the lowest mechanical stress due to thermal expansion compared to other settings at this boundary. Another extreme scenario is that if an infinite number of wires along the y direction is assumed, boundary 3 is locked, i.e. free expansion is not permitted. This induces the highest thermal-mechanical stress in comparison to other settings of boundary 3.

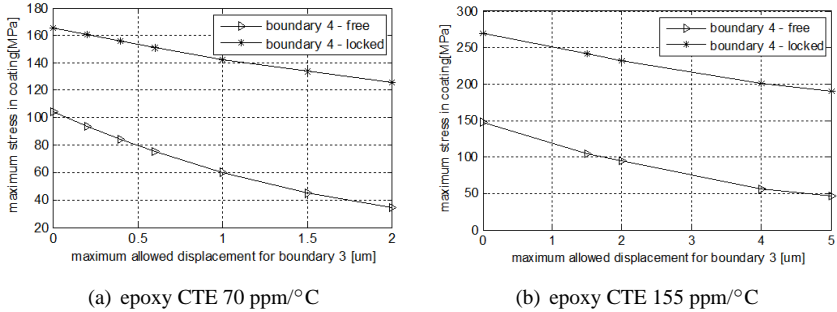(a) epoxy CTE 70 ppm/°C   (b) epoxy CTE 155 ppm/°C

Figure 4.6: Maximum stress of coating at height 2.9 mm with wire temperature 140°C and epoxy thickness 0.05 mm

In comparison to the large industrial machines, electrical machines used for traction have relatively smaller diameters and a rather high number of wires along the y direction (Fig. 4.5 and Fig. 4.4). Hence, in the traction machine, the permitted displacement for free expansion of each wire is smaller, thereby inducing a higher level of thermal-mechanical stress, although the thickness of epoxy bonded to each wire is bigger for larger machines.

Settings of boundary 4 could also be different due to different winding filling factors and the thermal expansion of stator teeth. Similarly to boundary 3, the higher the filling factor of windings in a slot, the lower the exposed degree of freedom for boundary 4.

A sensitivity study is carried out with varied maximum allowed displacement for boundary 3 and with boundary 4 either 'free to move' or 'locked'. The simulated length (in the z direction) is 3 mm, the thickness of epoxy is 0.05 mm and the wire temperature is 140°C. The results with two different values of CTE of epoxy are presented in Fig. 4.6(a) and Fig. 4.6(b), which are 70 ppm/°C and 155 ppm/°C, representing the epoxy before and after glass transition, respectively. The plotted stress is the maximum Von-Mises stress inside the coating layer. As a clearer comparison, Table 4.4 illustrates the maximum thermal-mechanical stress of wire coating in four extreme cases.

As shown in Fig. 4.6 and Table 4.4, in comparison to the case where boundaries 3 and 4 are both 'free to move', the thermal-mechanical stress level of wire coating increases approximately 6 to 7 times for the case where both boundaries

Table 4.4: Maximum stress [MPa] with wire temperature 140°C and epoxy thickness 0.05 mm

	epoxy CTE 70 ppm/°C	
Boundary 4	Boundary 3	
	Free to move	**Locked**
Free to move	27	104
Locked	104	166
	epoxy CTE 155 ppm/°C	
Boundary 4	Boundary 3	
	Free to move	**Locked**
Free to move	41	148
Locked	148	270

are fully 'locked'. It also shows that the induced mechanical stress on the coating is increased by approx. 1.5 times, if the CTE of epoxy is increased from 70ppm/°C to 155ppm/°C, which is caused by the glass transition of the epoxy 4260.

As shown above, an increased winding filling factor will change the boundary conditions of boundaries 3 and 4 from 'free to move' to 'locked', which shifts the thermal induced mechanical stress level in the coating, as shown in Fig. 4.6, from the right bottom corner to the left top corner, when other conditions are the same. However, a higher filling factor may also mean a thinner average thickness of impregnation material, which could decrease the level of the thermal-mechanical stress. Besides, some educated guesses are discussed as below, and the verification of them could be interesting future work. If the machine stator temperature is fixed, i.e. the maximum permitted total displacement is known, an optimum winding filling factor may exist to minimize the mechanical stress induced by thermal stress. From another perspective, with a known winding filling factor of a slot, there may be an optimum temperature difference between the stator and windings, so that the stator does not restrict the thermal expansion of the windings and their impregnation, and therefore the thermal induced mechanical stress of coating is kept to the lowest stress level (right bottom corner in Fig. 4.6(a) and Fig. 4.6(b)).

4.3.5   Simulation examples

This part shows some sensitivity study examples of the simulation model discussed above.

Sensitivity study - axial length

In order to study the axial length effect on the stress level for different bonded layers, a sensitivity study is carried out with varied axial lengths but with the remaking geometrical, material properties and the boundary conditions being identical. The temperature is set to 100°C in all the simulated cases with boundaries 3 and 4 'locked', epoxy thickness 0.05 mm and CTE 70 ppm/°C. The thermal induced mechanical stress ranges across the total volume of different materials are shown in Table 4.5.

The simulation results show that the ranges of the induced stress over different bonded layers are not influenced by the length changes if the simulated length is not too short. Meanwhile, the times for meshing and computing of the simulations are increased noticeably with the increased axial length from 4 mm to 40 mm. Mesh problems start to show up when the axial length of the model is greater than 40 mm, which is approx. 80 times the maximum dimension in the $x - y$ plane (Fig.4.4). Therefore, a suitable simulated axial length is chosen to be at least two times larger than the maximum dimension of the $x - y$ plane (Fig.4.4), to avoid distortion of the stress distribution and the unnecessary meshing and computing time.

The results from this study also agree with the conclusion derived by analytical equations (Equation 4.9) that the shear stress is zero at the center (marked by a dashed-line in Fig. 4.2), and increases gradually to a maximum at the free edge. The value of this maximum stress is obtained when $x = L$.

Sensitivity study - epoxy thickness

A uniform temperature of 230°C is applied in the following single wire simulation. The simulated axial length is 3 mm and the CTE of epoxy is 70 ppm/°C with the boundaries 3 and 4 set to be 'locked'.

As shown in Fig. 6.8, in practice the winding is randomly distributed in a slot and the thickness of epoxy is not the same between every two wires. The following compares the thermal-mechanical stresses in two simulation cases to demonstrate

Table 4.5: Sensitivity study of axial length influences on induced thermal-mechanical stress

Spatial evenly distributed temperature 100°C			
Axial length [mm]	Copper [MPa]	Coating [MPa]	Epoxy [MPa]
40	7.2241-330.46	44.456-143.25	7.2241-92.973
20	7.2241-331.69	44.456-143.48	7.2241-92.974
10	7.2241-331.81	44.456-141.78	7.2241-92.972
4	7.2241-330.74	44.456-143.4	7.2241-92.974
0.5	7.7693 -330.57	45.85-142.68	7.7693-92.976

the influences of epoxy thickness. In one case with the epoxy thickness is 0.05 mm and the in other case it is 0.45 mm.

Due to the fact that the stress is a derivative value of force over area, FEM mechanical simulation induces quite a large error at the free to move edge, i.e. the top edge in the simulations, which leads to a great stress increase as shown in the left sides of Fig. 4.7 and Fig. 4.8. Therefore, the stress integration over a line excluding the first few layers of cells close to the top edge is obtained as shown in the right sides of figure of Fig. 4.7 and Fig. 4.8.

In most part of the coating, Fig. 4.7 (thin layer of epoxy) and Fig. 4.8 (thick layer of epoxy) show the induced stress of 104 MPa and 130 MPa, respectively. Also, the maximum stress induced in coating is higher when bonded with thicker epoxy which agrees with the analytical Equation 4.9.

Sensitivity study - material

If the above-mentioned epoxy 4260 is replaced by the LORD epoxy, the maximum Von-Mises stress in coating decreases to almost one third as illustrated in Fig. 4.9 in comparison to Fig. 4.8. The decrease of mechanical stress mainly because of the smaller difference of CTE between the LORD epoxy, the coating and the copper, even though the Young's modulus of this epoxy is greater than that of epoxy 4260.

4.3.6 Limitations

There are limitations to the use of the single wire thermal-mechanical model to estimate the highest mechanical stress of winding coatings inside a slot, because it only simulates the thermal-mechanical stress induced on winding coatings that appear at the hot spot region inside a slot, which is usually in the middle of a
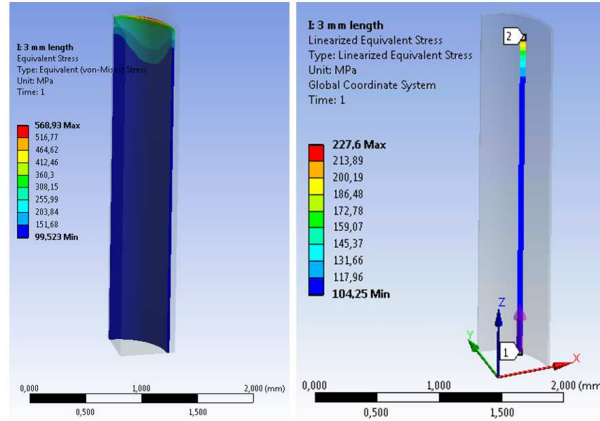
Fig. 4.7 Von-Mises stress over the volume of coating (0-3mm) (left); Von-Mises stress over one line inside the coating excluding the end effects (0-2.8mm) (right), coating thickness 0.05 mm

slot as shown in Fig. 4.10. However, the highest thermal-mechanical stress of the winding coating could be shifted from the hot spot of the winding to the outermost layer of the winding, which is closest to the stator core. The reasons could be because of the big CTE difference between coating, epoxy and steel as well as a high average temperature in each material. Article [80] discusses this phenomenon in detail by means of an 8×8 wires structure (4×4 in plots because of the symmetrical geometry). If the maximum permitted stress is interested to further evaluate the maximum thermal or current loading, multiple wires or a full slot model are needed, which will estimate the stresses over the space within a slot, thereby accurately identifying the location of the maximum stress.

However, to evaluate the fatigue lifetime caused by mechanical stress induced by a thermal cycle, the single wire model is sufficient and convenient, for the following reasons:

1. The fatigue lifetime is not only decided by the maximum stress level but also by the depth of the stress cycle, which will be discussed in detail in Chapter 5.6.2. Much deeper thermal cycles usually appear at the hot spot inside a slot rather than at the windings close to a slot iron, indicating that the threshold for lifetime induced by thermal cycles and mechanical stress cycle fatigue is set by the coating properties in the hot spot region.
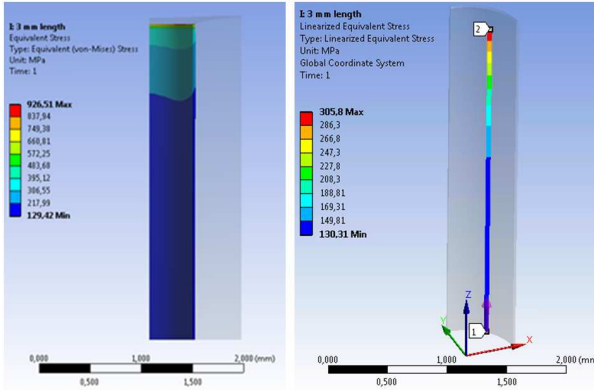
53

Fig. 4.8 Von-Mises stress over the volume of coating (0-3mm) (left); Von-Mises stress over one line inside the coating excluding the end effects(0-2.8mm) (right), coating thickness 0.45 mm

2. During the actual usage of a machine, the stator and the outermost windings close to the slot are exposed to much lower temperatures (see Fig. 7.29 and Fig. 7.34), compared to those of Fig. 4 in article [80]. Also, the temperature gradient between the hot spot inside the slot and outermost layer of the winding is steep, because of the low thermal conductivity of the wire bundles in the radial direction, as shown in Fig. 4.10. Taking the above-mentioned factors into account, the thermal-mechanical stresses of coatings in the outermost layer of windings are dropped because of the lower average temperature in this region, but the stresses in the middle of the slot are increased due to the more restricted displacement for thermal expansion.

The single wire model is used to estimate the lifetime due to mechanical fatigue of the dynamic temperatures.
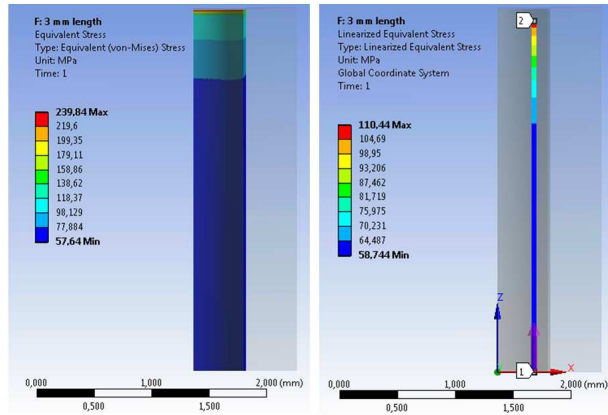
Fig. 4.9 Von-Mises stress over the volume of coating (0-3mm) (left); Von-Mises stress over one line inside coating exclude the end effects (0-2.8mm) (right), with LORD epoxy and thickness 0.45 mm
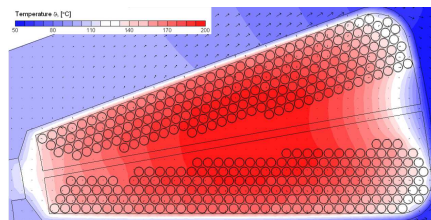

Fig. 4.10 Example of 2-D temperature distribution in a slot

55

Chapter 5

Modeling and simulation - drivetrain level

5.1 System modeling overview

Apart from the simulations on component level as discussed in the previous two chapters, the study is also extended to the system level taking into account the applications of electrical machines. This chapter presents the system modeling used to estimate the electrical machine temperature distribution and lifetime due to thermal and thermal-mechanical stresses with known driving cycles. The flowchart in Fig. 5.1 shows the holistic structure and steps to perform the above-mentioned simulation. The parts in the solid-line boxes and the dashed-line boxes in Fig. 5.1 are the models as required and the corresponding inputs/outputs of each model, respectively.

The simulation models, which are used to build the final completed system model are: a drivetrain model, an electromagnetic model, an analytical cooling/ CFD model, a thermal model, a cycle counter model, a thermal degradation model, a structural model and a mechanical fatigue model. Apart from the structural FEA model, which is discussed in Chapter 4, the other models are presented in this chapter in detail.

Two thermal models, a Lumped Parameter Analysis (LPA) model and a Finite Element Analysis (FEA) model, are studied. They are adapted to two different in-house designed traction electrical machines, which are applied in a passenger car

and a four-wheel drive wheel loader, respectively. For the convenience of discussion, the electrical machine for passenger car is called the **RWD machine** or **EM1** and that used for wheel loader is called the **VCE machine** or **EM2**. Both above-mentioned thermal models can be used to predict the machine temperature distribution from known driving cycles. However, the integration levels between the thermal model and the drivetrain model are different. The LPA model is built in Matlab Simulink and is easily integrated with or embedded in a drivetrain model, which is also built in Matlab Simulink. However, due to the complexity level of the FEA model, the drivetrain model and the FEA model are applied separately one after another.

With the knowledge of the temperature distribution in an electrical machine, cycle counters such as Mean edge 2 and Rainflow methods are applied to calculate the mean/average, amplitude/range/depth, duration and the total number of each temperature cycle. The output from the cycle counter is an important input for the thermal degradation model to estimate the lifetime reduction of the Electrical Insulation System (EIS) due to thermal oxidation of enameled wires.

Apart from this, with the discrete thermal cycles from a cycle counter, which contains all the information of each representative thermal cycle, static structural simulation to calculate the thermal-mechanical stress can be performed (method 2 in Fig. 5.1). Another method of carrying out the structural simulation is to perform a transient simulation directly with the simulated temperatures in relation to the operation time (method 1 in Fig. 5.1). Compared to method 2, the transient simulation results in more accurate results, although it takes up a much longer simulation time. In this study, method 2 is used and the resulted thermal-mechanical stress is fed to another cycle counter followed by a mechanical fatigue model, which covers the degradation caused by the cyclic effects of the dynamic temperatures. The simulation results are presented and discussed in Chapter 7.
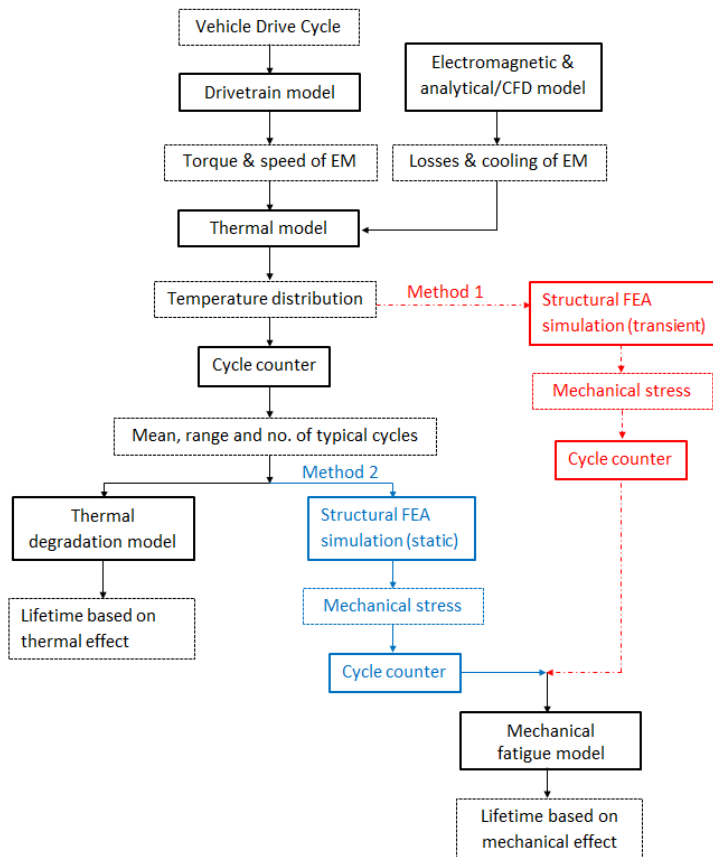
Fig. 5.1 Flowchart of system simulation

5.2 LPA thermal model with driving cycles

5.2.1 Drivetrain model

As shown in Fig. 5.2, the hybrid powertrain mechanics are simulated by Matlab Simulink, which dynamically outputs the electrical machine load points as inputs to the thermal LPA. The powertrain model contains power flow control, an internal combustion engine (ICE) model, an electrical machine model, a brake control model, a mechanical dynamics model and a road model.
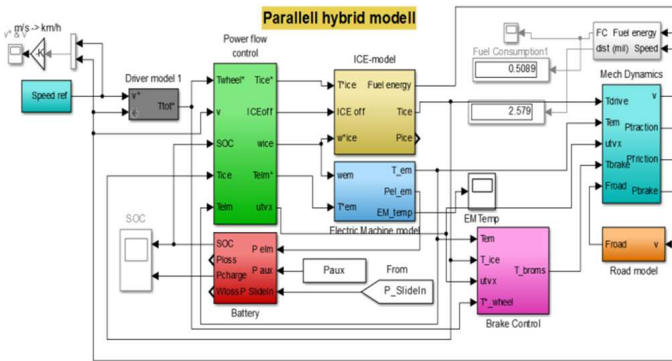
Fig. 5.2 Top layer of the parallel hybrid model [81]

5.2.2 Driving cycle

The high speed (US06) driving cycle is studied with the RWD machine. Fig. 5.3 shows the US06 driving cycle, which contains the total driving time, speed, acceleration of the studied vehicle and slope of the road.

5.2.3 RWD machine parameters and thermal model

The studied motor EM1/RWD machine is designed to work with a 300V DC link voltage, and to provide 14.3 kW continuous power and 30 kW peak power. The field weakening ratio is 1:5 and the maximum speed of the motor is 15,000 rpm at 150 km/h. The nominal torque is 40 Nm at 3,000 rpm and peak torque 100 Nm [81].
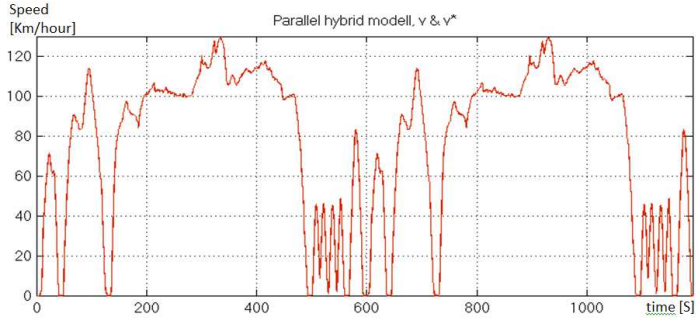
Fig. 5.3 US06 driving cycle

The 8-node Lumped Parameter thermal model (model 3 in Fig.1) is presented in Fig. 5.4 as developed in [82]. The chosen nodes are the winding active component, the winding end component, the stator yoke, the stator teeth, the rotor magnets, the rotor core, the rotor shaft and the bearings. The forced convection inside the housing is considered to be the thermal resistance between node 1 and ambient, which is not shown in Fig. 5.4. More information and detailed settings of the materials and boundary conditions of the thermal model of RWD machine are presented in Chapter 5 in [81].

Fig. 5.4 Lumped Parameter Model for an electrical machine

5.2.4 Loss maps

Losses in the simulated EM1/RWD machine are obtained by FEA simulations by FEMM. Fig. 5.5 and 5.6 show the losses in the copper and stator core at various speeds and torques, respectively [3, 81, 82].
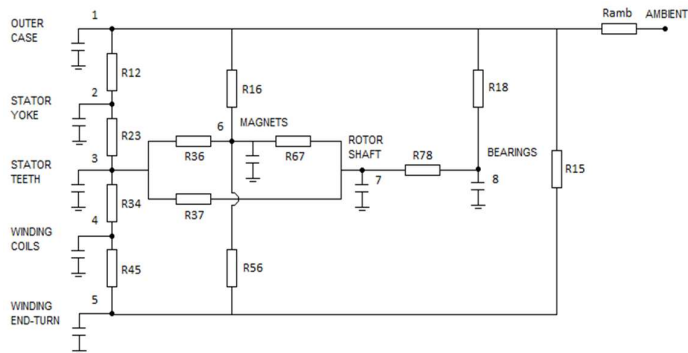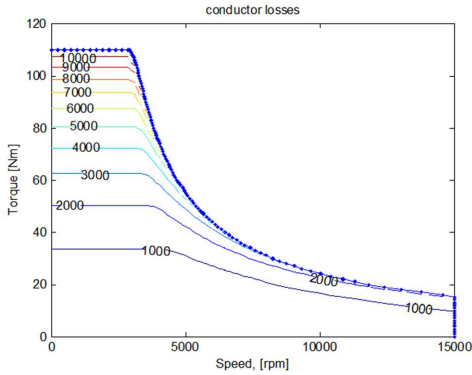

Fig. 5.5 Simulated copper loss in the stator
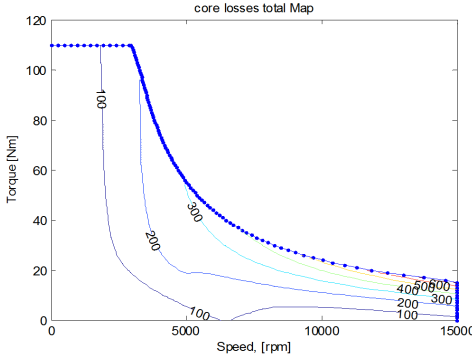
Fig. 5.6 Simulated core loss in the stator

5.3 FEA thermal model with driving cycles

5.3.1 Driving cycles

A Short Loading Cycle (SLC), as shown in Fig 5.7, is one of the frequently used driving cycles of wheel loaders (WL). This driving cycle starts with lifting of the load from ground level (point 1) and moving backwards to the reversing point (point 4) and then moving forward for several meters and avoid collision with pallets already loaded onto the load receiver [83]. At point 6 the WL stops, lowers the load and places it on the load receiver's deck, and then moves back to the initial loading position (point 1) [83].
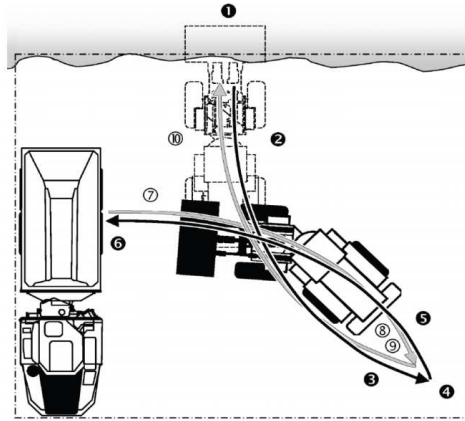
Fig. 5.7 Numbered sequence of actions in a short loading cycle, point 4 is the reversing point, picture from [83]

5.3.2 Loss maps

Losses of the VCE machine are obtained by FEA simulations by Maxwell, Ansys. Figs. 5.8 and 5.9 show the losses in the copper and stator core at various speeds and torques, respectively. The calculated loss in the rotor magnets are presented in Appendix C.2.
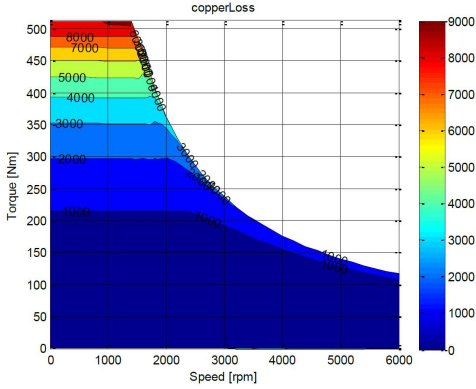
Fig. 5.8 Simulated copper loss in the stator at 120°C of VCE machine
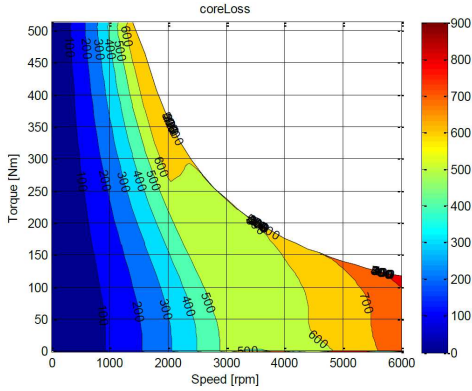
Fig. 5.9 Simulated core loss of VCE machine

5.3.3 VCE machine parameter and thermal model

The EM2/VCE machine is designed to work with a 540 V DC link voltage, and to provide 35 kW continuous power and 250 Nm continuous torque. The rated and maximum speeds of the motor are 1335 rpm and 6000 rpm, respectively [84].

The 2D FE thermal model is a Volvo in-house developed thermal model based on Gmsh as the geometry and meshing tool and Matlab as the solver and post-processing tool. Detailed model building procedures are documented in technical report [84]. Fig. 5.10 shows the geometry of the simulated VCE electrical machine, including the stator yoke, stator teeth, windings, winding insulation (the thin layer between the windings and the stator teeth in Fig. 5.10) rotor magnet, rotor iron, rotor shaft and glass fiber (the thin layer between the rotor magnet and the air gap shown in Fig. 5.10), etc. The materials for the different parts of the machine are listed in table 5.1. Boundary condition 1 to 4 (BC1-BC4) are set to symmetrical and boundary conditions 5 to 8 (BC5-BC8) are set to convection. There are six 'sensor locations' which indicates the locations where the temperatures over time are of interest. Sensor 1 to sensor 6 correspond to stator tooth opening, middle of the winding, stator yoke, shaft, rotor iron and rotor magnet, respectively.
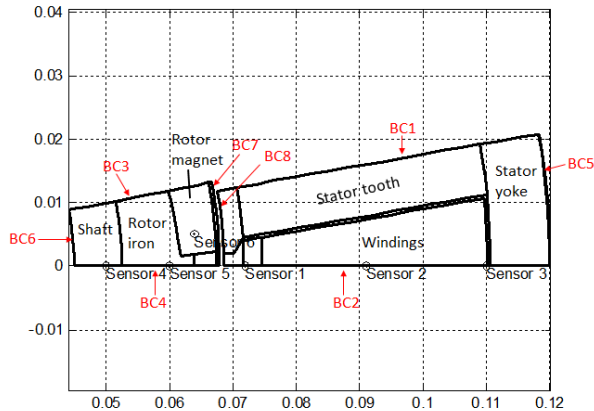
Fig. 5.10 Geometry, material, boundary conditions and sensor locations of the VCE electrical machine thermal model

Table 5.1: Materials list for 2-D FEA thermal simulation of VCE machine

Materials	Thermal conductivity [W/(m·K)]	Specific heat capacity [J/kg/K]
Steel lamination	26.9	450
Winding	2	522
Insulation	0.2	1100
Slot wedge	0.4	1100
Epoxy 4260	0.5	1200
Carbon fiber	3.09	933
Aluminum	255	910
Magnets	5.8	460
Shaft	45	450
Air	0.03	1012

5.4 Cycle counter

Cycle counters are used to count the respective mean/average, amplitude/range/ depth, duration and total number of each cycle of a known load-time history. The above-mentioned 'load' could be temperatures or mechanical stresses. Reference [85] discusses 7 different cycle counting algorithms, which can be used to decompose irregular thermal evolutions into frequencies/periods of depths and number of temperature cycles and mean temperatures. In our study, two most often used algorithms are discussed and the resulting lifetimes are compared later.

5.4.1 Mean edge 2 cycle counter

Fig. 5.11 [86] shows an example of a temperature profile applied to either bearings or windings. Based on this temperature profile, a weighted characteristic life can be evaluated by Equation 5.1 [86] with a known steady state life at specific temperatures. This cycle counting method (so called Mean edge 2 in [85]) counts the small temperature cycles between every two turning points and computes the mean of these maximum edges and minimum edges for the entire temperature profile.
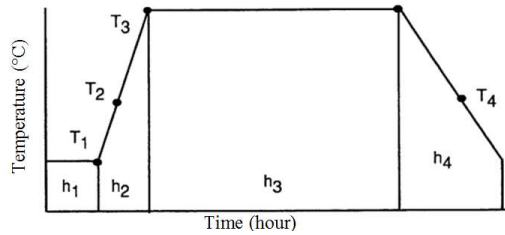
Fig. 5.11 Example of a temperature profile

$$L = \frac{h_1 + h_2 + h_3 + \cdots + h_m}{\dfrac{h_1}{L_1} + \dfrac{h_2}{L_2} + \dfrac{h_3}{L_3} + \cdots + \dfrac{h_m}{L_m}} \tag{5.1}$$

where:
L is the average life time;
h_1 is the time at temperature T_1;
h_2 is the time to cycle from temperature T_1 to T_3;
h_3 is the time at temperature T_3;
h_m is the time at temperature T_m;
L_1 is the winding life at temperature T_1;
L_2 is the winding life at temperature T_2;
$T_2 = \frac{T_1 + T_3}{2}$ and $T_4 = \frac{T_3 + T_1}{2}$.

5.4.2 Rainflow cycle counter

Rainflow counting is another widely used method of estimating stress/strain hysteresis loops within the area of fatigue life estimation [85, 87, 88]. Compared to the method discussed above, the Rainflow counting method is able to count the deepest cycles [85] and also break down the middle depth cycles into small depth cycles within a temperature or mechanical stress profile.

The basic Rainflow cycle counter algorithm is summarized as follows [89]:

1. Rotate the loading history 90° such that the time axis is vertically downward.

2. Imagine a flow of rain starting at each successive extreme point.

3. Define a loading reversal (half-cycle) by allowing each rainflow to continue to drip down these roofs until:
   a. It falls opposite a larger maximum (or smaller minimum) point.
   b. It meets a previous flow falling from above.
   c. It falls below the roof level.

4. Identify each hysteresis loop (cycle) by pairing up the same counted reversals.

With a given load-time history as shown in Fig.5.12, the rotated time loading history is shown in Fig.5.13. The counted reversals and cycles are shown in Table.5.2 and Table.5.3, respectively. Except for the cycle amplitude (range or depth), cycle mean value, number of cycles, the cycle period is also obtained from Rainflow cycle counting, which is not shown in this example in Table.5.3. With these output variables, Equation 5.1 is used to estimate the average lifetime consumed after the machine is exposed to a certain temperature cycle.

Fig. 5.12 Example of a load-time history

Based on the basic Rainflow cycle counting technique, other improved Rainflow cycle counting methods are developed, such as three-point (recommend by [88]) and four-point cycle counting methods [89].
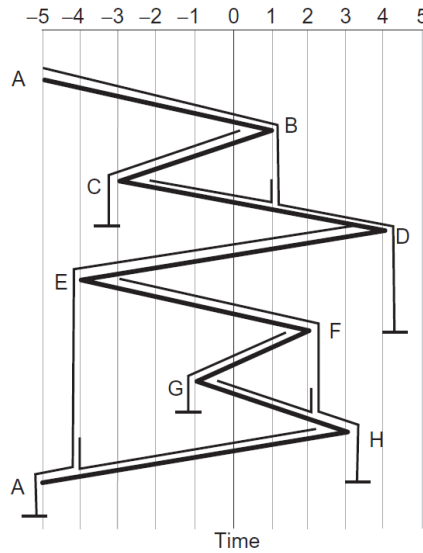
Fig. 5.13 Rainflow cycle counting the loading history

Table 5.2: Reversal counts based on the Rainflow counting technique [89]

No. of Reversals	From	To	From	To	Range	Mean
1	A	D	-5	4	9	-0.5
1	D	A	4	-5	9	-0.5
1	B	C	1	-3	4	-1
1	C	B	-3	1	4	-1
1	E	H	-4	3	7	-0.5
1	H	E	3	-4	7	-0.5
1	F	G	2	-1	3	0.5
1	G	F	-1	2	3	0.5

Table 5.3: Cycle counts based on the Rainflow counting technique [89]

No. of Cycles	Path	Range	Mean
1	A-D	9	-0.5
1	B-C	4	-1
1	E-H	7	-0.5
1	F-G	3	0.5

5.5 Lifetime model due to constant temperature

Electrical insulations (EI) and electrical insulation systems (EIS) are aged with
TEAM stresses, namely Thermal, Electrical, Ambient and Mechanical stresses
(Chapter 1.2). Each stress in relation to lifetime can be described by certain math-
ematical model as summarized in Tables 2.2 and 2.3. This section explains the
lifetime model resulting from constant temperatures.

5.5.1 Thermal Index and Arrhenius Law

The Arrhenius Law (also included in Table 2.2) describes the relation between the
insulation endurance and constant temperatures as shown in Equation 5.2

$$L = Ae^{(B/T)} \tag{5.2}$$

where L is the insulation endurance in hours, T the absolute temperature in Kelvin,
A and B the constants for each insulation type, and e the base of natural loga-
rithms, separately.

The linear function shown in Equation 5.3 is obtained by taking logarithms at
both sides of Equation 5.2

$$Y = a + bX \tag{5.3}$$

where

$$Y = log_{10}L$$
$$a = log_{10}A$$
$$X = 1/T$$
$$b = (log_{10}e)B$$

$$\tag{5.4}$$

According to the standard [21, 26, 90], the temperature index (TI) $N°C$ of EI
or EIS is the temperature at which 50% of total population of the tested speci-
mens fail (i.e. L50), after 20,000 hours of exposure. Fig. 5.14 shows the relation-
ship between the temperatures and the logarithm of the thermal lifetime of enam-
eled wires. Four magnet wires with different coating materials, i.e. polyurethane,
polyester, polyester-imide and polyester plus polyamide-imide, are presented in
the plot, which correspond to TI of 155°C, 180°C, 200°C and 220°C, respec-
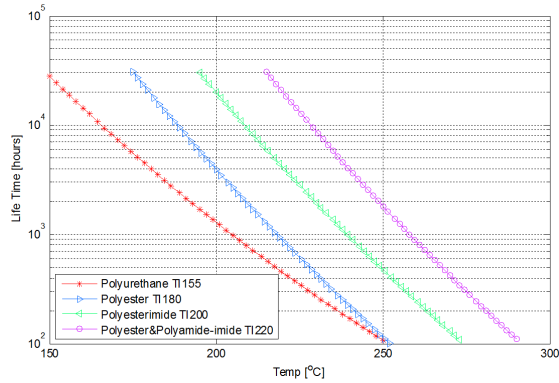tively.

Fig. 5.14 Steady state thermal life of magnet wires coated with different insulation materials [3]

5.6 Lifetime model due to cyclic mechanical stress

5.6.1 High cycle fatigue and low cycle fatigue

Fatigue is the weakening of a material caused by repeatedly applied loads [91]. It is the progressive and localized structural damage that occurs when a material is subjected to cyclic loading [91]. If the loads are above a certain threshold, microscopic cracks will begin to form at the stress concentrators [91].

There are two commonly used approaches to estimate the total life induced by cyclic mechanical stress of a material, which are Stress-Life approach and Strain-Life approach. These two approaches are normally corresponding to high cycle fatigue (HCF) and low cycle fatigue (LCF), respectively. In detail, for LCF the number of the cycles till failure is considerably shortened because materials are under high stress amplitudes with plastic deformations. Meanwhile, HCF refers to fatigue which occurs above certain number of cycles while the materials still work in their elastic regions.

For low cycle fatigue (LCF), Strain-Life model or Coffin-Manson equation (5.5) is used [92] to describe the relation between the plastic strain $\frac{\Delta\varepsilon_p}{2}$ and the total number of cycles till failure N_f.

$$\frac{\Delta\varepsilon_p}{2} = B(N_f)^\beta \qquad (5.5)$$

where B is the empirical constant known as the fatigue ductility coefficient, the

failure strain for a single reversal and β is the empirical constant known as the fatigue ductility exponent [91].

As mentioned above, when the cyclic mechanical stress is high and the materials of interest are in their plastic deformation regions, the LCF model is valid. However, if a material is working in its plastic deformation region, the lifetime of the material is much shortened. Materials show up to 1000 cycles of life if they are in their plastic deformation region as reported in [92] and [93]. Therefore, it is essential to design and operate machines so that materials, for instance the insulation materials, can operate in their elastic regions. In this case, the high cycle fatigue (HCF) model is valid. The HCF model or the Stress-Life model is discussed in detail in the following section.

5.6.2   Stress-Life (S-N) model

Fatigue loading

In an electrified vehicle application, loadings of the electrical machines are very dynamic. This leads to very dynamic stress-time histories which are similar to the one shown in Fig. 5.12. Using a cycle counter proposed in Chapter 5.4 can characterize the dynamic stress-time histories to typical cycles and create certain cycle spectrum as shown in Table. 5.3. Furthermore, for each typical cycle with High Cycle Fatigue (HCF), the Stress-Life (S-N) relationship can be used to estimate the lifetime spending after the whole dynamic cycle is applied. The S-N curves are derived from tests on samples of the material to be characterized where a regular sinusoidal stress is applied by a testing machine which also counts the number of cycles to failure [91]. A typical stress load cycle is shown in Fig. 5.15. Besides the frequency/period time, two of the parameters in Table 5.4 should be defined to describe a cycle as expressed by Equation 5.6.

$$S = S_{mn} + S_a \sin \omega t \tag{5.6}$$

S-N model of PAI coating

The tension fatigue curves of 4 different PAI insulation resins are shown in Fig. 5.16 [94]. In the later calculations, PAI 7130 is assumed to be applied as coating of DAMID 200 wire. Typically, the stress-life (S-N) relation can be described by the power law equation as in Equation 5.7. Furthermore, it can be derived into
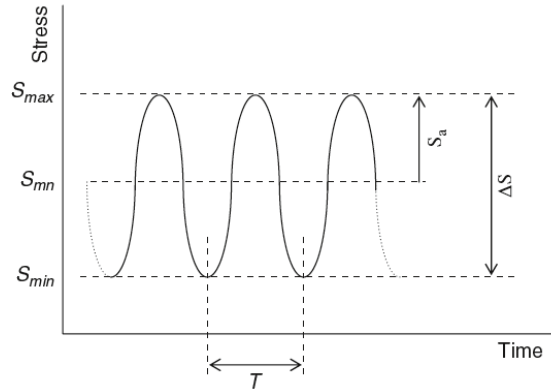
Fig. 5.15 Constant amplitude, constant frequency sinusoidal waveform

Table 5.4: Parameters used to describe fatigue spectra [92]

Maximum stress	S_{max}
Minimum stress	S_{min}
Stress amplitude	$S_a = \frac{S_{max} - S_{min}}{2}$
Mean stress	$S_{mn} = \frac{S_{max} + S_{min}}{2}$
Stress range	$\Delta S = S_{max} - S_{min}$
Stress ratio	$R = \frac{S_{min}}{S_{max}}$
Period	T(sec)
Frequency	$f = \frac{1}{T}$ (Hz)

Equation 5.8, which shows the linear relation between the stresses and number of cycles to failure in a log-log scale.

$$N_1 = N_2 \left(\frac{S_1}{S_2} \right)^{\frac{1}{b}} \tag{5.7}$$

$$b = \frac{\log S_1 - \log S_2}{\log N_1 - \log N_2} \tag{5.8}$$

The coefficient b in Equation 5.8 is found to be 0.1178 for PAI 7130 in Fig. 5.16. Also, the fitted tension fatigue curve for PAI is shown in Fig. 5.17.

The tension fatigue curves in Fig. 5.16 and Fig. 5.17 are useful in predicting the life of the PAI materials. However, it should be noted that the curves can
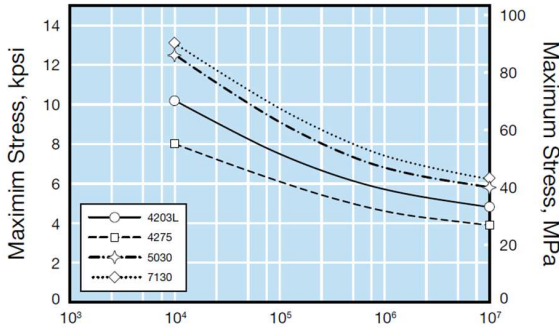
Fig. 5.16 Tension fatigue curves of PAI insulation resins - measured
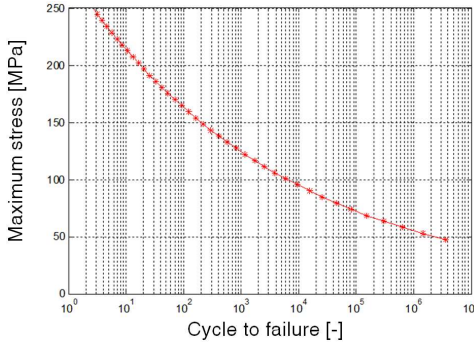
Fig. 5.17 Tension-Fatigue curve of PAI 7130 - fitted

be influenced by some factors for one specific material, for instance the types of loading stress (Fig. 5.18). For a polished 0.3-inch-diameter steel specimen, a lifetime of 10^3 cycles corresponds to 90%, 75% and 72% of the ultimate tensile strength (S_u) in bending, axial and torsion fatigue test, respectively, as shown in Fig. 5.19 [93, p. 321]. $S_n{}'$ is the endurance stress limit of the tested steel in a bending fatigue test.

For the stator windings, the induced thermal-mechanical stresses are a combination of axial stress and bending stress, which refers to shear stress and normal stress on the coating layer in the FEA simulations, respectively. However, the S-N curves in Fig. 5.16 are obtained with tension/tensile fatigue tests. Therefore, the calculated lifetime is expected to be shorter than in the real application.
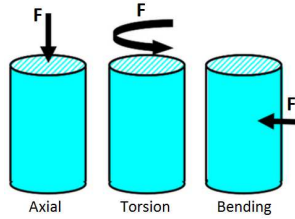
Fig. 5.18 Different types of loading in fatigue tests [95]
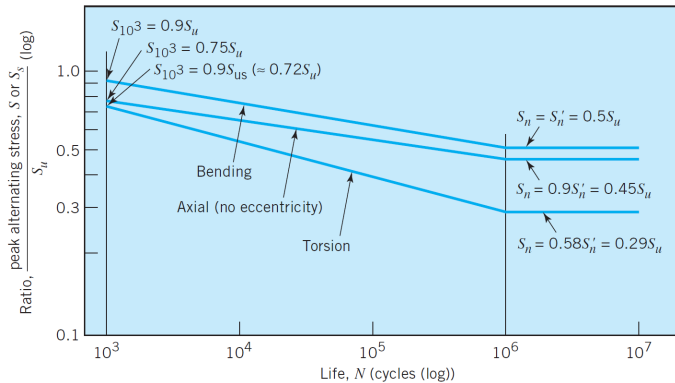
Fig. 5.19 Generalized S-N curves for polished 0.3-inch-diameter steel specimens [93].

Therefore, a more comprehensive S-N fatigue map for PAI coating is needed in order to more accurately estimate the lifetime loss due to mechanical wear. The completed S-N fatigue map should cover the fatigue life at different combinations of mean stress level and stress ratio (or two other parameters defined in Table 5.4), which is similar to the one in Fig. 5.20.

Cumulative damage method

The S-N curve is applicable to constant amplitude fatigue as shown in Fig. 5.15. However in many cases, including traction machine applications, variable amplitude fatigue spectra are experienced. Therefore, a relationship between constant amplitude fatigue with variable amplitude fatigue is needed. According to [92], a simple method to use S-N data to predict variable amplitude fatigue is proposed by Palmgren (1924) and further developed by Miner (1945). Miner assumed that
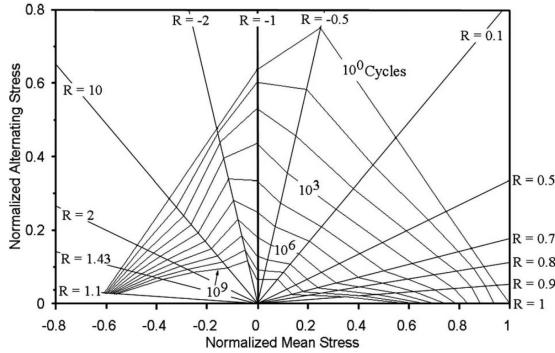
Fig. 5.20 Constant life diagram for E-glass/polyester laminate based on S-N data for 13 R-values, three-parameter mean S-N model [96]

the total amount of work (W) to cause failure in a sample, is a constant, regardless of the amplitude of the fatigue. Therefore if the sample is subjected to a spectrum loading consisting of i blocks, where the work associated with each block is w_i, then:

$$\Sigma w_i = W \tag{5.9}$$

Furthermore, Miner's rule (also included in Table 2.2) assumes that the work absorbed in a cycle is proportional to the number of cycles in the block, n_i, and hence:

$$\frac{w_i}{W} = \frac{n_i}{N_f} \tag{5.10}$$

where N_f is the number of cycles to failure at the stress amplitude for that particular block and can be obtained from the S-N curve. When the accumulated damage occurs, Equation. 5.11 is met. This equation is also named Palmgren-Miner's (P-M) law or the linear damage accumulation model, which is used in this study with results presented in Chapter 7.5.3.

$$\Sigma \frac{n_i}{N_f} = 1 \tag{5.11}$$

5.7 Statistics - Weibull distribution

Chapter 2.3.2 presents two different statistical models commonly used for accelerated life tests. This part focuses on the modeling of Weibull distribution.

A Cumulative Distribution Function (CDF) of a Weibull Distribution function shown in Equation 5.12 [97, 98] is used to calculate the relation between L10 and L50 life (see Chapter. 5.5.1).

$$F(t) = 1 - e^{-\left(\frac{t}{\eta}\right)^{\beta}} \tag{5.12}$$

where β is the shape factor, and η is the characteristic life parameter. Reference [99] presents the database of the shape parameters for various types of equipment and states that the value for AC and DC motors is between 0.5 and 3, with a typical value of 1.2. Takeshi Hakamada [100] carried out break-down voltage tests on 75 motors which had been used for 15 to 23 years and found out that the shape factor for stator windings is between 1.8 and 2.8 for low failure machines. These two sources report comparable shape factors for electrical machines. In the following study, a shape factor of 1.2 is considered to be on the conservative side of life time estimation, which results in an L50 life to L10 life ratio of 4.7.

Chapter 6

Test set-up

This chapter explains the selection of relevant tests, describes the test procedures and measurement techniques, and defines the test set-up and control strategies. The tests are used to investigate the degradation mechanisms and understand the degradation symptoms of the insulation material of enameled wires, the insulation system of motorettes and insulation system of entire electrical machines. The test results are presented in Chapter 7.

6.1   Enamel wire testing

Arrhenius Law in Table 2.2 is the most widely used rule to describe the lifetime of an Electrical Insulation (EI) or an Electrical Insulation System (EIS) at different constant temperatures. In standards [21, 26, 101], the test approaches are described in order to obtain the Temperature Index (TI) of enameled wire, insulation material and polymer, respectively. In order to identify the TI of a material or a combination of materials, several specimens of the material of interest are tested when subjected to at least 3 elevated temperatures. Furthermore the Arrhenius equation is derived to describe the thermal lifetime in relation to different constant temperature levels. The above-mentioned standards suggest that the test specimens should be measured in a temperature controlled oven with good air circulation, which exposes the specimens to an environment at high temperature and in the presence of oxygen. Therefore, the degradation that is measured and concluded is mainly due to oxidation at constant high temperatures.

As described in Chapter 2.2.2, a stator of an electrical machine in an electrified vehicle is usually impregnated by trickle impregnation, dipping impregnation or total encapsulation. The impregnation is applied to enhance the mechanical strength, electrical insulation and thermal conductivity of the coils. However, the application of impregnation materials prevents the exposure of the stator windings to the ambient air environment directly, thereby preventing the aging due to oxidation of the coating of the enameled wires.

In [102, p.3] and [103, p.60], various degradation mechanisms of polymers are reviewed. In [102], the degradation mechanisms of the thermal degradation are compared both in the absence of oxygen and in the presence of oxygen. According to [102], a pyrolysis reaction is the essential degradation reason for polymers placed in a total vacuum or a completely inert and dry atmosphere. Polymer pyrolysis contains three general mechanisms, namely random chain scission, de-polymerization and side group elimination. In comparison, thermal oxidation is the main degradation mechanism for polymer degradation in the presence of oxygen and application of heat, which is the test atmosphere defined by the standards [21, 26, 101].

Therefore, the Thermal Index and Arrhenius equations of EI and EIS concluded from the standard test methods are not necessarily valid to describe the degradation of EI and EIS of electrical machines in electrified vehicles, when the windings are exposed to no or a low content of air due to impregnation.

The tests below are carried out on enameled wires to investigate the thermal degradation differences when the wires are aged in air atmosphere and when they are aged in the absence of oxygen atmosphere, respectively. The study will also suggest the necessity of introducing a new thermal aging test procedure for enameled wires if they are used in absence of air condition. The tests on enameled wires are performed together with Chemistry and Chemical Engineering department, Chalmers University of Technology.

6.1.1 Test sample

The test object DAMID 200 enameled wire has two layers of coating, which are polyesterimide as a base coat and polyamide-imide as a top coat [52]. This enameled wire is chosen as a sample of interest due to the wide usage of its coating materials. The wire is of 0.9 mm diameter including approximately 0.85 mm diameter of copper.

6.1.2 Thermal stress and Scanning Electron Microscopy (SEM)

Fig. 6.1 shows the schematic setup for thermal aging of enameled wires. As shown in Fig. 6.1, a tubular furnace (Lenton, LTF14/25/180) is used for the convenience of gas environment and flow control. One side of the furnace is connected to a source of gas; a tank filled with Ar or synthetic air (20% O2 + 80% N2), and the other side is connected to an exhaust gas collector bubbled through water at room temperature. For both tests with different gas environments, the gas flow rate is controlled to approximately 20 ml/min. In addition, for both tests the same temperature stress profile is created with a Eurotherm 2416 temperature controller: 1) the furnace is slowly heated at the rate of 2°C/min to 275°C, 2) 275°C is maintained for 168h and 3) the furnace is cooled down to room temperature with a temperature change rate of 2°C/min.

For each test, the enameled wires are cut into pieces of length 40 to 50mm. 6 pieces of enameled wires are placed in an alumina boat crucible and then placed in the middle of the tube furnace as Fig. 6.1. After the thermal stress treatment, the specimens are prepared for further Scanning Electron Microscopy (SEM) observations. The SEM is a type of electron microscope that produces images of a sample by scanning it with a focused beam of electrons [104]. The electrons interact with atoms in the sample, producing various signals that contain information about the sample's surface topography and composition [104]. In our tests, the SEM measurements are carried out by the Phenom ProX desktop scanning electron microscope, which utilizes the beam from a thermionic emission gun. For the imaging mode, a 10-15 KeV beam is selected and both Secondary Electrons (SE) and Backscattered Electrons (BSE) detectors are applied.
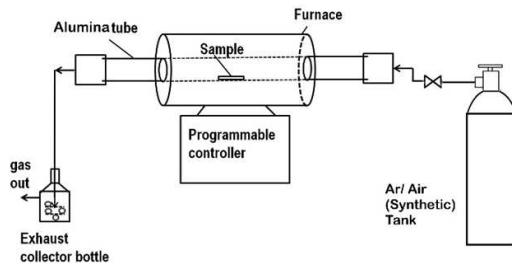

Fig. 6.1 Schematic setup of thermal aging of coated sample

6.1.3 Thermal Gravimetric Analysis (TGA)

Thermal Gravimetric Analysis (TGA) is a method of thermal analysis in which changes in the physical and chemical properties of materials are measured as a function of increasing temperature (with a constant heating rate), or as a function of time (with a constant temperature and/or constant mass loss) [105]. TGA is commonly used to determine selected characteristics of materials that exhibit either mass loss or gain due to decomposition, oxidation, or loss of volatiles (such as moisture) [105].

In our tests, the TGA are carried out on small pieces of new DAMID 200 enameled wires under Synthetic air (20% O_2 + 80% N_2) and Ar atmospheres, respectively. Each test sample is cut into length of approximately 3 mm. In order to subtract the contribution from the Cu oxidation, TGA is undertaken on the same length of Cu wire without enamel from the same wire supplier. The mass losses due to thermal stress within two different gas environments are observed and compared thoroughly.

The TGA experiments are performed with a NETZSCH STA 409 PC instrument as shown in Fig. 6.2. To ensure high accuracy for each experiment, a calibration is performed before each test by subtracting the weight contribution from the instrument, if any.
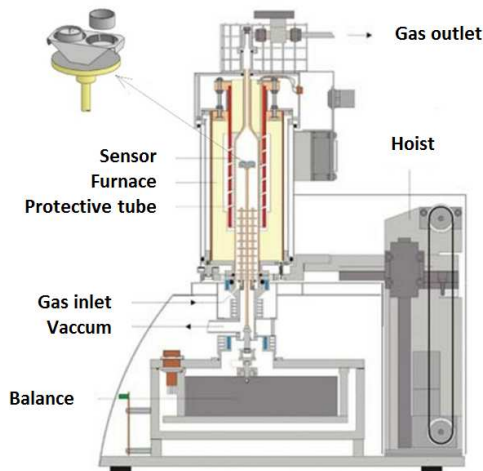

Fig. 6.2 Schematic setup for TGA measurement

6.2 Motorette testing

In order to verify our hypothesis about the causes of EIS degradation under dynamic temperatures and to study the symptoms during degradation thereby improving the condition monitoring methods, accelerated degradation tests are carried out on segmented stators, i.e. motorette specimens. The motorette specimen is defined in the subsequent section. The original plan was to test up to 8 motorette specimens at once for each accelerated testing, so that the results could reflect the statistical distribution. However, we start with testing a minimum of two motorette specimens for each accelerated testing in order to learn the physics of EIS degradation with cycled temperatures.

6.2.1 Test sample - segmented stator

The Volvo in-house designed traction machine (referred to as the VCE machine in this document) is chosen as the study object. Four of the traction machines are used as in-wheel propulsion for one wheel loader as shown in Fig. 6.3. The reason for choosing this electrical machine as the further study object is that it is a known design (geometries, materials, etc.) and that it is a relevant application. Fig. 6.4 shows the stators in production in the Eldrivet project [106]. More information about the wheel loader driving cycles and VCE machine is included in Chapter 5.3.

Fig. 6.3 Wheel loader with in-wheel drive traction electrical machines

For cost reasons, a minimized test object is designed. The test specimen before impregnation with epoxy is shown in Fig. 6.5. It is part of the VCE machine that has a concentrated winding in the stator (Fig. 6.4). The winding structure of the specimen consists of 7 turns and 29 parallel strands, which are rather arbitrarily

Fig. 6.4 Illustration of the VCE electrical machine stators

placed into the slot of the reference machine and are wound around the tooth of the segmented stator. In addition, two water cooling channels are made in the iron tooth of each specimen to simulate the cooling in the reference machine. The single tooth test object is later on impregnated with epoxy by Vacuum and Pressure Impregnation (VPI). The test specimen is hereafter referred to as the 'motorette'. Fig. 6.9 shows the cross section of the motorette with epoxy impregnation.
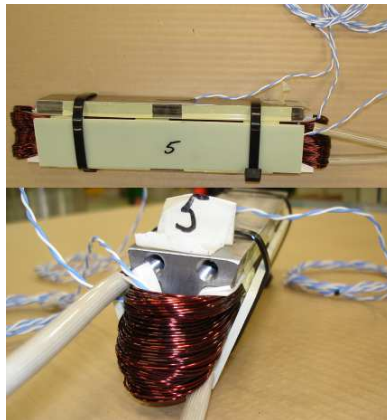

Fig. 6.5 Stator segment motorette sample before epoxy impregnation

The figure at the left of Fig.6.6 shows one of the first designed motorettes which suffered from water leakage after some thermal cycle stressing. In the first design, the cooling channels of a motorette are drilled in the back of the stator

tooth. There are several possible reasons for the water leakage, which are listed below to avoid similar failures in other relevant studies.

1. Mismatches between the connector (illustration at the left of Fig.6.6) and the internal thread in the iron back. The thread in the iron back was not easy to drill due to insufficient material thickness at iron back;

2. Missing O-rings and other sealing between the connector and the iron back thread;

3. Thermal mechanical stress loosened the connections.
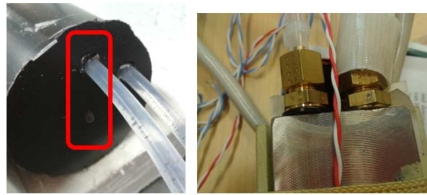
Fig. 6.6 Initial design of the test sample with water leakage (left) and the connectors for cooling channels (right)

In order to avoid water leakage, the design of the cooling ducts was improved (Fig. 6.7) by modifying the following design areas:

1. Cutting the cooling ducts at the top of the iron back;

2. Silver welding of the cooling metal tube to the cut groove to ensure good heat transfer;

3. Moving the problematic connectors outside the impregnated motorette.

Another improvement of the second generation of motorettes is the strand distribution inside a slot as shown in Fig. 6.8. In comparison to the 1st group of motorettes (left side of Fig. 6.8), the improvements to the distribution of the windings in the slots of the 2nd group of motorettes (right side of Fig. 6.8) are made as follows:

1. The wires are concentrated into the slot by fixing the tightening plate more firmly to the stator core (bottom illustration in Fig. 6.7);
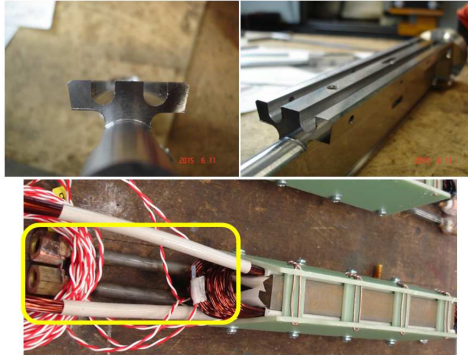
Fig. 6.7 Second design of the test sample with cut grooves (top) and the finalized motor-rette before impregnation with silver welded metal tubes acting as cooling ducts (marked in the yellow box) (bottom)

2. A slot wedge is added at the slot opening as it is used in the stator of the real machine;

3. Piecies of insulation paper between the tightening plate and windings are added to represent the insulation paper pieces between two winding phases inside a slot of the VCE machine stator.

Fig. 6.8 Cross section of the 1st group (left side) and 2nd group (right side) of the designed and produced test motorettes

The lesson that is learned from the specimen design and production is to keep the designed specimen as simple as possible to only include the materials/parts

of interest (stator, windings and other insulation materials, etc.) and leave the rest outside the test specimen (cooling system and so on) to avoid unexpected failures. Also, good communication between the designer and the manufacturer and between different departments within the manufacturing company is extremely important.

6.2.2 Temperature sensor locations and thermal stresses

Five PT100 temperature sensors are placed inside each motorette specimen. Four of them, as shown in Fig. 6.9, are present to capture the temperature distribution at different locations and they are in the middle of the axial direction. The 'winding 2' sensor is located in the end winding and cannot be shown in this illustration. The hot spot is identified by means of both simulation and testing, and its temperature is controlled by controlling a DC current power supply and a cooling water pump.
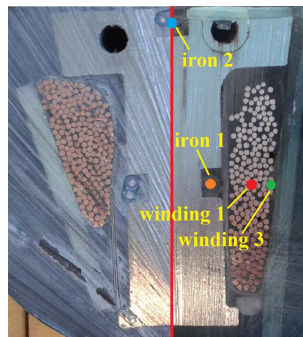
Fig. 6.9 Cross-section showing temperature sensor positions

6.2.3 Test rig

The test rig for accelerated tests with motorettes is built in-house as shown in Fig. 6.10 and Fig. 6.11. The rig is designed with a capacity to test a maximum of 8 samples simultaneously, taking into account the statistical nature of the lifetime test. Each motorette is placed inside a thermally insulated box. The cycled temperature is created by controlling the electrical current and forced water cooling,

which represents the heat generation and dissipation, respectively, in a real machine. The rig could be expanded for an accelerated lifetime test with E-field related stress, including voltage amplitude and frequency variations. Between a certain number of thermal cycles, SoH/condition monitoring measurements are made for each specimen to keep track of the health status. Table. 6.1 lists the hardware and software used for the Volvo in-house built test rig. The control schematics are shown in Appendix A.
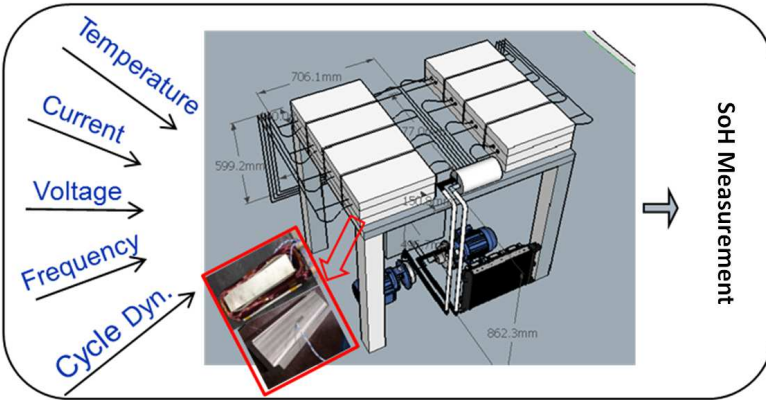
Fig. 6.10 Test rig sketch for accelerated tests
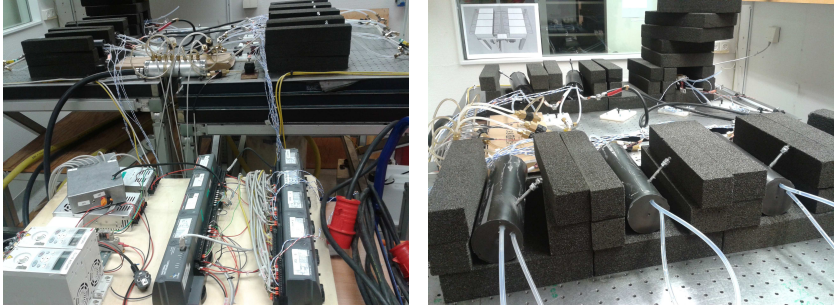
(a) Test rig built for accelerated tests - view 1 (including control hardware)

(b) Test rig built for accelerated tests - view 2 (excluding control hardware)

Figure 6.11: Test rig built for accelerated tests

Table 6.1: Components list of the test rig for accelerated tests on motorettes

Name	Function
PSI 9000 3U, Electro-Automatik	high current DC power supply for motorette heating
Peripheral pump P, Sawa	pump used for motorette cooling
ACS 150 drives, ABB	speed controller for pump electric motor
Flow divider, in house design and produced	to divide the cooling flow between 8 motorettes
Flow valves, Parker	to adjust the flow rate through each motorette
Swissflow 800	flow meter to measure flow rate for each motorette
Thermocouples	to measure inlet and outlet temperatures for each motorette and water tank
Field Point (FP), National Instrument (NI)	data logging and data conversion
Labview, National Instrument (NI)	control software

6.3 Electrical machine testing

During the above-mentioned accelerated degradation tests, the condition monitoring measurements are carried out on motorettes and detailed set-ups are described in Chapter 6.4.1. One of the important findings is that the insulation capacitance shows a clear trend during the degradation. Therefore, a study of an on-board monitoring method to utilize the capacitance changes as an indication of traction machine degradation is carried out via a master thesis project within the doctorate project. The details are documented in a master thesis [107]. Two PMSM machines of different sizes are tested with the purpose of verifying the on-board off-line method, and the two machines are briefly described in the following sections.

6.3.1 Test object 1

The main test object for this on-board off-line measurement method is the RWD electrical machine described in Table 2.6 and Chapter 5.2.3. More information about the LTH in-house designed machine can be found in Chapter 2, Chapter 3 and Appendix A in [108]. A picture of the machine is shown in Fig.6.12.

Fig. 6.12 RWD machine/EM1 [75]

6.3.2   Test object 2

In order to study the applicability of the prognostic method to a larger electrical machine for traction, the on-board off-line measurement method is also tested on a machine which is designed for electric hybrid heavy vehicles. The studied machine is an oil cooled, 6-pole, 80/180 kW (continuous/peak power) PMSM with distributed windings and a V-shaped magnet arrangement utilizing reluctance torque [109]. The base speed of the electric traction machine is 6,000 rpm and the maximum speed is 15,000 rpm. More information about this in-house designed machine can be found in [109]. This machine is also used for a sensitivity study for the temperature dependency of the measurement method. For the convenience of discussion, this machine is named **EM3**. A picture of the machine inside a temperature chamber is shown in Fig.6.13.

Fig. 6.13 EM3 placed inside a temperature insulated chamber [107]

6.4   Measurements for State of Health (SoH) and failure

The definitions of 'on/off-line' and 'on/off-board' condition monitoring methods are given in Chapter 2.5. In our studies, both 'Off-board off-line' and 'on-board off-line' measurements are investigated. The test set-ups are described below and the results are presented in Chapter 7.

6.4.1   Off-board off-line

To understand the degradation mechanisms during the accelerated degradation testing, off-board off-line tests are applied on the motorettes.

The DC polarization current and AC impedance measurement approaches are performed between the windings and the iron core and between the randomly grouped parallel strands of the machine windings. The above-mentioned measurements can furthermore be used to perform and analyze a short series of measurements: 1) initial measurement, 2) thermally loading and 3) repeated measurement at initial conditions [47]. The detailed set-up and measurements results are presented in this Chapter and in Chapter 7, respectively. The measurements between windings are performed by dividing the parallel strands of 29 wires into two groups of 14 and 15 strands randomly and it provides a great advantage that the winding insulation state of health and degradation can be estimated between these two groups and along the whole length of the windings.

Fig. 6.14 shows the original plan of the test setup with the functions of 1) heating up the sample under test to a predetermined temperature while SW1 relays are on; 2) applying a DC voltage pulse and measuring the polarization current at temperatures of interest for 300 seconds while the SW2 relay is on. The high current power supply is a PSI 9000 3U from Elektro Automatik and the DC voltage is supplied by a Glassman FJ2P60, with the polarization or leakage current measured by a Keithley 6485 picoammeter. However, the leakage current of the relay when it is off is in a similar range to the leakage current to be measured of the test objects. Therefore, the automatic switch between current supply and voltage supply is not used. Manual disconnection and connection have to apply for these measurements.

The capacitance between the two grouped strands and between the winding and ground is measured by Gamry Reference 3000 potentiostats. One open end of each of the two strands is connected to the Gamry potentiostats and the other open end is attached to a 50 KΩ resistance due to the measurement range limitation of the Gamry equipment.

The inductance and resistance of winding conductors are also measured by Gamry Reference 3000 potentiostats with the whole winding (not split as previous case) connected in series with Gamry.
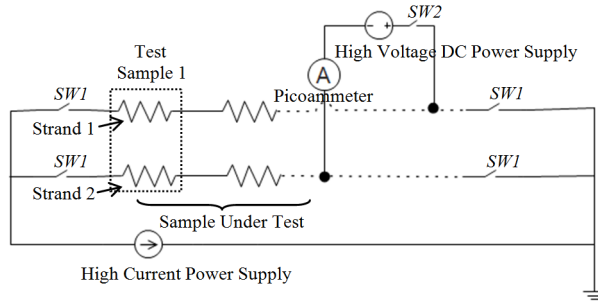
Fig. 6.14 Circuit diagram for heating up and measuring the polarization current of a single tooth sample [47]

6.4.2   On-board off-line

This section explains the implementations of the on-board off-line measurement method carried out on the entire machines (see Chapter 6.3) and mainly quotes the master thesis [107].

First a short voltage step is applied across the phases of the electrical machine in the vehicle. This voltage step can be as short as 10 μs. The voltage step is generated by the power converter going from the lower short circuit switching state (0,0,0) to switching state (1,0,0) (or an equivalent switching state). This corresponds to applying the DC-link voltage across the phases as depicted in Fig. 6.15. The transient current response that occurs as a result of this voltage step is then measured [107]. By means of data post-processing of the logged current and then by comparing the high frequency current response at different usage times, the current signatures are shifted at different ages of the machines, this being caused by changes in the parasitic capacitance during degradation. The block diagram in Fig. 6.16 shows the simplified connection for the test set-up. Table 6.2 describes the functions of the various components needed for this type of measurement. The measurement results are presented in Chapter 7.
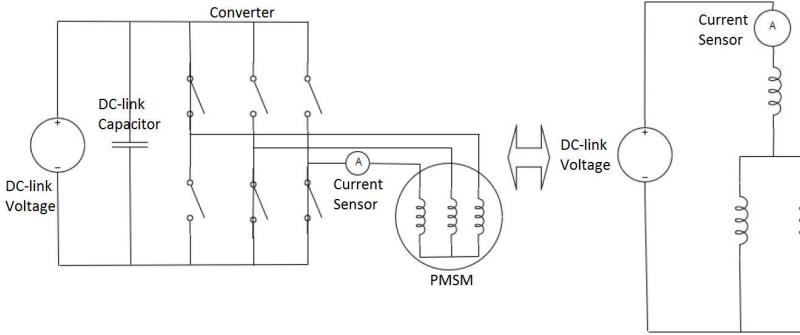
Fig. 6.15 Equivalent circuit of electrical machine when a voltage pulse is generated by drives
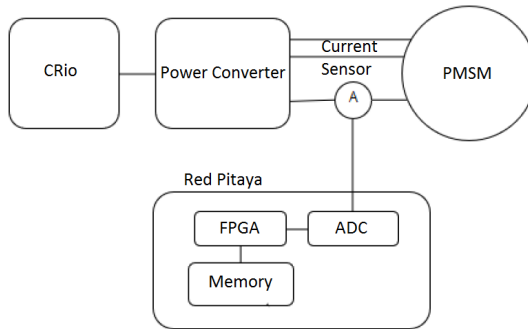
Fig. 6.16 Block diagram of the off-line on-board test set-up

Table 6.2: List of components for on-board off-line condition monitoring

Name	Function
cRIO, NI	machine control
Power converter	machine drive
PMSM	tested object
Tektronix A6303 and AM 503	current sensing and amplifying
Red Pitaya	A/D converter and data logging for high frequency current

Chapter 7

Experiment and simulation results

The results obtained from the tests and simulations are presented in this chapter. The purpose is to evaluate the tests proposed in Chapter 6, identify the relations between load, time and degradation of electrical insulation systems (EIS) and connect the experimental results with theoretical analysis.

This chapter starts with the test results of the enameled wires. The test results demonstrate the thermal aging difference of the coatings of wires in the environment with and without air, respectively. The thermal aging difference observed from the tests, indicates that the thermal aging mechanisms of the coating could be different with and without complete encapsulation (see Chapter 2.2.2). Afterward, the test results from the motorette testings are presented. Both the measured data before (i.e. the initial state) and during thermal cycle aging are presented and compared to the previous defined simulations. Next, results obtained from system simulations (Fig. 5.1) are presented on both VCE machine and RWD machine (defined in Chapter 5). In the end, results from the on-board off-line condition monitoring is briefly discussed and the results are mainly referred to the master thesis presented in [107].

7.1   Results of enamel wire testing

The setups for the tests performed on enameled wires are described in Chapter 6.1. The results from the SEM and TGA measurements are presented below.

7.1.1   Tube furnace aging and SEM results

The first visual inspection shows significant difference between the samples treated in the two different gas conditions with 275°C of 168 hours. As shown in Fig. 7.1, the coating of all the air treated samples show delamination at the end of the test. Whereas, the coating of all the Ar treated samples becomes darker than the same enameled wires when they are brand new, but without delamination. As a result of the delamination, the mass loss of the air treated sample is much higher than the Ar treated sample.

Fig. 7.1 Picture of the enameled wires after thermal stress of 275°C for 168 hours seated in the alumina boat crucible

In order to further investigate the surface changes of the enameled wires after the thermal treatment with the exposure to different gases, SEM measurement is applied.

Fig. 7.2 compares the thermally aged enameled wire surface in a low magnification, where the bright part is Cu and the dark part is polymer coating. Despite of the bottom part of Fig. 7.2 (b), which is due to the cut edge when preparing the sample rather than aging, the comparison clearly show that the damage of the same coating in air is much sever than it in Ar. Furthermore it indicates that the thermal degradation rate of the coating is much faster in Air than in inert gas.

The air aged and Ar aged samples are observed with high magnifications of 5k times and 17-20k times and presented in Fig. 7.3 and Fig. 7.4, respectively. Due to the combustion/oxidation of the polymer coating in air, the Cu wire is exposed and discontinued as in Fig. 7.3 (c) and Fig. 7.4 (e). In comparison, the Ar aged sample shows that the coating surface is continued as in Fig. 7.3 (d) and Fig. 7.4 (f). However, with the highest magnification in Fig. 7.4 (f), the Ar treated sample

shows small 'particles' or 'bubbles' at the left part of the picture. This might be the early phase of coating delamination. This early phase of delamination could result in sudden changes of dielectric properties, such as the insulation resistance and capacitance, before the final failure of delamination.
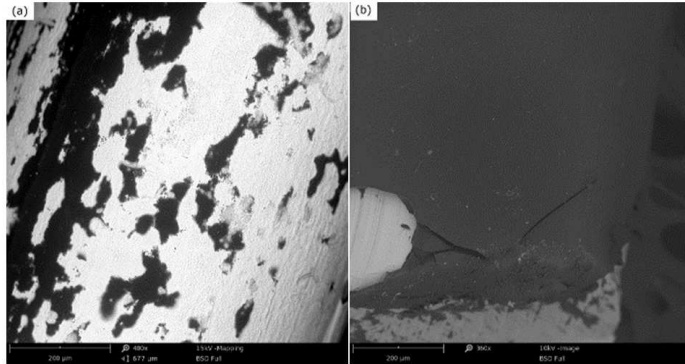

Fig. 7.2 SEM images of enameled wires after thermal stress under gas stream of air (a) and argon (b)
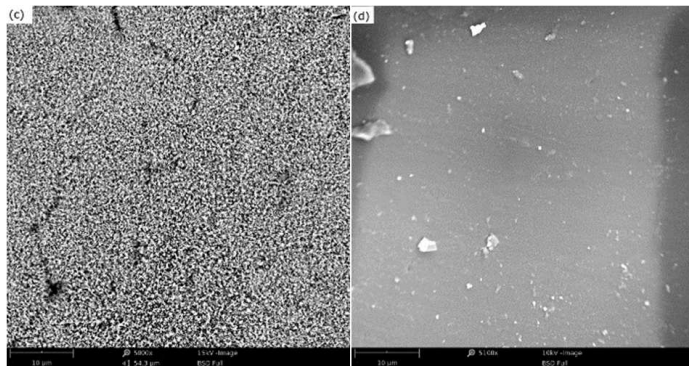

Fig. 7.3 SEM images (5K times) of enameled wires after thermal stress under gas stream of air (c) and argon (d)
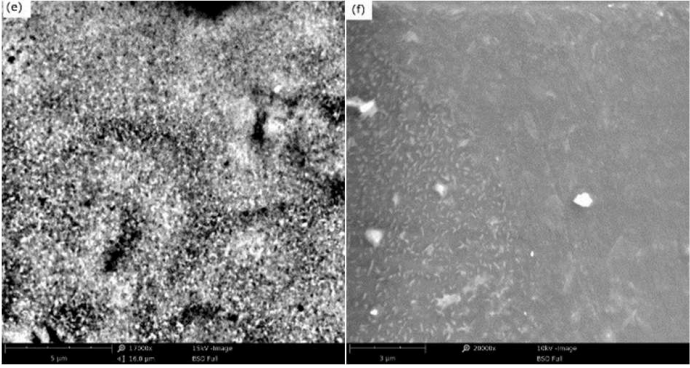
Fig. 7.4 SEM images (17-20K times) of enameled wires after thermal stress under gas stream of air (e) and argon (f)

7.1.2 TGA test

TGA tests (see Chapter 6.1.3) are carried out on enameled wire (coating + copper) and pure copper samples. Each type of specimens is tested in Ar or Air, separately. The mass losses of enameled wire sample (curve 1 and 4) and pure copper sample (curve 2 and 3) are shown in Fig. 7.5. The y-axis shows the residual mass change [%] compared to the initial mass and the temperature change [°C] (the dotted-line), and the x-axis shows the TGA measurement time (minute) including 2 hours isothermal stage at 400°C. In comparison to curve 1 which represents the mass loss of enameled wire in Ar, curve 4 shows higher mass loss when enameled wire is in synthetic air. However, the mass loss of pure copper occupies a large proportion in the total mass loss of enameled wires, from the exposure to heat and different gases (curve 2 and 3).

Fig. 7.6 compares the effective mass change [%] of the coating material in air and inert gas. The effective mass change is calculated by subtracting the percentage mass loss of the pure Cu from that of the enameled wire. The figures at the left and right side of Fig. 7.6 are the effective mass change of coating before and after the 2 hours of isothermal stage, respectively. A higher coating mass loss is observed from the exposure to air than to Ar. The values obtained from the tests in air and Ar corresponds to 0.27% and 0.18% before the isothermal stage, and 0.18% and 1.65% after the isothermal stage, respectively, with the measurement accuracy ± 0.0003%. Fig. 7.6 also shows that the effective mass loss of coating increases steadily first and decreases sharply at around 380°C in Ar environment.
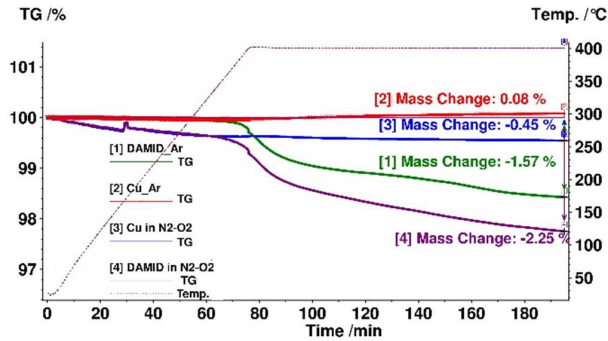
Fig. 7.5 Comparison of TGA results under inert (Ar) and Air (20% O2+80% N2) atmo-
sphere of enameled wire and pure Cu wire. Percentage of mass change is indicated
for each sample. The bump under Air (on sample 3, 4 around 30 min) is artifact
from external noise

In comparison, the sharp decrease starts at a bit lower temperature around $310°C$
in synthetic air. The coating material becomes unstable at lower temperature in
the presence of oxygen than absence of oxygen.

In other words, if the high temperature oxidation is considered as the only
degradation cause of polymer coating, the complete impregnation of windings
should prevent the enameled wire coating from oxidation, thereby prolonging
its lifetime. However, from the accelerated degradation tests of motorettes with
complete impregnation, it shows that the lifetime of windings of motorettes is
shorter than the lifetime estimated by Arrhenius equation (results are presented
in table 7.5). The Arrhenius equations are obtained with standard tests and the
enameled wires are tested with constant high temperatures in the presence of air.
Whereas, the accelerated aging tests of motorettes are carried out with cycled tem-
perature and the wires and the wires are not directly exposed to air due to the com-
plete impregnation. This emphasizes the motivation to look for other degradation
mechanisms when the wire coatings in EIS is exposed to cycled temperatures.

7.2 Results of motorette testing - initial state

Two different motorette designs are discussed in Chapter 6.2.1, which show dif-
ferent winding distributions (see Fig. 6.8) and requires different ways (Fig. 6.7) of
producing the cooling channels. The studies on the insulation resistance (IR) at the

(a) Effective mass loss [%] before 2 hours of isothermal stage

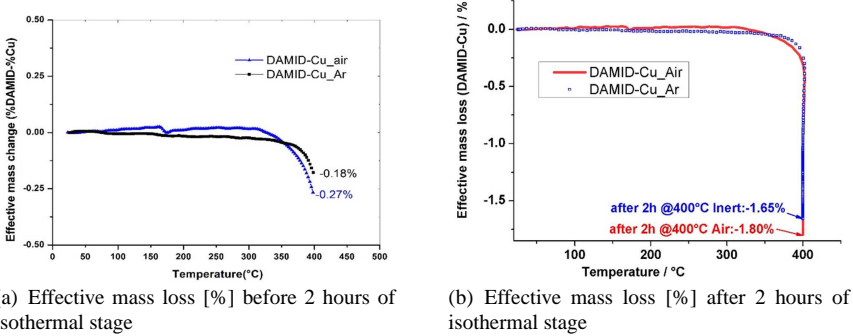(b) Effective mass loss [%] after 2 hours of isothermal stage

Figure 7.6: Comparison of effective mass loss [%] in inert (Ar) and Air (20% O2+80% N2) atmosphere of enameled wire and pure Cu wire

initial state, i.e. before the exposure to the accelerated aging tests, of the motorette specimens are carried out on one of the 1st group of specimens before impregnation with epoxy. The studies of the insulation capacitance (IC) at the initial state of the motorette specimens are carried out on eight samples of the 1st group of specimens with complete impregnation with epoxy. The purpose of the these two studies is to gain a deeper understanding of the condition monitoring methods (see Chapter 6.4.1), namely the DC leakage current and the AC impedance measurement. After exposing the 1st group of specimens to the long term accelerated aging testing, the water leakages are found, and therefore the 2nd group of specimens are produced with the re-design. However, the well-understood condition monitoring methods are still valid. Hence, the verified methods are continued to be implemented on the 2nd group of specimens in the accelerated aging testings in the later studies.

In short, the test results presented in Chapter 7.2 are obtained from the tests with 1st group of specimens with and without epoxy impregnation. The results presented in Chapter 7.3 are obtained from accelerated aging testings with 2nd group of specimens with epoxy impregnation. A list of all motorette specimens used in the studies are summarized in Appendix B.1.

In the following discussions, two terms, 'winding-to-winding' and 'winding-to-ground', are often used. The IR and IC of 'winding-to-winding' or 'between windings' are measured between the two randomly grouped strands (defined in Chapter. 6.4.1). The data of 'winding-to-ground' or 'between the windings and

ground' are obtained from the measurements between all strands inside the slot and the ground. The simplified illustrations of these measurements are shown in Fig. 3.2. Besides, the inductance in the following discussions is the value measured on all strands inside the slot.

7.2.1 Transient and steady state of the polarization current

Transient polarization current

The DC polarization currents and the resulted dielectric resistances between windings are studied in detail below. Fig. 7.7 [47] shows the dielectric resistance, which is derived from the polarization current. They are measured at four different temperatures and each of the current is measured for 2 minutes at 900 V. The temperatures are measured with the PT100 sensor in the middle of the active winding (sensor 1 in Fig. 6.9).

The measurements show that the leakage current increases though the dielectric resistance decreases with the increased temperature. Besides, the insulation resistance decreases with time at one constant temperature.

Theoretically, when the step voltage is applied over the dielectric material, the positive and negative charges become oriented thus forming different dipoles [110]. The dielectric polarization is the result of a relative shift of positive and negative charges in a material [110]. During these processes, the electric field is not able to force the charges to escape from the material, which would cause inherent electric conduction [110]. In [47, 110, 111], the equation of the transient leakage current after applying a step voltage (Equation 7.1) and the equation of insulation resistance at steady state (Equation 7.2) are derived. The first and second part of Equation 7.1 represent the conductivity and the activation of the different polarization processes of the sample, respectively [112]. The last part with the delta function cannot be recorded in practice due to the large dynamic range of the current and can be neglected [110].

$$i_p(t) = (\frac{\sigma}{\varepsilon_0} + f(t) + \varepsilon_r \delta(t)) C_0 U_c \qquad (7.1)$$

where σ is the conductivity, ε_0 permittivity of vacuum (8.85419[-12]), $f(t)$ the dielectric response function, ε_r the relative permittivity, $\delta(t)$ the delta function arising from the suddenly applied step voltage at $t = 0$ and C_0 the geometric or vacuum capacitance of the tested sample, separately [47].

$$\frac{U_c}{i_p(t_{ss})} = C_{gm}e^{-\lambda\theta} \tag{7.2}$$

where C_{gm} and λ are the global dielectric resistance coefficients, θ the temperature, $i_p(t_{ss})$ the polarization/leakage current at steady state, separately.
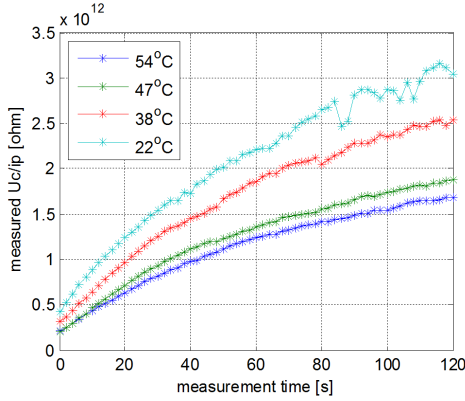

Fig. 7.7 Transient dielectric resistances measured at different temperatures

Steady state polarization current

Table 7.1 shows the dielectric resistances obtained at 2 minutes at the four different temperatures. After the curve-fitting of the measured values (Table 7.1), the coefficients of Equation 7.2 are obtained. It describes the relationship between the dielectric resistances and temperatures of the tested object. Fig. 7.8 compares the measured points and the fitted curve.

Table 7.1: Steady state dielectric resistance at different temperatures

Temperature [°C]	22	38	47	54
$U_c/i_p(t_{ss})$ [TΩ]	1.68	1.88	2.54	3.15

$$\frac{U_c}{i_p(t_{ss})} = C_{gm}e^{-\lambda\theta} = 4.9^{12}e^{-0.02\theta} \tag{7.3}$$

Apart from the numerical expressions presented above, we learned that the leakage current and insulation resistance are temperature and time dependent.
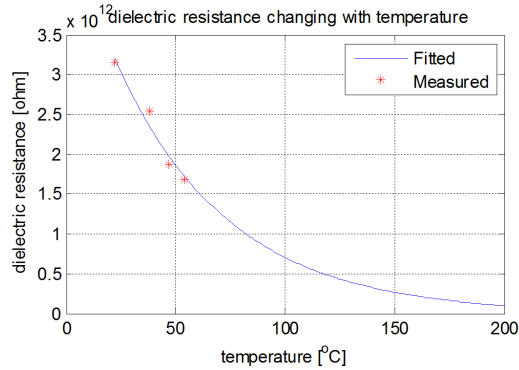
Fig. 7.8 Dielectric resistance changing with temperatures for both measured (red) and fitted (blue) values

Hence, in order to make fair comparisons to further indicate the degradations, IR measurements should be made at the same temperature and at the same time after the step voltage is applied. Taking these factors into account, for the IR measurements in the later studies (Chapter. 7.3), the high voltage DC power supply and the Picoammeter (test setup in Chapter 6.4.1) are well synchronized by Labview control. All the IR measurements are carried out at room temperature. The DC voltage level are all set to 1300 V and lasts for 5 minutes to reach the steady state of the leakage current. If tests are repeated on one sample, enough 'rest' time between every two tests is needed. It is at least equal to the time that the high voltage was applied in the previous IR test. This is to ensure that all charged dipoles from the previous IR measurement are fully discharged.

7.2.2 Insulation capacitance

The insulation capacitance (IC) is less temperature dependent compared to the insulation resistance (IR). The presented values in this part are measured at two locations, which are between windings and between winding and ground. The IC measurement are carried out at room temperature on the 1st group of specimens with complete epoxy impregnation at the initial state.

An example of the measured phase and angle (blue dotted-line) of a motorette impedance is shown in Fig. 7.9. It is measured between 0.001 Hz and 10 MHz AC frequency. The measured data is fitted to a parallel resistance-capacitance

electrical circuit to derive the insulation capacitance value. Good fit between the measurement curve (blue dotted-line) and the fitted curve (green solid-line) is observed as shown in Fig. 7.9.
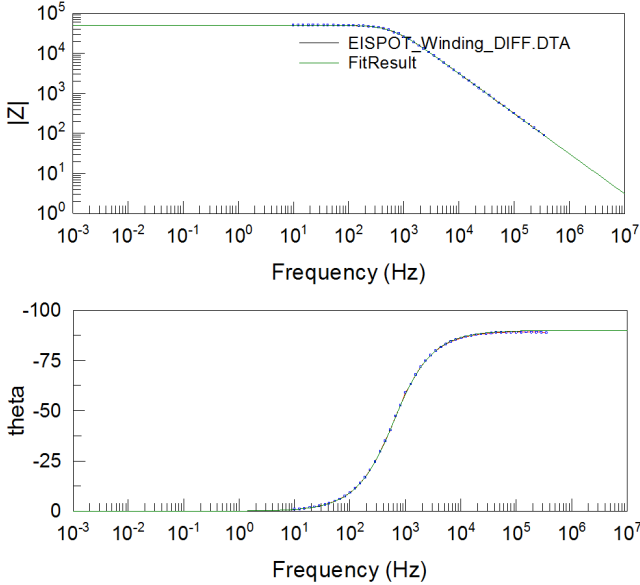
Fig. 7.9 An example of a measured (blue dotted-line) and a fitted (green solid-line) phase and angle of the impedance of a single tooth sample at room temperature

Fig. 7.10 and 7.11 show the measured IC of 8 different motorette samples between windings and between winding and ground, respectively. The values are in the range of 14.5 nF - 16.5 nF and 0.41 nF - 0.44 nF, between the windings and between the windings and ground, respectively.

Fig. 7.10 Initial insulation capacitance between two randomly grouped paralleled windings

Fig. 7.11 Initial insulation capacitance between the windings and ground

7.3 Results of Motorette testing - degradation and failure

7.3.1 Thermal cycles of accelerated degradation tests

A deeper understanding of the condition monitoring methods, in terms of insulation resistance (IR) and insulation capacitance (IC), is obtained by studying the measurements of the unused motorette specimens. The verified condition monitoring 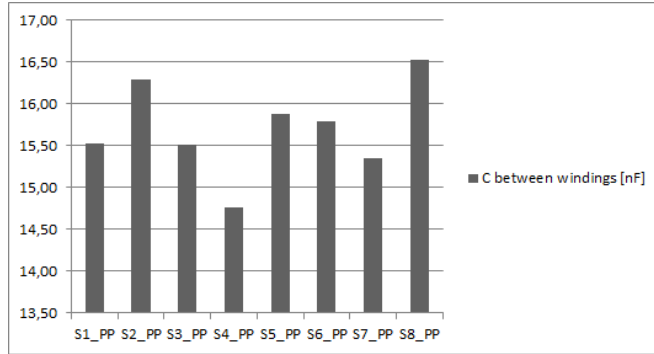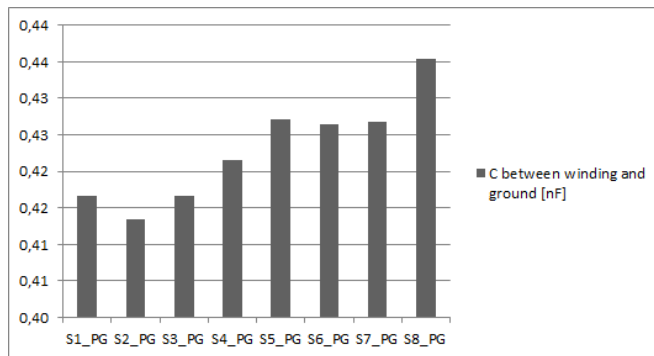methods are carried out periodically on the motorette samples during accelerated degradation testings when thermal cycles are applied. Table 7.2 shows the information of the three different temperature cycles applied for the accelerated tests. The cycled temperatures are measured at the hot spot of the segmented windings, i.e. via the sensor 'winding 1' in Fig. 6.9. The measured changes of IR and IC due to the long term cyclic temperatures are presented in the parts below.

Table 7.2: Tested thermal cycles

Cycle No.	θ_{min} [°C]	θ_{max} [°C]	τ_{dec} [s]
#1	210	230	150
#2	190	210	250
#3	180	200	250

7.3.2 Parameters changes during thermal cycle degradation

Thermal cycle #1

Six motorette specimens (called S1 to S6) are subjected to thermal cycle #1. Two motorette specimens (called S7 and S8) are used as references, which are not subjected to the cycled temperature.

The measured IC [nF] between winding and ground are presented in Fig. 7.12. The dark and the light gray bars represent the IC of specimens at initial state and after exposed to thermal cycle #1 for 47 hours, respectively. As a result, the changes [%] of IC of the 6 specimens are shown in Fig. 7.13. They are calculated by the division of the absolute IC change of each specimen in the accelerated test by the average value of IC of the two reference specimens.

Low insulation resistances (a couple of Ωs) between windings of the motorettes are observed after the exposure to thermal cycle #1 for 47 hours. Com-

pared to the IR of 260 GΩ - 350 GΩ at the initial state (Fig. 7.14), the small IR indicates short circuits between windings hence failures of the motorettes. Also, the decrease of inductance in the range of 3% - 43% (Fig. 7.15) is observed after the accelerated test, which is considered as another indication for failure. The IC between the windings and ground is decreased from 0.40 nF - 0.45 nF (unused motorettes) to 0.33 nF - 0.37 nF (failed motorettes) as shown in Fig. 7.12, which corresponds to the capacitance changes of approx. 12% - 18% (Fig. 7.13).
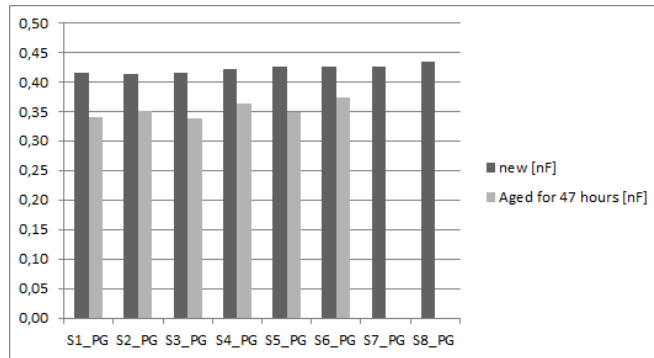
Fig. 7.12 Measured insulation capacitance [nF] **between winding and ground** for multiple motorette specimens before and after thermal cycle #1 applied for 47 hours
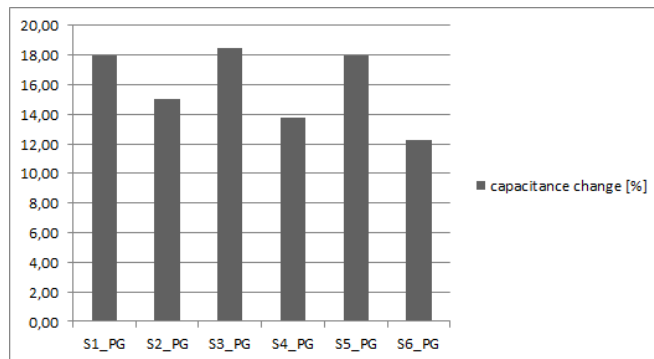
Fig. 7.13 Measured changes of insulation capacitance [%] **between winding and ground** for multiple motorette specimens before and after thermal cycle #1 applied for 47 hours

Fig. 7.14 Measured insulation resistance [GΩ] **between 2 randomly grouped strands** for multiple motorette specimens before thermal cycle #1 applied

Fig. 7.15 Measured changes of winding inductance [%] for multiple motorette specimens before and after thermal cycle #1 applied for 47 hours

(a) GΩ unit   (b) P.U. unit
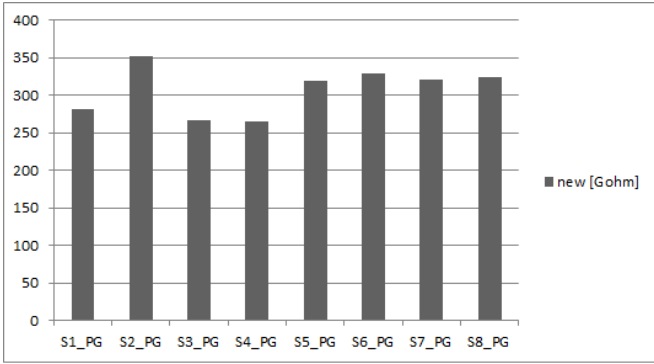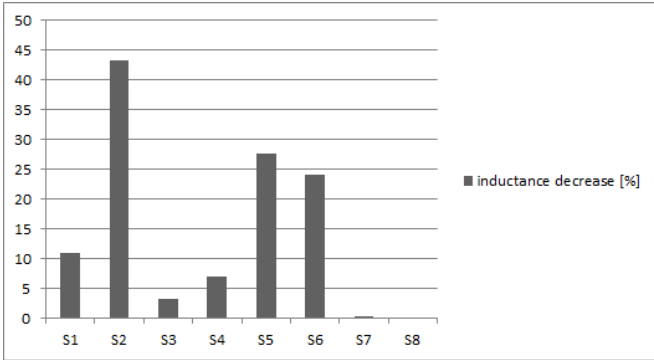
Figure 7.16: Measured insulation resistance **between 2 randomly grouped strands** for two motorette specimens during degradation with thermal cycle #2

Thermal cycle #2

Two motorette samples (called S1 and S2) are subjected to thermal cycle #2 in the accelerated aging testing.

The measured insulation resistance (IR) [GΩ] and insulation capacitance (IC) [nF] in relation to degradation time between windings are presented in Fig. 7.16(a) and 7.17(a), respectively. The change of IC [nF] between the winding and stator core/ground is shown in Fig. 7.18(a).

For the convenience of comparisons, the Per Unit (P.U.) values are derived and plotted in Fig. 7.16(b),7.17(b) and 7.18(b) for the above-mentioned parameters. The P.U. value of one sample is defined as the measured parameters (IR or IC or inductance) during the degradation testing divided by the same parameters at the initial state.

Low insulation resistances between windings are observed at approx. 190 hours of this degradation test as shown in Fig. 7.16(a), which indicates the failure of the motorettes.

From previous experiences, a steep change of IC is expected at the very early stage of degradation. Therefore, one more IC measurement is carried out at approx. 25 hours, which results in 6 measured points of IC but 5 measured points of IR of each specimen.
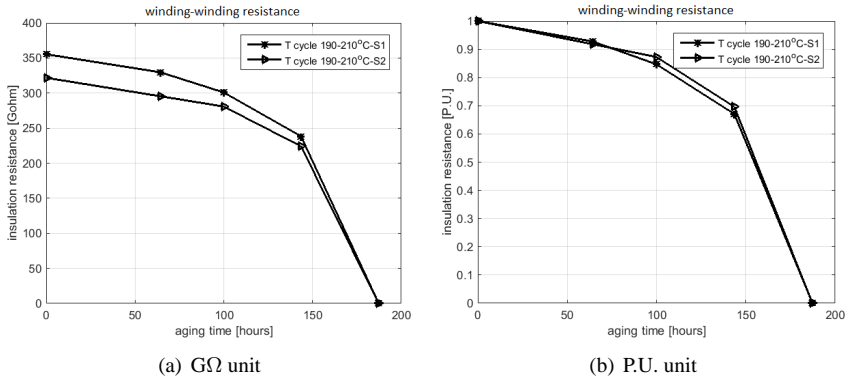
(a) nF unit

(b) P.U. unit

Figure 7.17: Measured insulation capacitance **between 2 randomly grouped strands** for two motorette specimens during degradation with thermal cycle #2

(a) nF unit

(b) P.U. unit

Figure 7.18: Measured insulation capacitance **between winding and ground** for two motorette specimens during degradation with thermal cycle #2

Thermal cycle #3

Two motorette samples (called S1m and S2m) are subjected to thermal cycle #3 in the accelerated aging test.

The measured insulation resistance (IR) [GΩ] and insulation capacitance (IC) [nF] in relation to degradation time between windings are presented in Fig. 7.19(a) and 7.20(a), respectively. The changes of IC [nF] between the windings and the stator core/ground are shown in Fig. 7.21(a). The Per Unit (P.U.) values are shown in Fig. 7.19(b), 7.20(b) and 7.21(b) for the above-mentioned parameters. The P.U. calculation is defined in the previous section.

Sudden increases of IR between the windings are observed at approx. 290 hours as shown in Fig. 7.19. Correspondingly, the IC between the windings show a slightly faster decreases than the previous trends as presented in Fig. 7.17. At the same time, sudden decreases of the winding inductance are observed as shown in Fig. 7.22. All these phenomenons indicate the failure of the two motorettes.

Two more condition monitoring points (i.e. IR, IC and inductance) are collected after the failure occurring. As shown in Fig. 7.19, 7.17 and 7.22, it seems that the failed motorettes are 'rebalanced' and the degradation is continued from the new 'starting point' at approx. 290 hours.

The measured IR is higher of the 1st group of specimen without epoxy impregnation (in the range of several $T\Omega$ as shown in Chapter. 7.2.1) than that of the 2nd group of specimens with epoxy impregnation (in the range of hundreds GΩ). The main reason is that air has higher electrical resistivity than the epoxy matrix (see Table. 3.1). However, it does not mean that air is a better electrical insulator than epoxy because the dielectric strength of air (3 MV/m [53]) is much lower than that of the epoxy (19-21 MV/m [49]). Another reason could be that the distance between the two randomly grouped strands of the 1st group of specimens could be larger than that of the 2nd group of specimens (see Fig. 6.5). As a result, the total equivalent IR of the latter specimen is lower due to the decreased insulation thickness.

(a) GΩ unit

(b) P.U. unit

Figure 7.19: Measured insulation resistance **between 2 randomly grouped strands** for two motorette specimens during degradation with thermal cycle #3
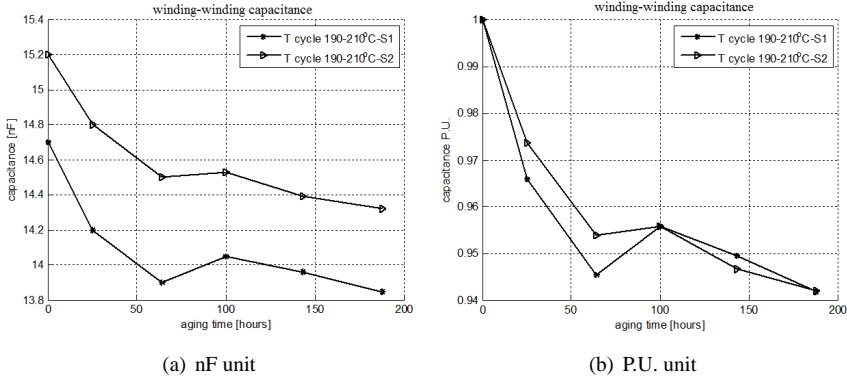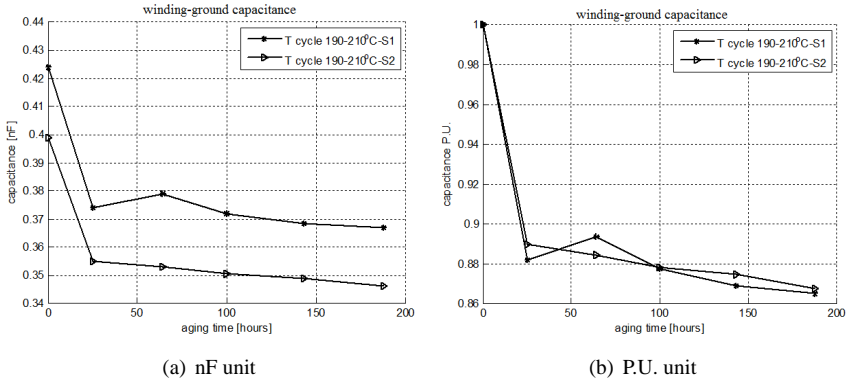

(a) nF unit

(b) P.U. unit

Figure 7.20: Measured insulation capacitance **between 2 randomly grouped strands** for two motorette specimens during degradation with thermal cycle #3
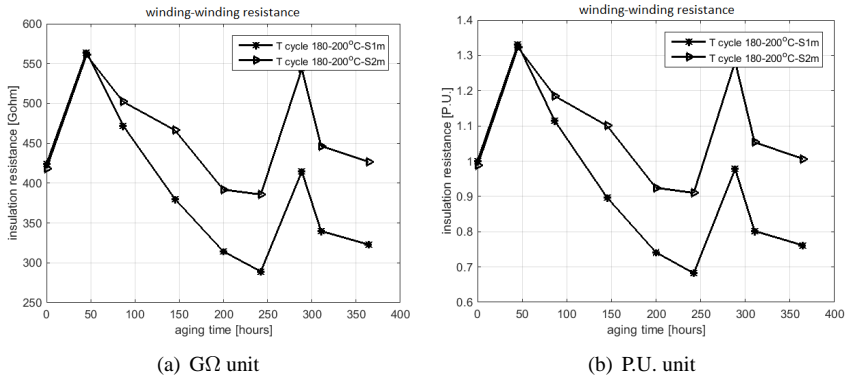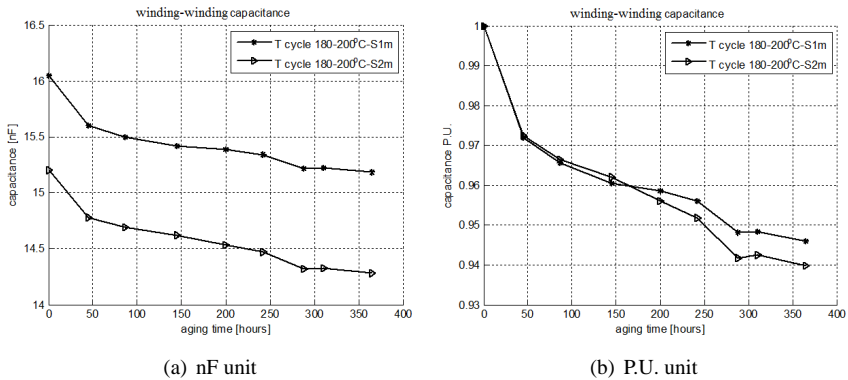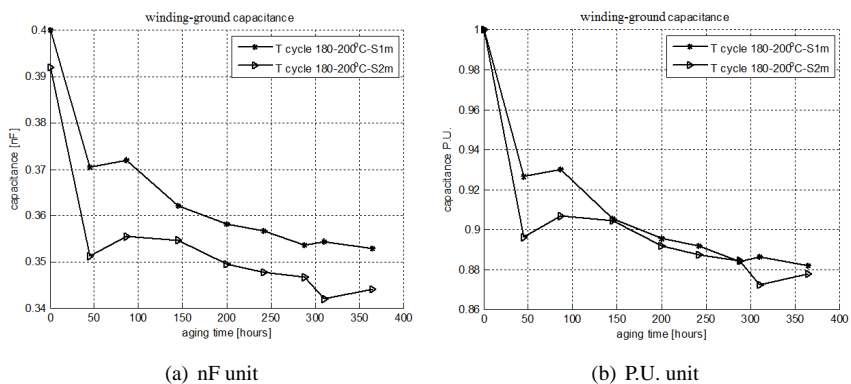
(a) nF unit   (b) P.U. unit

Figure 7.21: Measured insulation capacitance **between winding and ground** for two motorette specimens during degradation with thermal cycle #3
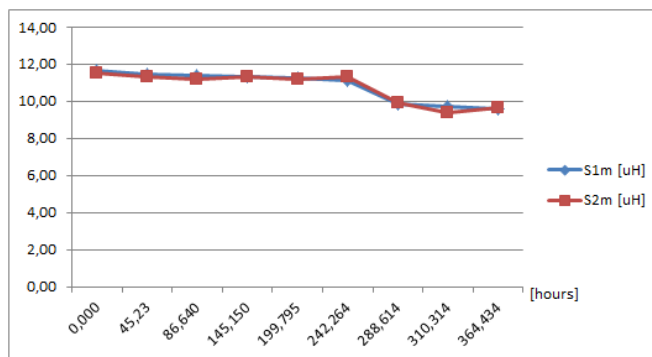

Fig. 7.22 Measured winding inductance [μH] for two motorette specimens during degradation with thermal cycle #3

Test results comparisons and curve fitting

As shown in Fig. 7.16 and Fig. 7.19, the insulation resistance (IR) between windings changed differently in relation to the aging time, when the motorettes were exposed to thermal cycle #2 and #3. In detail, the IR show slower declines at the beginning compared to the later reductions, during the degradation process of the motorettes exposed to thermal cycle #2. In comparison, when the motorettes are exposed to thermal cycle #3, increase of IR is observed first (at approx. 50 hours), followed by the decrease during the rest of the degradation process before the failures occur. The increased IR at approx. 50 hours could be caused by extra curing of the coating and epoxy at this cycled temperature level. After the assumed additional 'curing', a rapid decrease of IR is observed and then the reduction pace is slowed down, which is opposite to the IR changes of the motorettes exposed to thermal cycle #2.

The changes of insulation capacitance (IC) in relation to the degradation time between windings and between winding and ground are discussed as below. The IC changes of the motorettes [P.U.] exposed to thermal cycle #2 and #3 at both locations are shown in Fig. 7.23 and 7.24. In both measurement locations, decreases of IC are observed during degradation. Approx. 5% - 6% and 12% - 14% of IC decrease are obtained between windings and between winding and ground, respectively, during the degradation of motorettes exposed to thermal cycle #2. The corresponding figures are 4% - 6% and 11% - 12% respectively of motorettes exposed to thermal cycle #3. This is a strong indication that there is a value in studying the IC changes of the electrical machines by the on-board off-line condition monitoring method presented in Chapter 6.4.2.

The IC changes [P.U.] in relation to degradation time [hours] are fitted to Equation 7.4 with two exponential parts. Both IC changes between the windings and between the windings and ground in thermal cycle #2 and #3 are fitted. The fitted coefficients with 95% confidence bounds are summarized in Table. 7.3.

$$IC_{P.U.} = a \cdot e^{b \cdot time} + c \cdot e^{d \cdot time} \tag{7.4}$$

If the changes of one parameter under one thermal cycle are compared over time, the rate of life loss at different age of the EIS is not linear, although the same load is applied. Therefore, using the superposition method to accurately estimate the residual useful life (RUL) of EIS is difficult. The accurate RUL estimation relies on complete look-up tables or equations of the changes of properties of EIS in relation to time and different loadings. These look-up tables or equations

Table 7.3: Fitted polynomial coefficients of insulation capacitance changes versus degradation time

	a	b	c	d
Thermal cycle #2 (S1)				
between windings	0.046	-0.056	0.955	$-5.44 \cdot 10^{-5}$
between winding and ground	0.107	-1.33	0.893	$-1.65 \cdot 10^{-4}$
Thermal cycle #3 (S1m)				
between windings	0.028	-0.048	0.972	$-7.73 \cdot 10^{-5}$
between winding and ground	0.066	-0.107	0.943	$-1.78 \cdot 10^{-4}$

have to be obtained by more tests, which are similar to the ones presented in this Chapter 7.3.
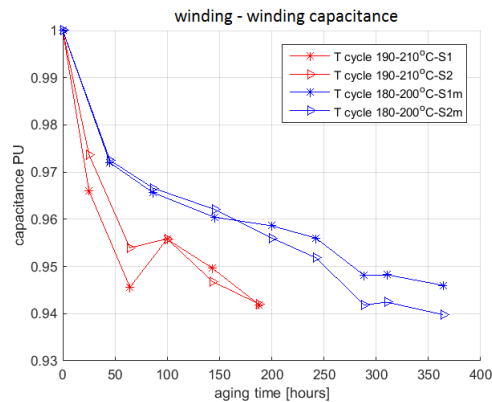

Fig. 7.23 Comparison of measured insulation capacitance [P.U.] **between 2 randomly grouped strands** during degradation with thermal cycle #2 and #3
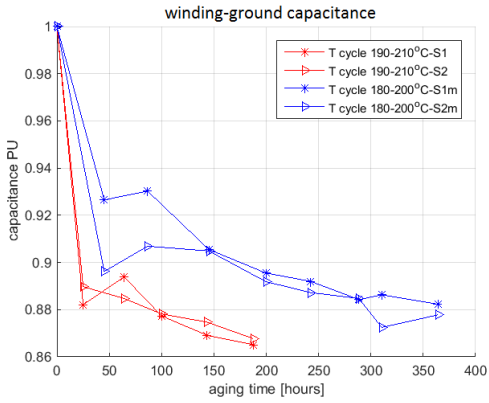
Fig. 7.24 Comparison of measured insulation capacitance [P.U.] **between winding and ground** during degradation with thermal cycle #2 and #3

7.4 Comparisons between modeling and testing of motorette

7.4.1 Condition monitoring of motorette

The condition monitoring parameters, i.e. insulation resistance (IR) and insulation capacitance (IC) are compared between the simulations and measurements in this section. The IR and IC between the windings are focused below because the values at this location reflects the state of health of all windings inside a slot and is more difficult to simulate accurately than the ones between the windings and ground. The comparisons are carried out on the 2nd group of specimens with complete epoxy impregnation (right side of Fig. 6.8). The values before (referred as 'initial state' below) and during the accelerated degradation testings are discussed.

As discussed in Chapter 3.5, the values of IR and IC between windings at the initial state are varied with different winding distributions and thicknesses of the insulation materials. With the constant coating thickness of 25 μm (defined by the data-sheet of the enameled wire of interest) and with the varied epoxy thickness of 50 μm - 120 μm, the simulated IC is in the range of 10 nF - 19 nF by the analytical model. At the initial state, the measured IC between the windings are between 14 nF and 16 nF as shown in Fig. 7.17(a) and 7.20(a), which are within the range of the simulation results.

With geometrical properties given above, at the initial state the simulated IR between windings is approx. 610 GΩ according to analytical model. In comparison, the measured IR is slightly lower and is in the range of 260 GΩ - 410 GΩ as shown in Fig. 7.14,7.16(a) and 7.19(a). At initial state, the differences of the measured IR between different specimens could be induced by the producing process or by the different winding distributions when the two paralleled strands are grouped for condition monitoring. The slightly lower IR in the measurements than the simulations could be because that the actual coating thickness is thinner than the simulated value (25 μm in the simulations) or the actual volume resistivity of coating is lower than the simulated value ($2 \cdot 10^{15} \Omega$m in the simulations). The coating volume resistance could be influenced by the additional curing process with the epoxy impregnation. However, the simulated and the measured IR are in the same order of magnitude. In the following sensitivity studies, the volume resistance of coating in the model is tuned to $1.2 \cdot 10^{15} \Omega$m at the initial state, which corresponds to an IR of 360 GΩ and is within the range of the measured IR.

The sensitivity studies are carried out with the varied volume resistances and different thicknesses of coating. The changes of volume resistance represent the irreversible changes of the coating property due to degradation. Fig. 7.25 shows the IR of the EIS in relation to the volume resistivity and the thickness of coating. Similar sensitivity study could be made for IC of the EIS with the analytical model but is not included in the thesis.
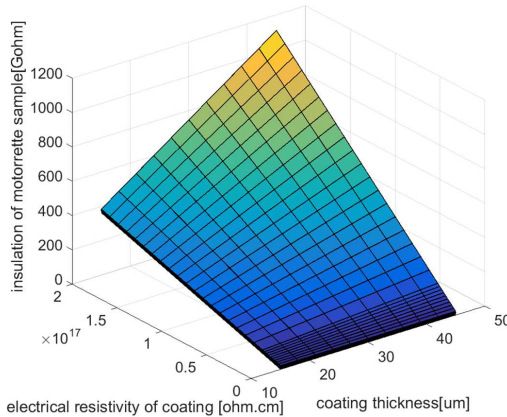
Fig. 7.25 Simulated IR of EIS versus the volume resistivity and the thickness of coating

From another perspective, the analytical model could be used to estimate the gradual changes of the dielectric properties of coating during aging, if the IR and IC of EIS are measured and the geometrical properties of the insulation materials are known. One example is given in Fig. 7.26. It shows the gradual changes of the volume resistance of coating when motorette is exposed to thermal cycle #2. The values in this figure are derived by the analytical model and based on the measured IR of the motorette during degradation (Fig. 7.16) and with coating thickness of 25 μm.

Regarding to the studies about insulations, it is always a question that whether the accelerated degradation testings should be performed on an electrical insulation (EI) material or on an electrical insulation system (EIS). The benefit to test EI individually is that the measured dielectric properties are generic, which can be applied to other calculations. However, it is hard to emulate the stresses induced between materials as in a real application, which could be achieved by the testings of EIS. Modelings like the one discussed above are essential to connect the mea-
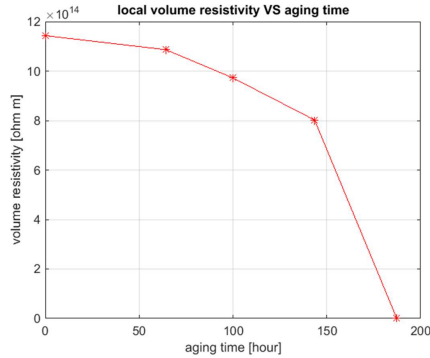
Fig. 7.26 Simulated global insulation resistance changes with different local volume resistivity and thickness of coating

sured EIS properties (i.e. IC and IR) with the dielectric properties of individual material at the initial state and during the process of aging.

7.4.2 Failure and lifetime of motorette

To define the failure of a motorette is challenge because the failure can arise at different locations inside the stator segment. Therefore, the resulted 'symptoms', i.e. the measurement results by condition monitoring, could be different. In this study, too low IR between windings or between winding and ground (temperature cycle #1 and #2) or steep change of winding inductance (temperature cycle #1 and #3) are all considered as failure of the motorettes. It is difficult to use one condition monitoring method to locate all possible failures in a stator. Instead, a combination of condition monitoring methods are required. To connect the measured failure 'symptoms' of the motorettes (or electrical machines) to the specific failure locations, modeling of the failures are required. However, the modeling of different types of failures are beyond the scope of this thesis, which is an interesting future work.

The lifetime of a motorette is decided when a failure occurs. The measured and estimated lifetime of the motorette are compared below. Two estimated lifetimes by the Arrhenius Law and the thermal-mechanical fatigue are compared below.

The thermal-mechanical stresses are calculated for the three different thermal cycles (see Table. 7.2). The maximum and minimum stresses and the respective stress ratios are presented in Table 7.4. Furthermore, the lifetime of the EIS ex-

posed to the cycled thermal-mechanical stresses are calculated and presented as 'LT 3' in table 7.5. LT 1 and LT 2 represent the lifetime of the EIS estimated by Arrhenius law with Thermal Index (TI) 200°C and TI 180°C of the coating, respectively. It shows that the lifetime estimated by Arrhenius law is much longer than the measured lifetime when the EIS is exposed to the tested thermal cycles. In contrast, the lifetime estimated by thermal-mechanical fatigue model is more accurate.

In order to comment on the confidence level of the measured lifetime, more samples should be tested. This is beyond the scope of this research and is an interesting future work.

Table 7.4: Maximum stress [MPa] with epoxy thickness of 0.05 mm and CTE of 155 ppm/°C with boundary 3 and 4 free to move

Maximum stresses at peak temperatures and stress ratio ($\frac{S_{min}}{S_{max}}$)			
Cycle #1	230°C	210°C	stress ratio
	123	111	0.9
Cycle #2	210°C	190°C	stress ratio
	111	100	0.9
Cycle #3	200°C	180°C	stress ratio
	105	94	0.895

Table 7.5: Tested thermal cycles and corresponding lifetime

Cycle No.	θ_{cycle} [°C]	LT 1 [hour]	LT 2 [hour]	LT 3 [hour]	tested [hour]
#1	210-230	4,255	949	30	<47
#2	190-210	24,999	4,256	119	150-180
#3	180-200	64,172	9,456	192	250-290

7.4.3 Design improvement

Simulations in Chapter 4.3.5 show that the thermal-mechanical stress of coating of the enameled wire is reduced by replacing the epoxy 4260 with the LORD epoxy. Furthermore, if the EIS with the LORD epoxy is exposed to the same thermal cycles, the induced mechanical cycle of the coating, in terms of mean value is

lower, compared to that of the EIS with epoxy 4260. If the amplitude/depth of the thermal-mechanical cycles are similar for the two EIS, the degradation of coating due to thermal-mechanical fatigue is slowed down and the lifetime is prolonged for EIS with the LORD epoxy. However, the accelerated aging tests are not carried out on the motorettes molded with the LORD epoxy due to the time limitation.

Thermal tests are carried out to compare the temperatures of the motorettes with epoxy 4260 and with the LORD epoxy. Two motorettes (one of each epoxy impregnation) are thermally isolated to the surroundings and are heated by DC current through the windings. The hot spot temperatures (measured by sensor 'winding 1' in Fig. 6.9) at steady-state are compared in Fig. 7.27. The blue and the red curves show the temperature-versus-current of the motorette impregnated with Epoxy 4260 and with LORD Epoxy, respectively. The motorette impregnated with the LORD epoxy shows $40°C$ lower at hot spot than the motorette impregnated with Epoxy 4260 at DC current 100 A. One example of the FEA steady state thermal simulation of the motorette with LORD epoxy is attached in Appendix. C.1.
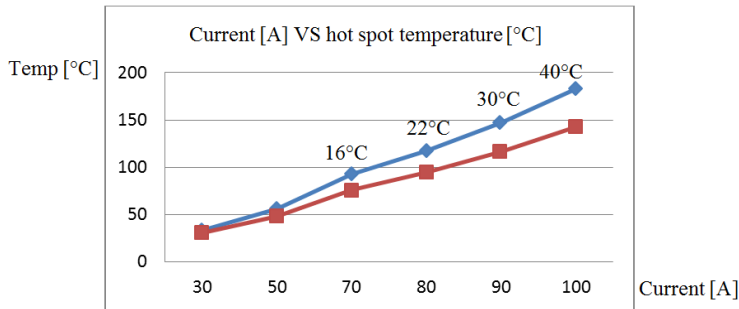

Fig. 7.27 Measured temperature comparisons of the two motorettes with two different epoxy impregnation: blue-Epoxy 4260, red-LORD epoxy

7.5 Results of system simulations of the VCE machine

The system simulation is illustrated by the flowchart 5.1. The application of it is demonstrated below, via the simulations of the VCE machine.

(a) Speed requirements for VCE machines

(b) Torque requirements for VCE machines (red: front wheel; blue: rear wheel)
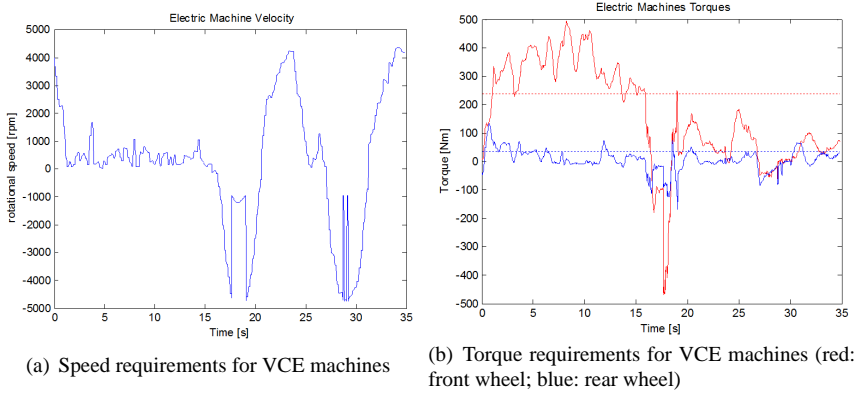
Figure 7.28: Speed and torque requirements for VCE electrical machines

7.5.1   Temperature distribution

The speeds and torques of the VCE machines (see Fig 7.28) are obtained after driving with Short Load Cycle (SLC) of the wheel loader. The SLC driving cycle of the wheel loader is demonstrated in Chapter 5 and each of the SLC lasts for 35 seconds. A total of 200 cycles are simulated. The speeds and torques of the electrical machines in front and in rear wheel are represented by the red and blue curve, respectively. The electrical machines in the front wheel are exposed to a tougher load cycles with much higher torque demands than the ones in the rear wheel. Because the pallet basket is in the front, thereby shifting the center of gravity of the wheel loader to the front of the vehicle. Taking this factor into consideration, thermal and lifetime simulation is focused one of the traction machines in the front wheel below.

The temperature distribution of the electrical machine in front wheel is obtained as shown in Fig. 7.29(a). The thermal steady state of the machine is reached after 200 SLC driving cycles. The temperature in the middle of the windings, stator tooth and stator iron back are presented by the blue, red and black curves, respectively. The hot spot temperature is observed in the middle of the windings. Also, the simulation results show that the temperatures in the stator are more dynamic than the temperatures in the rotor (i.e. rotor shaft, rotor yoke and magnet). The hot spot temperature is zoomed in between approx. 6,100 second and 6,300 second as shown in Fig. 7.29(b). In this figure, each temperature cycle between

(a) Overview of the temperature distribution

(b) Zoom in for temperature at middle of windings between approx. 6,100 s and 6,300 s
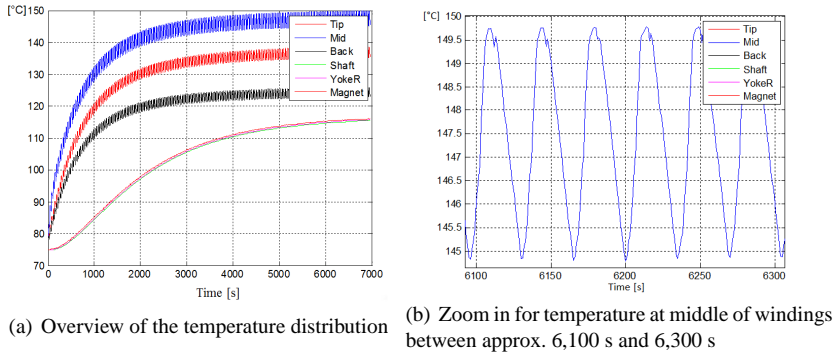
Figure 7.29: Temperature distribution of the VCE machine after driving 200 times of SLC

approx. 145°C and 150°C corresponds to one SLC driving cycle of 35 seconds.

7.5.2 Lifetime by Arrhenius Law

The Rainflow cycle counter is applied for the hot spot temperature of the VCE machine. The result is presented in Fig. 7.30, where 'X-ampl', 'Y-mean' represent the amplitude $((\theta_{max} - \theta_{min})/2)$ and the mean value $((\theta_{max} + \theta_{min})/2)$ of a temperature cycle in [°C], respectively. The values in z-axis are the number of temperature cycles that are calculated by the cycle counter. The most frequent thermal cycles are summarized in Table. 7.6.

Table 7.6: Typical thermal cycles of the VCE machine after driving with 200 times SLC cycles

Name	Mean [°C]	Amplitude [°C]	No. of cycles
A	149.9	6.2×10^{-5}	84
B	147	2	47
C	148	2.5	31.5

The thermal cycle A (see Table. 7.6) mainly represents the extremely small depth of cycles, for instance the ones between approx. 6,500s and 7,000s. Though the total number of cycles of thermal cycle A are about twice of the cycle B and C (see Table. 7.6), the duration of each cycle B and C is much longer than that

of cycle A. As a result, the thermal cycle B and C dominate the life loss in this application. Besides, the cycle with the greatest depth is the one with mean and amplitude of 112.2 °C and 37.5°C (0.5 cycles), respectively, and it represents the overall temperature between 0 to 7,000s.
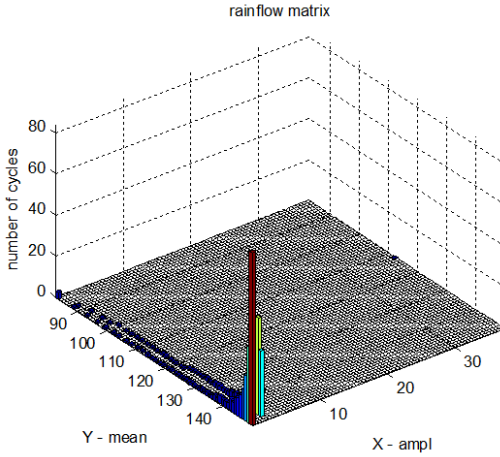
Fig. 7.30 Result from Rainflow cycle counter of the hot spot temperature (blue curve in Fig. 7.29(a))

The L10 lifetimes of the EIS estimated by Arrhenius Law of enameled wires (see Equation 5.3 and Fig. 5.14) are given in Table 7.7. Three EIS include enameled wires of different thermal grades are studied. One example of estimated life loss (in [%]) of the stator EIS of the VCE machine after driving with 200 times of SLC, is shown by the blue curve in Fig. 7.31. It is calculated with the enameled wire of Thermal Index (TI) 155°C.

Table 7.7: Estimated lifetime of the stator EIS of the VCE machine with different enameled wires

TI of enameled wire [°C]	L10 lifetime [hours]
155	9,684
180	122,312
200	625,564
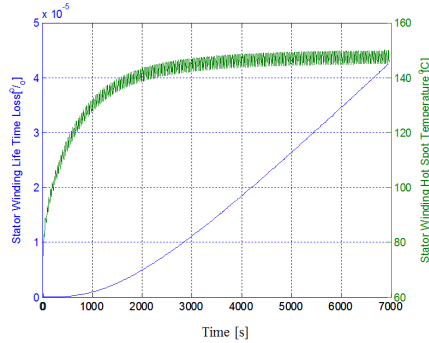
Fig. 7.31 Life loss (in %) of the stator EIS with the enameled wire of TI 155 °C after 200
times SLC

7.5.3   Thermal-mechanical stress and fatigue lifetime

The simulated thermal-mechanical stress versus time of the coating exposed to the
hot spot temperature (see green curve in Fig. 7.31) is shown in Fig. 7.32(a). The
thermal-mechanical stress is simulated with epoxy thickness of 0.05 mm, CTE of
155 ppm/°C and boundary 3 and 4 free to move. The simulation result is zoomed
in between approx. 6,100 second and 6,300 second as shown in Fig. 7.32(b) .

The mean, amplitude and number of cycles of the thermal-mechanical stress
are calculated by the Rainflow cycle counter. The result is shown in Fig. 7.33,
where 'X-ampl', 'Y-mean' represent the amplitude and the mean value of the
thermal-mechanical cycles in [MPa], respectively. The values in z-axis are the
number of thermal-mechanical cycles that are calculated by the cycle counter.
One of the typical cycles is identified with mean and amplitude of 46.1 MPa and
0.98 MPa, respectively, and the respective number of cycles is 106. For example,
the cycle between approx. 6,200s and 6,240s in Fig. 7.32(b) can be described by
this type of cycle.

The estimated lifetime of the EIS due to mechanical fatigue is 14,780 hours
with the thermal-mechanical profile in Fig. 7.32(a). This mechanical fatigue is
described by the stress-cycle life (S-N) equation (Fig. 5.16) of coating 7130. The
simulation results show that if the windings are made with enameled wires of TI
180°C or 200°C, the EIS will fail because of the thermal-mechanical stresses in-
duced by thermal cycles rather than high average temperature. In other words, a
high thermal grade of enameled wires does not always ensure a long thermal life-
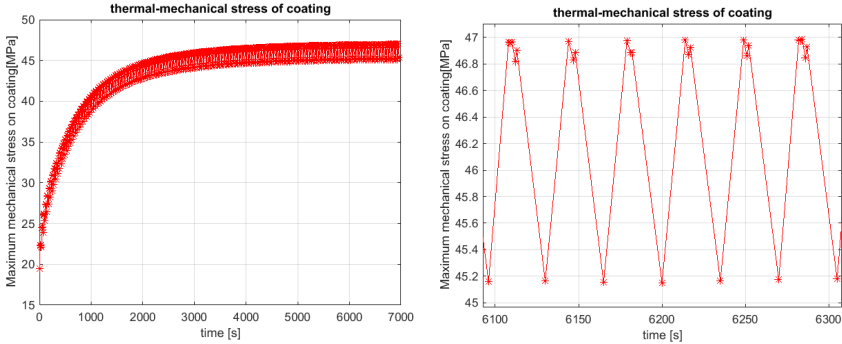
(a) Overview of the thermal-mechanical stress distribution of coating

(b) Zoom in of the thermal-mechanical stress distribution of coating between approx. 6,100 and 6,300s

Figure 7.32: Mechanical stress of coating induced by thermal stress of the VCE machine stator after running 200 times of SLC

time of the EIS if it is exposed to dynamic or cycled temperature. The dynamic thermal-mechanical stress on coatings, which is induced by the dynamic temperature and the interaction between the coating and the surrounding materials, results in mechanical fatigue of the coating furthermore fatigue of the EIS.

The thermal-mechanical fatigue lifetime of the EIS is calculated from the S-N curve of the coating 7130 and it is obtained from the fatigue test of stress ratio 0.9. However, the stress ratios of the stress cycles in Fig. 7.33 is much smaller. Therefore, the simulated thermal-mechanical fatigue lifetime of the EIS is shorter than that is in reality. However, the data of stress-life (S-N) curves of the coatings are not completed to make more accurate estimation. More fatigue tests with different mean stresses and stress ratios need to be performed on the coatings of interest, which is an interesting future work.

To conclude, the application of the system simulation (Fig. 5.1) is demonstrated via the simulations of the VCE machine with the SLC driving cycle in this section. Both the FEA thermal and the FEA thermal-mechanical simulations are carried out to estimate the temperature distribution and the mechanical stresses due to the dynamic loadings of the machine, respectively. Furthermore, the resulted thermal and thermal-mechanical stresses are used to calculate the lifetime losses caused by thermal oxidation and mechanical fatigue of the coating of interest, respectively. The lifetime of the EIS of the VCE machine is eventually

Fig. 7.33 Result from Rainflow cycle counter of the maximum mechanical stress of winding coating (Fig. 7.32(a))

determined by the shorter lifetime among the two calculated above.

7.6 Results of system simulation of RWD machine

The results of a system thermal simulation of the RWD machine are discussed in this section. The lifetime estimations by Arrhenius Law are also presented to compare the two cycle counting methods defined in Chapter. 5.4. The system thermal simulation is an integration of a drivetrain model of a hybrid electrical car and a Lumped Parameter Analysis (LPA) thermal model of the RWD machine. Both models are built and integrated by Matlab Simulink.

The LPA thermal model (Fig. 5.4) is verified against tests and presented in [3, 82, 108]. The temperature distribution of the RWD machine after driving with the US06 driving cycle is shown in Fig. 7.34. The temperatures at the middle of end and active part of the windings are shown by the red and magenta curves, respectively, which are the first and second highest temperatures of the machine.

The ambient temperature is set to 70 °C in accordance with the average coolant temperature at the inlet. As shown in Fig. 7.34, the hot spot temperature is below 180 °C at most of the time but with two peaks exceeding 180 °C for a short while. The frequent accelerations and regenerative brakes of the vehicle rise the average
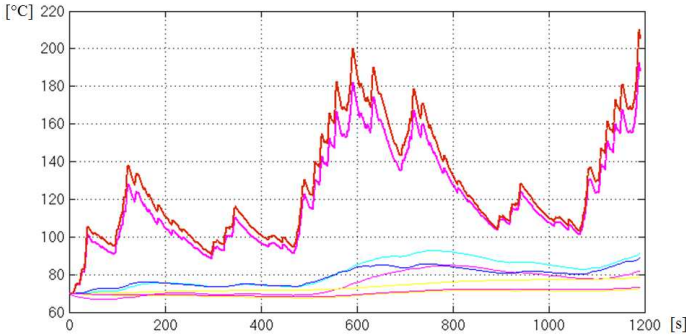
Fig. 7.34 Temperature evolution of RWD machine over US06 driving cycle

temperatures and leads to frequent temperature cycles of the electrical machine because of the demands of the high and dynamic torques. The increased temperatures and the frequent cycles between 500 and 600 second are due to such factors.

However, the thermal steady state of the machine has not been reached after one US06 driving cycle in this simulation. The hot spot temperature slightly exceeds 200°C when the driving cycle is terminated. If the same loadings and cooling are continued, over-heating will occur eventually. Therefore, an improvement of the cooling system of the RWD machine is required to accommodate the high way driving condition.

In the following calculations, we assume the temperatures of the machine are cooled to the ambient temperature of 70 °C before the next driving cycle is started, therefore the temperature cycle as Fig. 7.34 can be repeated. The lifetime of the RWD machine estimated by the two different cycle counters is shown in Table. 7.8.

Table. 7.8 shows the lifetime of the EIS with enameled wires of TI 155°C, 180°C and 200°C, respectively. Shorter lifetime is observed if the dynamic hot spot temperature is processed by the RainFlow cycle counter than that by the Mean edge 2 method, when other conditions are identical. It is because that some of the deep and long period cycles, which can be captured by the RainFlow counter, cannot be captured by the Mean edge2 counter. RainFlow cycle counting algorithm, which slightly overestimates the lifetime, helps the designer to choose the machine windings from the safe side.

Table 7.8: Estimated lifetime of RWD machine by Arrhenius Law

TI of enameled wire [°C]	Lifetime by mean edge 2 [hours]	Lifetime by Rain-flow [hours]
155	4,773	2,495
180	24,389	20,550
200	124,741	105,104

7.7 Results of on-board off-line diagnostic tests

As discussed in Chapter 7.3.2, insulation capacitance (IC) decreases between windings and between winding and ground during degradation. Approx. 4% to 6% and 11% to 14% of capacitance changes are observed at the two locations before failures, respectively. Therefore, the on-board off-line method is investigated via a master thesis [107] within the Ph.D. project. The test objects and test set-up are presented in Chapter 6.3 and Chapter 6.4.2, respectively. Some of the results are picked from the thesis [107] and presented below.

Fig. 7.35 illustrates the simplified equivalent circuit of the parasitic capacitance of the studied machines (see table 2.6 and Chapter 6.3). One of the measurements is carried out on the RWD machine with and without a simulated fault. The simulated fault is simulated by connecting a 1 nF capacitor in parallel with one phase winding. The DC excitation voltage of 50V is applied for 10 μs. The means of applying the excitation voltage is discussed in Chapter 6.4.2. As a result, the measured currents for both cases (with and without simulated fault) in the time domain and the frequency domain are shown in Fig. 7.36. The two currents in the frequency domain show clearer differences than they are in the time domain. For instance, the second and the third peaks of the current amplitudes are observed at a lower frequency with the 1 nF capacitor.

Different sensitivity studies are carried out and presented in [107]. Some interesting findings are highlighted as follows:

1. The measurement method shows good repeatability on both small and large sized PMSM machines (see Fig. 5.2 and 5.3 in [107]);

2. The current responses are independent on the rotor positions once the current sensor location is fixed (see Fig. 5.4 and 5.5 in [107]);

3. The current responses are independent on temperatures as shown in Fig. 7.37(a);
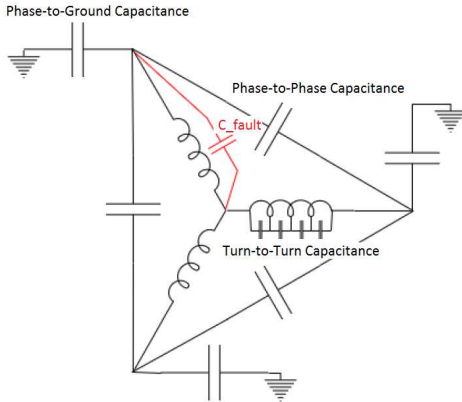
Fig. 7.35 Simplified equivalent circuit of parasitic capacitance for electrical machines and
simulated fault with a capacitor paralleled to one phase winding [107]

4. The cable capacitance between the drive and machine influences the total
   measured capacitance and therefore influence the current (see Fig. 5.11
   and 5.12 in [107]). Placing the sensors close to the machine of interest is
   recommend;

5. High frequency current sensor and A/D converter are needed. Approx. 15
   MHz current sensing and logging are required to measure the currents in
   Fig. 7.36.

In conclusion, the parasitic capacitance is gradually changed with aging of EIS
of electrical machines. This diagnostic method provides a means to indirectly keep
track of the above-mentioned changes by recording the high frequency current
when switch on the six-bridge converter to any switching-state of the drive and
comparing them over time. A clear connection between the high frequency current
and the parasitic capacitance relies on detailed FEA and circuit simulations and
has not been established in this study, which is an very interesting future work.
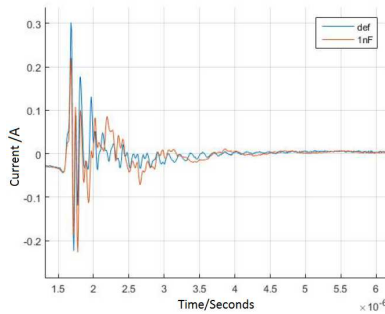
(a) Current responses in time domain
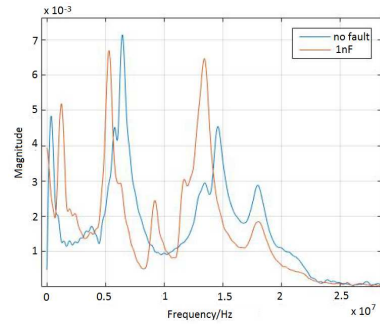
(b) Current responses (absolute value) in frequency domain

Figure 7.36: Current responses without (blue line) and with (red line) simulated fault
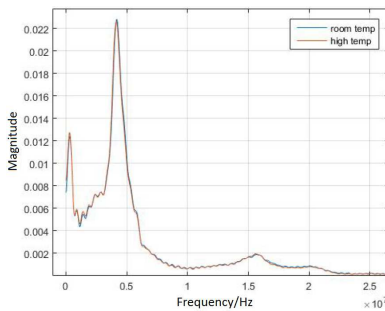
(a) Current response (absolute value) of EM 3 (defined in Chapter 6.3) at room temperature and at steady state $55°C$
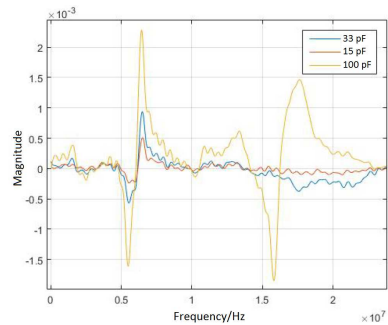
(b) Current response with varied levels of simulated degradation represented by different sizes of paralleled capacitors (Fig. 7.35)

Figure 7.37: Current responses in frequency domain - examples from sensitivity study

Chapter 8

Conclusions and future work

This chapter concludes the results and describes the limitations of the research. Furthermore, some interesting future investigations are proposed.

The usage of the electrical machines for traction purposes is investigated by system thermal modeling. The model uses driving cycles and drivetrain parameters of the studied vehicles as inputs and simulates the temperature distribution within the traction electrical machines. Two thermal simulation methods, FEA and LPA are applied on two types of electrical machines (the VCE machine and the RWD machine, see Chapter 5) used for a wheel loader and a car, respectively, and are simulated with their corresponding driving cycles. Both simulations identify the middle of the machine winding bundles as the hot spot. Besides, it is observed that the temperatures in the stator are quite dynamic over time compared to the temperatures in the rotor. The simulated hot spot temperature in relation to time is the input to further estimate the lifetime of the electrical insulation system (EIS) due to the dynamic temperature loading in the stator.

The accelerated aging testings are carried out for both enameled wire and motorette specimens to identify the degradation mechanisms of the EIS. For the motorette specimens, numerical simulations are implemented to estimate the measurement ranges to further understand the measurements. Major findings from both the accelerated aging tests and numerical simulations are discussed below.

Comparison tests with accelerated temperatures are carried out on enameled wires in different gas environments with and without the presence of oxygen. These tests represent stator windings without and with complete encapsulation,

respectively. Compared to the thermal aging in air, longer lifetime is obtained for the same enameled wire under the same temperature, but in the absence of air. In other words, if the high temperature oxidation is considered as the only degradation cause of polymer coating, the complete impregnation of windings should prevent the enameled wire coating from oxidation, thereby prolonging its lifetime.

However, from the accelerated degradation tests of the motorettes with complete impregnation, it shows that the lifetime of the winding coatings of the motorettes is shorter than the lifetime estimated by Arrhenius equations as shown in table 7.5. The Arrhenius equations are obtained with standard tests of enameled wires and the wires are tested with constant high temperatures in the presence of air. Whereas, the accelerated aging tests of motorettes are carried out with cycled temperatures and the wires are not directly exposed to air due to the complete impregnation. This emphasizes the motivation to look for other degradation mechanisms when the wire coatings in EIS is exposed to cycled temperatures.

The mechanical fatigue induced by cycled temperature is assumed to be the other degradation mechanism. We studied this mechanism through thermal- mechanical modeling and fatigue data of the wire coating material. The thermal cycle lifetimes estimated by thermal-mechanical stress simulations and S-N relation of coating material are closer to the lifetime obtained from accelerated tests compared to the estimated lifetime estimated by the Arrhenius law.

From a lifetime estimation perspective, if electrical machines with complete encapsulations are exposed to dynamic loading, the thermal-mechanical stress analysis of the primary electrical insulation, i.e. the winding coating, followed by a fatigue life estimation based on Inverse power law and Miner's rule (see Table 2.2) is proposed. This simulation together with the lifetime estimation based on Arrhenius law (see Table 2.2) represents the degradation caused by cycled temperature and average high temperature, respectively. The dominating degradation mechanism among the two above-mentioned factors is defined as the one that results in a shorter lifetime, despite the linked degradation effects between these two. The dominating degradation mechanism is different for different types of machines due to distinctive driving cycles, material properties, slot filling-factors etc. However, the use of a simplified single wire geometry to estimate the worst case scenario has its limitations and future studies using multiple wires of a full slot might provide a more precise conclusion.

Both the tested and simulated lifetime shows that the thermal-mechanical fa-

tigue is the dominating degradation mechanism for the studied VCE machine with complete encapsulation. The thermal-mechanical fatigue is most likely caused by the high thermal expansion ratio of the epoxy matrix material, which induces relatively high cycled thermal-mechanical stress on enameled wire coatings and also leads to the mechanical fatigue. Therefore, from an electrical machine design perspective, decreasing the thermal-expansion ratio of the epoxy from the root will eventually weaken the degradation mechanism caused by thermal-mechanical stress under cycled thermal loadings. For this reason, a LORD epoxy was tested for its thermal performance and simulated for its thermal-mechanical stress. Comparison tests of LORD epoxy and epoxy 4260 show that a lower temperature is obtained for the motorette with the LORD epoxy with the same current loading. Together with a lower thermal expansion ratio, the LORD epoxy induces lower thermal-mechanical stress on coatings compared to the original epoxy 4260. However, LORD epoxy has a higher density and is more rigid than epoxy 4260, therefore its performance in vehicles generating high frequency vibrations would be interesting to investigate.

Based on the insights into the importance of thermal-mechanical stress discussed above, one relevant interesting future study is to look into the possibility to directly measure the mechanical stress in windings induced by cycled temperatures. In order to achieve this, further studies of stress sensors and their implementation are essential.

Another important result of the accelerated aging tests is the measured trend of the dielectric parameters changes during degradation of EIS by the the condition monitoring approaches.

We propose a new approach to measure the health condition of the insulation inside the winding bundles through measuring the insulation resistance (IR) and insulation capacitance (IC) between two randomly separated strands of windings. Numerical simulations are utilized to understand and estimate the expected measurement ranges. Because of the random distribution and distance between wires inside a slot, the numerical model is not precise in calculating the IR and IC exactly, but it is useful when calculating expected ranges. The test results of the motorettes at the initial state are within the predicted range by simulations. Furthermore, the analytical model was used for the further sensitivity studies. The sensitivity studies show that the IR of the EIS is mainly contributed by the coating of wire since it has much higher electric resistivity than the epoxy and the IC of EIS was contributed by both the coating and the epoxy due to their similar

dielectric constant.

Using the information provided by the simulations of the motorettes at initial state, the analytical model is used to simulate the property changes of the EIS caused by the degradation of the coating. This provides an opportunity to understand the link between the individual EI material and the composed EIS. However, in these models, the property change of individual EI is simplified by assuming that each wire segment inside a slot is aged in the same manner. This assumption may be different in reality, considering the temperature gradients of winding bundles in a slot (see Fig. 4.10). More advanced models of the condition monitoring should be developed to include this effect.

The parameter changes of EIS during the three accelerated degradation tests are recorded with the above-mentioned condition monitoring methods. The tests show that the IR in relation to degradation time display different trends, but the IC changes display similar trends at different levels of temperature cycle. Results from the IC measurements are used for further on-board condition monitoring. Besides, compared to the IC measurement, the IR measurement is based on measuring low leakage current of the insulation system and is therefore very sensitive to the environment, such as temperature, humidity, etc. Thus the IR measurement can easily be applied in controlled lab environment, but difficult to be utilized as an on-board approach. The on-board condition monitoring approach, which is based on the theory that the parasitic capacitance changes during degradation, is investigated further in this study via a mater thesis. In this measurement, a voltage pulse excitation is set by switching the motor drive converter from the zero state to any other switching state, and furthermore the corresponding current is measured. Because of the parasitic capacitance change during degradation, the current magnitude and frequency, in the frequency domain changes accordingly. The measurement approach shows high repeatability and little dependency on temperatures. However, the current sensor sampling rate required for this type of measurement is much higher than the control need. A deeper understanding between the measured current and parasitic capacitance is required to identify a threshold current (the current level at which severe degradation is starting) and it has to rely on more detailed FEA and circuit modeling, which can be an important future study.

The lifetime modeling method (approach A) (Fig.5.1) and the measurements of the parameter changes of the EIS during degradation by condition monitoring (approach B) discussed above are also two approaches for prediction of State

of Health (SoH) or Residual Useful Life (RUL) of electrical machines. Both approaches must rely on knowledge of the electrical machine usage. The difference is that approach A relies on the degradation database of the critical EI material (for instance the changes of volume resistance of coating) and the lifetime modeling of the EIS, whereas approach B relies on a degradation database of the EIS of motorettes or entire machines (for instance the changes of IR) and most importantly the measurement feedback. The two above-mentioned degradation databases are both obtained from extensive tests with stresses of interest at different mean and amplitude levels. Completing the databases by comprehensive tests are important for future studies of SoH or RUL prediction. The tests with motorettes and complete machine are much more expensive than tests with individual materials.

Several important issues regarding the motorette production are observed. Since motorettes are seldom the standard products of any electrical machine manufacturer, procedures for designing and producing motorettes are not standardized. From the design point of view, there is a balance between the simplification of the motorette to save cost of materials and the oversized test equipment and its ability to represent the real winding slot and all types of stress that insulations could be exposed to. It is also important to keep the potential irrelevant failures of the assisting system (see cooling water leakage problem in Chapter 6.2) outside the motorette during the accelerated aging tests. From a production point of view, since it is not a standard manufacturing procedure, communication between the designer and the manufacturer as well as between different departments along the production line is quite important to ensure that the final motorettes are produced as expected and in a repeatable fashion (example as Fig. 6.8).

References

[1] G. C. Stone, E. A. Boulter, I. Culbert, and H. Dhirani, *Electrical insulation for rotating machines: design, evaluation, aging, testing, and repair*. John Wiley & Sons, 2004, vol. 21.

[2] M. Shanel, "Electrical insulation options for hybrid and electric vehicle applications in passenger vehicles, buses and trucks," DuPont, Tech. Rep., 2016.

[3] Z. Huang, F. J. Márquez-Fernández, Y. Loayza, A. Reinap, and M. Alaküla, "Dynamic thermal modeling and application of electrical machine in hybrid drives," in *International Conference on Electrical Machines (ICEM), 2014*. IEEE, 2014, pp. 2158–2164.

[4] P. Tavner, "Review of condition monitoring of rotating electrical machines," *IET Electric Power Applications*, vol. 2, no. 4, pp. 215–247, 2008.

[5] "Ieee working group report of problems with hydrogenerator thermoset stator windings part i, ii and iii," *IEEE Transactions on Power Apparatus and Systems*.

[6] O. V. Thorsen and M. Dalva, "A survey of faults on induction motors in offshore oil industry, petrochemical industry, gas terminals, and oil refineries," *IEEE transactions on industry applications*, vol. 31, no. 5, pp. 1186–1196, 1995.

[7] ——, "Failure identification and analysis for high voltage induction motors in petrochemical industry," in *Industry Applications Conference, 1998. Thirty-Third IAS Annual Meeting. The 1998 IEEE*, vol. 1. IEEE, 1998, pp. 291–298.

References

[8] P. Tavner and J. Hasson, "Predicting the design life of high integrity rotating electrical machines," in *Electrical Machines and Drives, 1999. Ninth International Conference on (Conf. Publ. No. 468)*. IET, 1999, pp. 286–290.

[9] Z. Zhu and C. Chan, "Electrical machine topologies and technologies for electric, hybrid, and fuel cell vehicles," in *2008 IEEE Vehicle Power and Propulsion Conference*, 2008.

[10] W. Xu, J. Zhu, Y. Guo, S. Wang, Y. Wang, and Z. Shi, "Survey on electrical machines in electrical vehicles," in *Applied Superconductivity and Electromagnetic Devices, 2009. ASEMD 2009. International Conference on*. IEEE, 2009, pp. 167–170.

[11] W. T. Shugg, *Handbook of electrical and electronic insulating materials*. IEEE press New York, 1995, vol. 995.

[12] "Insulator (electricity)," https://en.wikipedia.org/wiki/Insulator_(electricity), Nov. 2015.

[13] "Electrical insulation," http://encyclopedia2.thefreedictionary.com/Electrical+Insulation, Nov. 2015.

[14] "Impregnating resins," http://www.elantas.com/beck-india/products-services/secondary-insulation-si/impregnating-resins.html, Nov. 2016.

[15] S. R. Center, "Accelerated testing of systems and assemblies," 2004.

[16] W. B. Nelson, *Accelerated testing: statistical models, test plans, and data analysis*. John Wiley & Sons, 2009, vol. 344.

[17] *IEEE Recommended Practice for Thermal Cycle Testing of Form-Wound Stator Bars and Coils for Large Rotating Machines*, Std. IEEE 1310, 2012.

[18] P. Cygan and J. Laghari, "Models for insulation aging under electrical and thermal multistress," *IEEE transactions on electrical insulation*, vol. 25, no. 5, pp. 923–934, 1990.

[19] N. Lahoud, J. Faucher, D. Malec, and P. Maussion, "Electrical aging of the insulation of low-voltage machines: Model definition and test with the design of experiments," *IEEE Transactions on Industrial Electronics*, vol. 60, no. 9, pp. 4147–4155, 2013.

[20] "Electrical insulating material standards," https : / / www . astm . org / Standards / electrical - insulating - material_ standards.html, Oct. 2016.

[21] *Electrical Insulation - Thermal Classification*, Std. IEC 60 085, 2004-6.

[22] *Electrical insulating materials - Thermal endurance properties - Part 1: Ageing procedures and evaluation of test results*, Std. IEC 60 216 - 1, 2001.

[23] *Electrical insulating materials - Thermal endurance properties - Part 2: Determination of thermal endurance properties of electrical insulating materials - Choice of test criteria*, Std. IEC 60 216 - 2, 2005.

[24] *Electrical insulating materials - Thermal endurance properties - Part 5: Determination of relative thermal endurance index (RTE) of an insulating material*, Std. IEC 60 216 - 5, 2003.

[25] *Winding wires - Test methods - Part 6: Thermal properties*, Std. IEC 60 851 - 6, 2012.

[26] *Test Procedure for The Determination of The Temperature Index of Enamelled Winding Wires*, Std. IEC 60 172, 1987.

[27] *Electrical insulation systems - Procedures for thermal evaluation - Part 1: General requirements - Low-voltage*, Std. IEC 61 857-1, 2008.

[28] *Electrical insulation systems - Procedures for thermal evaluation - Part 21: Specific requirements for general-purpose models - Wire-wound applications*, Std. IEC 61 857-21, 2009.

[29] *Rotating electrical machines - Part 18-31: Functional evaluation of insulation systems - Test procedures for form-wound windings - Thermal evaluation and classification of insulation systems used in rotating machines*, Std. IEC 60 034-18-31, 2012.

[30] *Rotating electrical machines - Part 18-34: Functional evaluation of insulation systems - Test procedures for form-wound windings - Evaluation of thermomechanical endurance of insulation systems*, Std. IEC 60 034-18-34, 2012.

References

[31] *IEEE Recommended Practice for Thermal Evaluation of Unsealed Or Sealed Insulation Systems for AC Electric Machinery Employing Form-Wound Pre-Insulated Stator Coils for Machines Rated 15 000 V and Below*, Std. IEEE 1776, 2008.

[32] "Fluke insulation resistance testing-application note," http://www.testequipmentdepot.com/application-notes/pdf/insulation_testers/insulation-resistance-testing_an.PDF, September 2016.

[33] "Current state of surge testing induction machines," http://www.existest.com/appnotes/Baker/Teoria%20Surge.pdf, September 2016.

[34] *Rotating electrical machines - Part 25: Guide for the design and performance of cage induction motors for converter supply*, Std. IEC 60 034 - 25, 2002.

[35] H. Edin, "Partial discharges studied with variable frequency of the applied voltage," 2001.

[36] C. Forssén and H. Edin, "Measured partial discharge inception voltage for a cavity at different applied frequencies," 2007.

[37] *Rotating electrical machines - Part 18-41: Qualification and type tests for Type I electrical insulation systems used in rotating electrical machines fed from voltage converters*, Std. IEC 60 034 - 18 - 41, 2006.

[38] *Rotating electrical machines - Part 18-42: Qualification and acceptance tests for partial discharge resistant electrical insulation systems (Type II) used in rotating electrical machines fed from voltage converters*, Std. IEC 60 034 - 18 - 42, 2008.

[39] S. Nandi, H. A. Toliyat, and X. Li, "Condition monitoring and fault diagnosis of electrical motors-a review," *IEEE transactions on energy conversion*, vol. 20, no. 4, pp. 719–729, 2005.

[40] J.-H. Jung, J.-J. Lee, and B.-H. Kwon, "Online diagnosis of induction motors using mcsa," *IEEE Transactions on Industrial Electronics*, vol. 53, no. 6, pp. 1842–1852, 2006.

[41] P. McFadden and J. Smith, "Vibration monitoring of rolling element bearings by the high-frequency resonance technique-a review," *Tribology international*, vol. 17, no. 1, pp. 3–10, 1984.

[42] D. Ho and R. Randall, "Optimisation of bearing diagnostic techniques using simulated and actual bearing fault signals," *Mechanical systems and signal processing*, vol. 14, no. 5, pp. 763–788, 2000.

[43] R. Randall, "Developments in digital analysis techniques for diagnostics of bearings and gears," in *Fifth International Congress on Sound and Vibration, Adelaide, South Australia*, 1997.

[44] J. Härsjö, *Modeling and analysis of PMSM with turn-to-turn fault.* Ph.D. Thesis, Chalmers University of Technology, 2016.

[45] L. A. Dissado and J. C. Fothergill, *Electrical degradation and breakdown in polymers.* IET, 1992, vol. 9.

[46] Z. Huang, A. Reinap, and M. Alaküla, "Dielectric properties modeling and measurement of single tooth coil insulation system under accelerated degradation test," in *International Conference on Electrical Machines (ICEM), 2014.* IEEE, 2016.

[47] ——, "Predictive monitoring of turn-on-turn insulation in single tooth coils," in *10th International Symposium on Diagnostics for Electric Machines, Power Electronics and Drives (SDEMPED), 2015.* IEEE, 2015, pp. 171–177.

[48] "Polyamide-imide," https://en.wikipedia.org/wiki/Polyamide-imide, July 2016.

[49] "Product information - elan-tron$^{\circledR}$, mc 4260/w 4260, 100:10," http://www.wes.uk.com/files/74.pdf, July 2016.

[50] "Electrical resistivity and conductivity," https://en.wikipedia.org/wiki/Electrical_resistivity_and_conductivity, September 2016.

[51] P. Stenzel, P. Dollinger, J. Richnow, and J. Franke, "Innovative needle winding method using curved wire guide in order to significantly increase the copper fill factor," in *Electrical Machines and Systems (ICEMS), 2014 17th International Conference on.* IEEE, 2014, pp. 3047–3053.

References

[52] "Round enamelled winding wire of copper, heat resistant, class 200 product information," http://www.lww.se/wp-content/uploads/2014/06/DAMID-200.pdf, July 2016.

[53] "Dielectric strength," https://en.wikipedia.org/wiki/Dielectric_strength, September 2016.

[54] Y. Lin, H. Sautereau, and J. Pascault, "Epoxy network structure effect on physical aging behavior," *Journal of applied polymer science*, vol. 32, no. 4, pp. 4595–4605, 1986.

[55] G. Odegard and A. Bandyopadhyay, "Physical aging of epoxy polymers and their composites," *Journal of Polymer Science Part B: Polymer Physics*, vol. 49, no. 24, pp. 1695–1716, 2011.

[56] C. DeMilo, C. Bergad, R. Forni, and T. Brukilacchio, "Thermally induced stresses resulting from coefficient of thermal expansion differentials between an led sub-mount material and various mounting substrates," in *Integrated Optoelectronic Devices 2007*. International Society for Optics and Photonics, 2007, pp. 64 860N–64 860N.

[57] H.-K. Tseng and M.-L. Wu, "Electro-thermal-mechanical modeling of wire bonding failures in igbt," in *2013 8th International Microsystems, Packaging, Assembly and Circuits Technology Conference (IMPACT)*. IEEE, 2013, pp. 152–157.

[58] X. Hao, L. Qin, D. Yang, and S. Liu, "Thermal-mechanical stress and fatigue failure analysis of a pbga," in *Electronic Packaging Technology Proceedings, 2003. ICEPT 2003. Fifth International Conference on*. IEEE, 2003, pp. 438–442.

[59] W. Li and X. Zhang, "Thermal-mechanical failure and life analysis on cbga package used for great scale fpga chip," in *Electronic Packaging Technology & High Density Packaging, 2009. ICEPT-HDP'09. International Conference on*. IEEE, 2009, pp. 1216–1219.

[60] C. Hsueh, P. Becher, and E. Sun, "Analyses of thermal expansion behavior of intergranular two-phase composites," *Journal of materials science*, vol. 36, no. 1, pp. 255–261, 2001.

[61] Y. Fu, Y. Wong, C. Tang, and C. Poon, "Thermal induced stress and associated cracking in cement-based composite at elevated temperatures—-part i: Thermal cracking around single inclusion," *Cement and Concrete Composites*, vol. 26, no. 2, pp. 99–111, 2004.

[62] ——, "Thermal induced stress and associated cracking in cement-based composite at elevated temperatures—-part ii: thermal cracking around multiple inclusions," *Cement and Concrete Composites*, vol. 26, no. 2, pp. 113–126, 2004.

[63] A. Mouritz, S. Feih, E. Kandare, and A. Gibson, "Thermal–mechanical modelling of laminates with fire protection coating," *Composites Part B: Engineering*, vol. 48, pp. 68–78, 2013.

[64] C. Bathias and A. Pineau, *Fatigue of materials and structures: application to design*.   John Wiley & Sons, 2013.

[65] A. Constantinescu, E. Charkaluk, G. Lederer, and L. Verger, "A computational approach to thermomechanical fatigue," *International Journal of fatigue*, vol. 26, no. 8, pp. 805–818, 2004.

[66] A. Derewonko, J. Godzimirski, K. Kosiuczenko, T. Niezgoda, and A. Kiczko, "Strength assessment of adhesive-bonded joints," *Computational materials science*, vol. 43, no. 1, pp. 157–164, 2008.

[67] J. Tomblin, W. Seneviratne, P. Escobar, and Y. Yoon-Khian, "Shear stress-strain data for structural adhesives," DTIC Document, Tech. Rep., 2002.

[68] J. F. Mandell and D. D. Samborsky, "Doe/msu composite material fatigue database: test methods, materials, and analysis," Sandia National Labs., Albuquerque, NM (United States), Tech. Rep., 1997.

[69] P. Reis, J. Ferreira, J. Costa, and M. Richardson, "Fatigue life evaluation for carbon/epoxy laminate composites under constant and variable block loading," *Composites Science and Technology*, vol. 69, no. 2, pp. 154–160, 2009.

[70] L. J. Broutman and S. K. Gaggar, "Fatigue behavior of epoxy and polyester resins," *International Journal of Polymeric Materials*, vol. 1, no. 4, pp. 295–316, 1972.

References

[71] D. L. Logan, *A first course in the finite element method*. Cengage Learning, 2011.

[72] "Structural dynamics," https://en.wikipedia.org/wiki/Structural_dynamics, July 2016.

[73] "What's the different between quasi-static and dynamic analyse?" https : / / www . researchgate . net / post / Whats_the_different_between_quasi-static_and_dynamic_analyse, July 2016.

[74] J. Gere and S. Timoshenko, *Mechanics of materials, 3rd SI edition*. Chapman & Hall, London, 1991.

[75] Z. Huang, A. Reinap, and M. Alaküla, "Degradation and fatigue of epoxy impregnated traction motors due to thermal and thermal induced mechanical stress-part i: thermal mechanical simulation of single wire due to evenly distributed temperature," 2016.

[76] W. Chen and C. Nelson, "Thermal stress in bonded joints," *IBM Journal of Research and Development*, vol. 23, no. 2, pp. 179–188, 1979.

[77] I. ANSYS, *ANSYS Mechanical APDL theory reference*, 2016.

[78] "Who/what is von mises stress, and why do we use it in fea analysis?" https : / / www . capinc . com / 2014 / 02 / 12 / frequently_asked-questions-on-von-mises-stress-explained, December 2016.

[79] "Materials data book," Cambridge University Engineering Department, Tech. Rep., 2003.

[80] Z. Huang, A. Reinap, and M. Alaküla, "Degradation and fatigue of epoxy impregnated traction motors due to thermal and thermal induced mechanical stress part ii," in *8th International Conference on Power Electronics, Machines and Drives PEMD 2016*, 2016.

[81] Z. Huang, *Thermal Design of Electrical Machines-Investigation and Evaluation of Cooling Performances*. Licentiate Thesis, Lund University, 2013.

[82] F. Marquez-Fernandez, A. Reinap, Z. Huang, and M. Alaküla, "Dynamic evaluation of the overloading potential of a convection cooled permanent

magnet synchronous motor," in *2011 IEEE International Electric Machines & Drives Conference (IEMDC)*. IEEE, 2011, pp. 13–18.

[83] V. Nezhadali and L. Eriksson, "Optimal control of wheel loader operation in the short loading cycle using two braking alternatives," *IEEE VPPC*, 2013.

[84] P. Ingelsröm, "Thermal measurements and simulations of the vce wheel hub electrical motor," Volvo Group, Tech. Rep., 2014.

[85] J. Ottosson, *Thermal Modelling of Power Modules in a Hybrid Vehicle Application*. Ph.D. Thesis, Lund University, 2013.

[86] U. S. of America: Department of Defense, *Military Handbook: Reliability Prediction of Electronic Equipment: MIL-HDBK-217F: 2 December 1991*. Department of defense, 1991.

[87] S. Ariduru, "Fatigue life calculation by rainflow cycle counting method," *Middle East Technical University, Tese de Mestrado*, 2004.

[88] *Standard Practices for Cycle Counting in Fatigue Analysis*, Std. ASTM E1049-85, 2005.

[89] Y.-L. Lee and T. Tjhung, "Rainflow cycle counting techniques," *Metal Fatigue Analysis Handbook: Practical Problem-solving Techniques for Computer-aided Engineering*, p. 89, 2011.

[90] *Functional Evaluation of Insulation Systems - Test Procedures for Wire-Wound Windings - Thermal Evaluation and Classification*, Std. IEC 60 034-18-21, 2012.

[91] "Fatigue (material)," https : / / en . wikipedia . org / wiki / Fatigue_(material)#High-cycle_fatigue, July 2016.

[92] L. F. M. da Silva and A. Öchsner, *Modeling of adhesively bonded joints*. Springer, 2008.

[93] R. C. Juvinall and K. M. Marshek, *Fundamentals of machine component design*. John Wiley & Sons New York, 2006, vol. 83.

[94] "Torlon pai design guide," http://www.solvay.com/en/binaries/Torlon-PAI_Design-Guide_EN-227547.pdf, July 2016.

References

[95] "What is a sn-curve?" https://community.plm.automation.siemens.com/t5/_Testing-Knowledge-Base/What-is-a-SN-Curve/ta-p/355935, December 2016.

[96] D. D. Samborsky, T. J. Wilson, and J. F. Mandell, "Comparison of tensile fatigue resistance and constant life diagrams for several potential wind turbine blade laminates," *Journal of solar energy engineering*, vol. 131, no. 1, p. 011006, 2009.

[97] M. Handbook, "Electronic reliability design handbook," MIL-HDBK-338, DoD, Tech. Rep., 1988.

[98] "Nist/sematech e-handbook of statistical methods," http://www.itl.nist.gov/div898/handbook/eda/section3/eda3668.htm, July 2016.

[99] H. Bloch and F. Geitner, "Practical machinery management for process plants. volume 2: Machinery failure analysis and troubleshooting," Exxon Chemical Co., Baytown, TX, Tech. Rep., 1983.

[100] T. Hakamada, "Analysis of weibull distribution for electrical breakdown voltage o stator windings," *IEEE transactions on electrical insulation*, no. 2, pp. 114–118, 1984.

[101] *Polymeric Materials - Long Term Property Evaluations*, Std. UL 746B, 2001.

[102] D. W. L. Hawkins, *Polymer Degradation and Stabilization*. Springer Berlin Heidelberg, 1984.

[103] A. G. eited by S.Halim Hamid, Mohamed B.Amin, *Handbook of Polymer Degradation*. Research Institute King Fahd University of Petroleum & Minerals, Dhahran, Saudi Arabia, 1992.

[104] "Scanning electron microscope," https://en.wikipedia.org/wiki/Scanning_electron_microscope, December 2016.

[105] "Thermogravimetric analysis," https://en.wikipedia.org/wiki/Thermo_gravimetric_analysis, December 2016.

[106] Z. Huang, "Final report of project 'dynamic modeling of cooling for electrical drive system' to energimyndigheten," 2016.

[107] J. Björngreen, "Pmsm diagnostics and prognostics," Master's thesis, Lund University, 2016.

[108] F. Marquez, *Electric Traction Machine Design for an E-RWD Unit*.   Ph.D. Thesis, Lund University, 2014.

[109] R. Andersson, *Electric Traction Machine Design for Heavy Hybrid Vehicles*.   Licentiate Thesis, Lund University, 2014.

[110] W. S. Zaengl, "Dielectric spectroscopy in time and frequency domain for hv power equipment. i. theoretical considerations," *IEEE Electrical Insulation Magazine*, vol. 19, no. 5, pp. 5–19, 2003.

[111] A. Helgeson and U. Gafvert, "Dielectric response measurements in time and frequency domain on high voltage insulation with different response," in *Electrical Insulating Materials, 1998. Proceedings of 1998 International Symposium on*.   IEEE, 1998, pp. 393–398.

[112] M. Farahani, H. Borsi, and E. Gockenbach, "Dielectric response studies on insulating system of high voltage rotating machines," *IEEE Transactions on Dielectrics and Electrical Insulation*, vol. 13, no. 2, pp. 383–393, 2006.

References

Appendix A

Control schematics of the accelerated aging test rig

In this appendix, the control schematics of the accelerated degradation tests are attached.
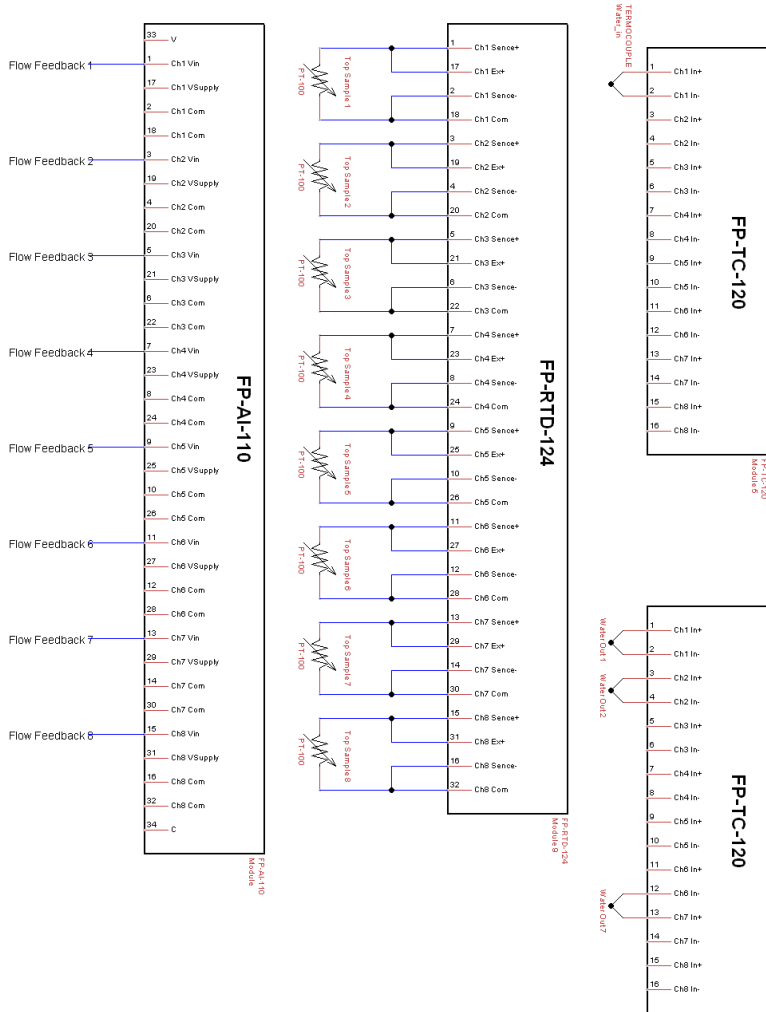
Fig. A.1 Control schematics for accelerated aging test - logging of flow rates, temperatures of motorette iron and coolant
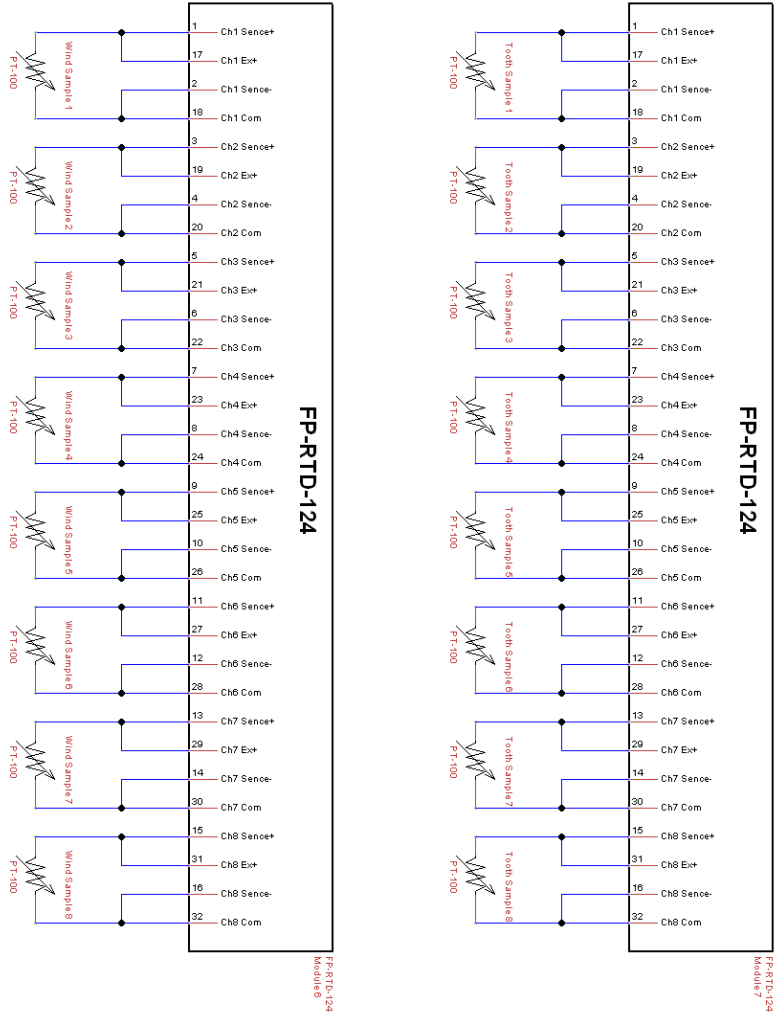
Fig. A.2 Control schematics for accelerated aging test - logging of motorettes temperatures
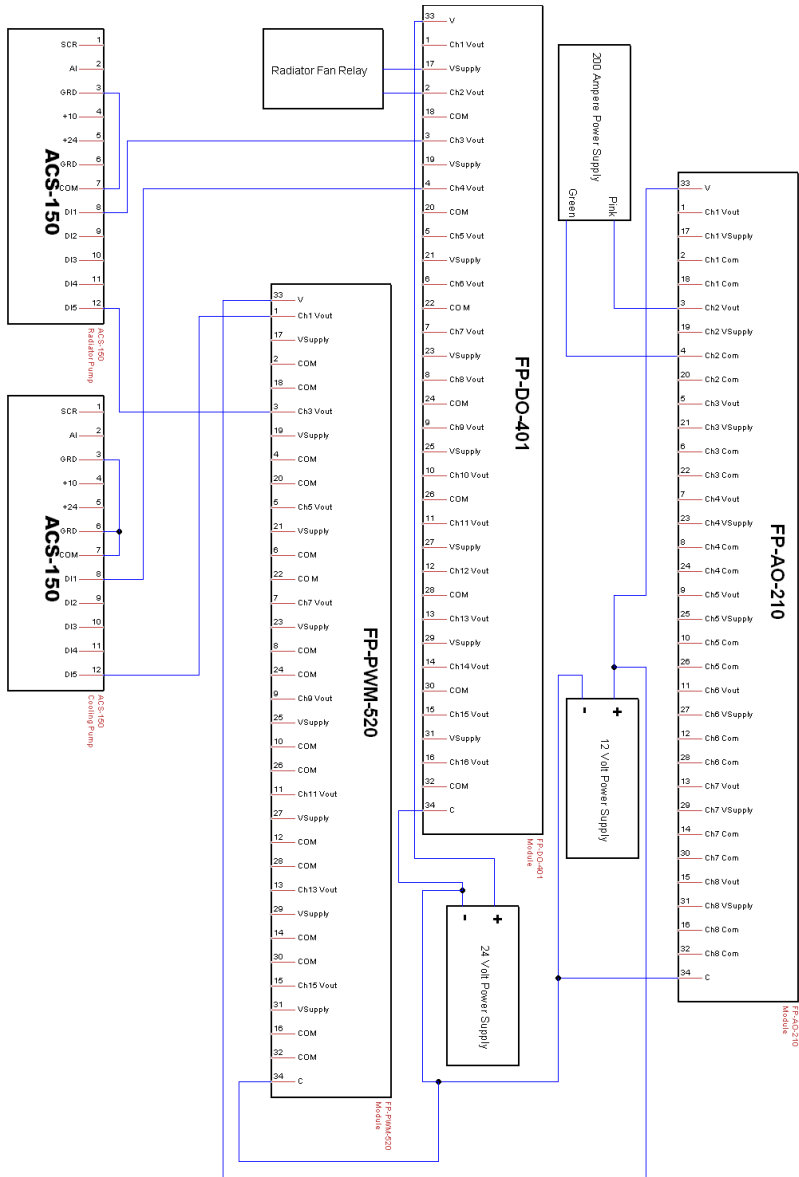
Fig. A.3 Control schematics for accelerated aging test - control of power supply, cooling
pump, radiator pump, radiator fans

Appendix B

Motorette specimen

B.1 List of motorette specimens

This appendix summarizes the motorettes used for condition monitoring and accelerated degradation testings.

Total number of specimens	Name	Function
1st group of specimens		
1	-	To study the insulation leakage current or the insulation resistance (IR) at transient and steady state when specimens are new
8	S1-S8	To study the insulation capacitance (IC) when specimens are new
2nd group of specimens		
8	S1-S8	S1 to S6 are used to study both the IR and the IC during degradation with thermal cycle[1] #1. S7 and S8 are the reference samples.
2	S1,S2	To study both the IR and the IC during degradation with thermal cycle #2
2	S1m,S2m	To study both the IR and the IC during degradation with thermal cycle #3

B.2 An example of the measured winding hot spot temperature

Fig. B.1 shows an example of the measured hot spot temperatures of the six motorettes tested simultaneously.
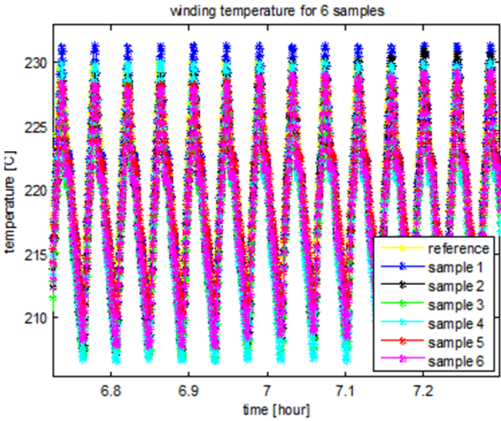

Fig. B.1 Measured hot spot temperature in windings of the 6 motorette specimens in accelerated test (thermal cycle #1, defined in Table 7.2)

---

[1]Thermal cycles are defined in Table. 7.2

Appendix C

Examples from FEA simulations

C.1 FEA thermal simulation

Fig. C.1 shows an example of FEA thermal simulation in steady-state on the motorette with LORD epoxy.
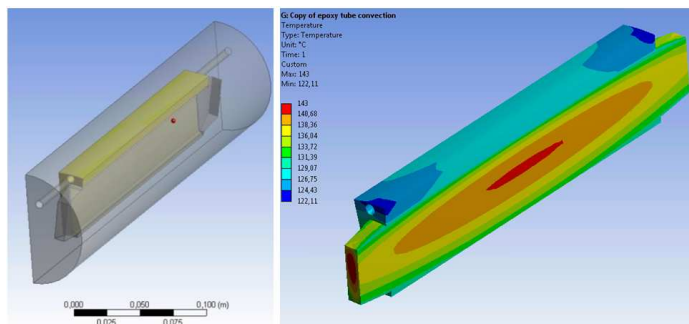

Fig. C.1 Example of steady-state FEA thermal simulation with LORD epoxy as impregnation material at 100 A

C.2 Loss simulation

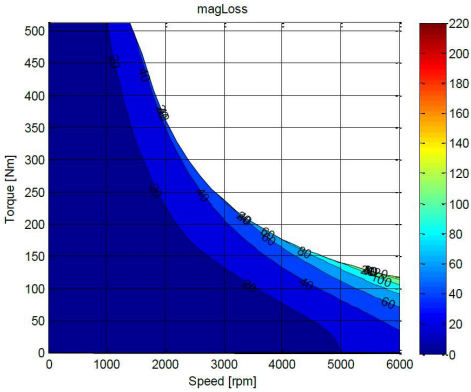Fig. C.2 shows the eddy current loss in magnets of the VCE machine from the FEA electromagnetic simulation.

Fig. C.2 Simulated eddy current loss in magnets of VCE machine

Appendix D

Abbreviations

EV	Electrified Vehicles
TEAM stresses	Thermal, Electrical, Ambient and Mechanical stresses
EI	Electrical Insulation
EIS	Electrical Insulation System
DC	Direct Current
AC	Alternating Current
SoH	State of Health
LV	Low Voltage
MV	Medium Voltage
HV	High Voltage
IM	Induction Machine
SRM	Switch Reluctance Machine
RM	Reluctance Machine
PMM	Permanent Magnet Machine
PMSM	Permanent Magnet synchronous Machine
ICE	Internal Combustion Engine
OEM	Original Equipment Manufacturer
PAI	Polyamideimide
PEI	Polyetherimide
VPI	Vacuum and Pressure Impregnation
DoE	Design of Experiment
CDF	Cumulative Distribution Function

Appendix D. Abbreviations

PI	Polarization Index
DAR	Dielectric Absorption ratio
PD	Partial Discharge
PDIV	Partial Discharge Inception Voltage
CIV	Corona Inception Voltage
MCSA	Motor Current Signature Analysis
RF	Radio Frequency
FE	Finite Element
FEA	Finite Element Analysis
LPA	Lumped Parameter Analysis
CFD	Computational Fluid Dynamics
IR	Insulation Resistance
IC	Insulation Capacitance
LED	Light Emitting Diode
IGBT	Insulated-Gate Bipolar Transistor
PBGA	Plastic Ball Grid Array
FPGA	Field Programmable Gate Array
S-N	Stress-Life or Stress-Cycle Life
CTE	Coefficient of Thermal Expansion
1D	One Dimension
3D	Three Dimension
SLC	Short Loading Cycle
WL	Wheel Loader
BC	Boundary Condition
TI	Thermal Index
HCF	High Cycled Fatigue
LCF	Low Cycled Fatigue
SEM	Scanning Electron Microscopy
SE	Secondary Electrons
BSE	Backscattered Electrons
TGA	Thermal Gravimetric Analysis
FP	Field Point
NI	National Instrument
cRIO	Compact Reconfigurable IO modules
P.U.	Per Unit
RUL	Residual Useful Life
LT	Lifetime
VCE	Volvo Construction Equipment
RWD	Rear Wheel Driven